Dynamic Simulations of Hot-Electron Quantum-Optics Devices

Keaghan Krog

Thesis submitted for the degree of
Doctor of Philosophy

School of Mathematics, Statistics & Physics
Newcastle University
Newcastle upon Tyne
United Kingdom

July 2023

This thesis is dedicated to my mother

Acknowledgements

There are a number of people who I am indebted to and without whom this thesis might not have been written. I am extremely grateful to my supervisor, Clive Emary, for his support, guidance, and patience throughout this journey. I would also like to thank the group's collaborators Andrea Bertoni, Masaya Kataoka, Nathan Johnson, and Patrick See.

I had the pleasure of pursuing this PhD with the other amazing members of the HEQO group, Lewis Clark and Clarissa Barratt, both of whom have supported me throughout. In particular, special thanks go to Lewis for taking the time to mentor and guide me right to the end.

Thank you to all my fellow PGRs for making an amazing research environment at Newcastle University and provided much needed breaks to play badminton, go climbing, or just a trip to the pub.

This endeavour would not have been possible without my incredible family. Thank you to my brothers for providing me with love and support and I am forever grateful to my Dad for motivating me and being there for me every step of the way.

Finally, to Sophie Crompton, thank you for your love, positivity, and endless patience throughout this journey with me.

Abstract

It has been a long standing ambition of the mesoscopic community to perform quantum-optics like experiments with electrons. The advent of single photon sources paved new ways of exploring quantum optics phenomena and with the introduction of single electron sources it is hoped that the same advancement within the field of electron quantum optics can be found. Early realisations of these single sources were used for electronic Mach-Zehnder, Hanbury-Brown-Twiss, and Fabry-Perot interferometers. However, they highlight significant difference between electron and photon quantum optics: the quantum statistics of the particles, the presence of the Fermi sea and Coulomb interactions.

Recently, experiments using quantum-dot charge pumps have been shown to be a reliable source of single electrons. In addition, they are able to emit electrons at energies far above the Fermi level. These "hot electrons" offer solutions to the previous problems as their energetic separation is thought to isolate them from electron-electron interactions. With the application of a strong magnetic field, edge channels are formed due to the integer quantum Hall effect, which creates ballistic channels for the single electrons mimicking optical paths.

The objective of this thesis comprises of two main parts. We begin by creating accurate models of realistic device potentials by introducing a method to model the electrostatic potential at the depth of the two-dimensional electron gas. Previously, other methods which are used to obtain these electrostatic potentials only address the use of one fabrication technique to manipulate the motion of electrons. However, our method incorporates both surface gates of Ti/Au and chemical etching which are used by M. Kataoka at the National Physical Laboratory. We call this the projected surface method which additionally offers a reduction in computational cost over other methods such as the finite element method. The use of this new method is applied to two devices: a time of flight experiment and a Mach-Zehnder interferometer. We will perform analysis on the electrostatic potential acquiring the velocity and spatial trajectory of the electron.

The second part of the thesis focuses on the study of the electron transport around these devices using dynamic simulations. By applying a single wave-packet propagation code to their potentials we can model the electrons as Gaussian wave packets and numerically integrate the two-dimensional Schrödinger equation to evolve the wave packet around our calculated potentials. This approach utilises the Trotter-Suzuki factorisation and the Fourier split-step method for stability and efficiency. Initially we apply this simulation to simple geometries of devices then continue on to the realistic device potentials, such as the time-of-flight experiment and a variety of quantum point contacts. Not only do the simulations provide detailed time- and energy-resolved information that is accessible

experimentally but also provide information about how the electron is travelling within the device between emission and detection.

Dissemination of results

The results of this thesis have been partially covered in the following:

- *Electrostatic modelling of electron quantum-optics devices: hot-electron trajectories,velocities and time of flight*, Keaghan Krog, Nathan Johnson, Masaya Kataoka, and Clive Emary (To be submitted to Phys. Rev. B)

- Oral presentations: *Dynamic simulations of hot-electron quantum-optics devices*, Northern Quantum Meeting 2020.

Contents

Part I

Introduction

Chapter 1

Background

For over five decades, advancements in technology have allowed a speed up in the development of quantum mesoscopic physics and furthered our understanding of electronic transport in systems much smaller than the coherence length of an electron. This has opened up new paths to studying the interface between quantum mechanics and bulk macroscopic properties. For a long time, parallels were made between the flow of electrons and the beams of photons in quantum optics. A particle of matter being associated with a wave was first introduce by Louis de Broglie in a series of notes presented to the French Academy of science between 1923-1924 accumulating into his thesis in 1925 [1]. His work would then be confirmed experimentally by the Davisson-Germer experiment [2] in 1928 where electron beams were scattered off nickel, displaying diffraction patterns. This progressed further to an electronic double-slit experiment [3], analogous to Young's double-slit experiment of light [4], where the fabrication of semi-conductors improved such that electronic analogues of famous photonic interferometers could be built. These discoveries laid the foundations for the realisation of electronic interferometers such as Hanbury-Brown-Twiss [5, 6], Mach-Zehnder [7–12], and Fabry-Pérot [13, 14].

An important milestone in the mesoscopic community was the advent of single electron sources [15] analogous to a single photon source. Being able to control single electrons meant that the wave-like properties of electrons could be applied to quantum technology [16, 17] and allows for quantum metrology measurements [18]. However, their application in these electron quantum optics devices has allowed for a similar evolution in this area of study as the single photon source has had in quantum optics. The challenge with this topic is that, due to the quantum properties of the electrons, we can not see what is happening to the electron travelling through these electronic interferometers without destroying their quantum state. The purpose of this thesis is model and dynamically simulate the motion of a electron within the electron quantum optics devices. In particular,

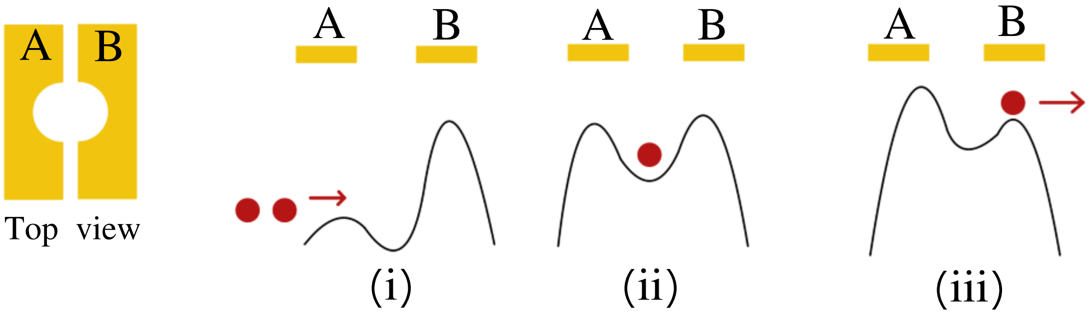

Figure 1.1: The process of emitting a single electron with a tunable barrier pump. Two depletion gates labelled A and B are shown on the left. Gate A has an AC voltage applied to it while gate B has a DC voltage applied to it. The electrostatic potential creates a potential energy barrier which can deplete electrons (red) residing directly below each gate. (i) the loading phase where a strong voltage is applied to gate B while a low voltage is applied to gate A allowing electrons to occupy the zone between the two gates. (ii) The trapping phase where the voltage of gate A is increased trapping an electron and raising its energy. (iii) The emission phase where the voltage on gate A is further increased to give the electron enough energy to overcome the potential energy barrier underneath gate B. The emitted electron has a raised energy higher than the Fermi energy.

we will observe electrons in a high-energy regime and use our results to help aid in the design of future experimental devices. I will be introducing in this chapter the basic concepts and background on the themes of this thesis and provide a general structure on the rest of this work.

1.1 Single-electron sources

The boom in development of quantum optics had an advantage in form of single-photon sources [19, 20]. This had a massive impact on quantum-optic experiments where improvements were made in the understanding of quantum mechanical phenomena by being able to study just a single photon at a time. They also made important steps in the world of quantum information processing [21]. With electronic analogues of quantum-optic style experiments being successfully realised with the implementation of single-electron sources [22], the hope is that this same kind of explosion in development is also found for electron quantum optics.

There are multiple variations in the type of single electron sources such as mesoscopic capacitors [23], Leviton pumps [24], and quantum-dot charge pumps [25]. Their applications range from quantum technology [26] to quantum metrology [27], as well as opening up avenues of exploring interactions and de-phasing. Single electrons are injected into chiral edge channels in the quantum Hall regime, essentially becoming ideal ballistic channels similar to optical paths of photons. The use of these chiral edge channels of the quantum

Hall effect have long been theorised in the study of mesoscopic electron transport [28]. Since these micron scale samples are much smaller than the coherence length of the electronic wave function, quantum mechanical effects can be studied at very low temperatures [6].

The ability to manipulate single electrons plays a vital role in the applications of electrical metrology [29, 18]. The movement of redefining the SI unit system to be dependent on physical constants of nature encourages the improvement of measurement and in turn facilitates the advancement of science and technology. Previously, one Ampere was defined as the current needed to produce a force of 2.7×10^{-7} Nm^{-1} between two infinitely long, parallel conductors placed one meter apart in a vacuum. Now, it is defined by constants of nature; the electrical charge $e = 1.602176619 \times 10^{-19}$ As and the second, which itself is defined by the frequency of energy jumps in a caesium atom [30]. Single electron sources emit a single electron with high accuracy and in order to create one Ampere 6.241509×10^{18} electrons would need to be emitted per second. Currently single electron sources are able to emit a pico Ampere per second but in order to develop a working standard a microAmpere per second would suffice. They also play a vital role in solid state quantum computing [31, 15]. The use of electrons for quantum computing offers a scalable system in which quantum bits (qubits) can be initialised in a quantum two-level system such as Landau Levels, spin, or charge. The motivation behind single-electron sources derives from the success that single-photon sources had in the field of quantum optics and is where inspiration is taken in the pursuit of accurate emissions of single electrons.

In this thesis, we consider a gate-modulated single electron source also known as a tunable barrier pump which comprises of two metallic surface gates applied to the surface of a III-V heterostructure of AlGaAs/GaAs. Within the layers of this structure a two-dimensional electron gas (2DEG) is formed. By applying a strong, negative voltage to the surface gates, the electrostatic potential creates a potential energy barrier at the depth of the 2DEG depleting all electrons below it [32]. A basic set up of these surface gates is shown in Fig. 1.1 where two gates marked A and B show the top down view of their geometry. The emission of an electron can then be broken down into three steps. For step (i) represented in the figure, a strong, negative DC voltage is applied to gate B, depleting all electrons directly below it and is represented by a large potential energy barrier barrier in the figure. A negative AC voltage is applied to gate A and is initially low, so a low potential energy barrier is created, allowing electrons in the 2DEG to occupy the region between the gates. The voltage of gate A is then increased in step (ii), trapping a single electron and raising its energy. In step (iii) the voltage of gate A is further increased in the AC cycle such that the energy of the electron is large enough to overcome the potential

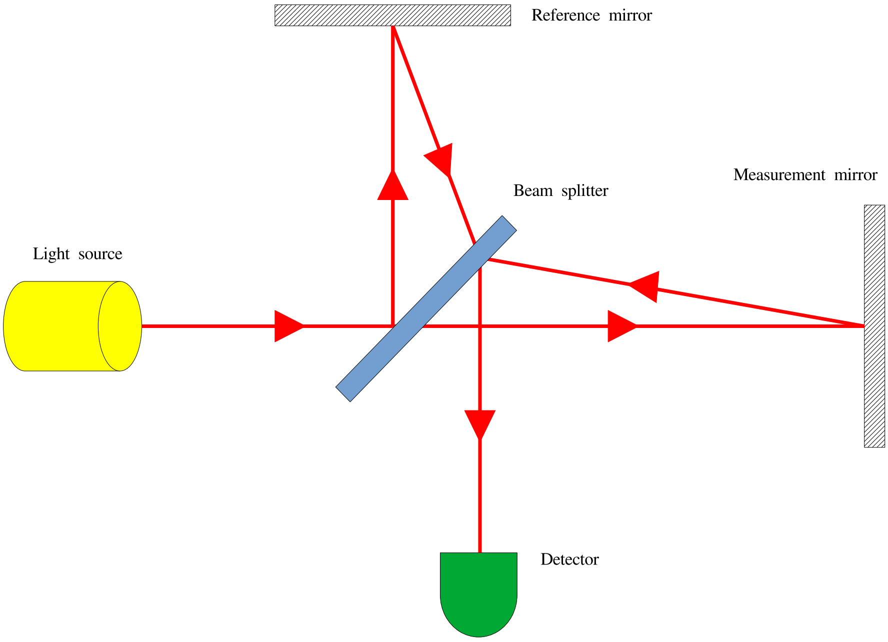

Figure 1.2: Diagram of a Michelson interferometer showing the trajectories (red) of photons emitted from a light source into a beam splitter. The paths rebounded off the mirrors combine back at the beam splitter and the intereference fringe patterns are analysed at the detector [34]. Note: the paths are drawn for visual purposes and do not represent the true trajectories of the photons.

energy barrier created by the gate B.

In addition to the high frequency of emission, the tunability of the emission gate allows for the energy of the electron to be specified. For example, an electron can be injected at energies $\sim$ 100 meV higher than the background electrons in the 2DEG [33]. This is defined as a hot-electron, in reference to its high energy. The advantage of this is that they provide an energetic separation from background electrons, travelling in a state that reduces the likelihood of electron-electron interactions. These hot-electrons can be emitted at a gigahertz frequency and with an accuracy of 1.2 ppm [18].

1.2 Quantum optics

At the start of the 20th century Max Planck postulated that the energy of the light field was quantised, introducing quantum mechanics which became a central pillar in modern physics. It was not until 1960 that the introduction of the laser, a source of monochromatic light, that quantum optics could close the gap between theoretical and experimental research. It is a study of the intrinsically quantum properties of light and provides the experimental capacity for fundamental aspects of quantum mechanics such as coherence and quantum entanglement.

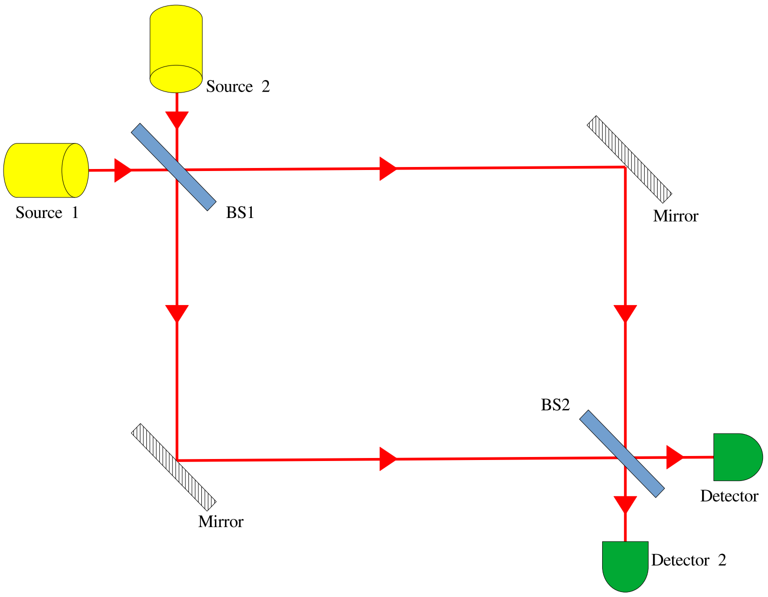

Figure 1.3: A Mach-Zehnder interferometer. Two sources of photon beams are directed to a beamsplitter (BS1). The beamsplitter is set to split the path of the photon into a 50/50 distribution. The path of the photon beam continues and reflects off the respective mirror of each path until interfering at the second beamsplitter (BS2). Two detectors are place in each path to measure the interference [35].

Figure 1.2 shows a diagram of the first interferometer designed in 1887 by Albert A. Michelson [34]. A basic setup, it consists of a light source and a beamsplitter which creates two paths for the photons to follow. Each path is reflected off a mirror and recombined at the beamsplitter. The resultant interference fringe patterns are analysed at the detector. This experiment, conducted by Michelson and Morley, hoped to find evidence for an "aether" which was thought to fill all empty space and provide a medium for light to travel. Although this was proved wrong, the techniques used in their experiment laid the foundation for future interferometers which have become increasingly more complex and used for a broader range of experimental verification and measurements.

In this thesis we will discuss the quantum point contacts designed for an electronic Mach-Zehnder interferometer. A Mach-Zehnder interferometer is used to demonstrate interference by division of amplitude. Figure 1.3 shows a basic diagram of this interferometer. It includes two light sources, both of which combine in a beamsplitter. In this case, the initial coherent beams of light are split between two paths and are recombined at the second beamsplitter, after which the intensity of the light beams are measured in the detectors. By changing the path length or introducing a medium through which the light can travel, the beam will acquire a phase shift which can be measured.

1.3 Electron quantum optics

The history of electron quantum optics has relied much on drawing similarities between electrons and photons and creating electronic analogues of photonic systems. But, there are significant difference between photons and fermionic particles. The problem with treating electrons like photons lies with the presence of the Fermi sea and Coulomb interaction. Most single electron sources emit an electron at an energy similar or below the Fermi level, meaning that the injected particle will interact with the sea of electrons. There is also the chance of scattering due to phonon emission [36]. These interactions, as well as the motion in the quantum Hall edge channel [37], lead to decoherence [38].

There are numerous solutions which have been brought forward to overcome these problems such as single electron sources based on voltage pulses [24, 39] and surface acoustic wave driven single electrons [40, 41]. However, in this thesis we will focus on single electron sources using a tunable-barrier pump which have primarily been used for metrology applications [23, 18, 42]. A quantum current standard has been well sought after for over 25 years and electrons pumps have been rigorously studied as their single electron emissions create a macroscopic current that can be measured accurately by controlling the frequency of emission and number of electrons emitted. But, it is found that they either do not have the accuracy or a high enough current output [43]. However, a tunable-barrier electron pump has been shown to acquire this ideal combination [18] satisfying the requirement of accuracy to the 10^{-8} level [44]. In contrast to previous sources, this type of single-electron source allows the electron to be emitted with an energy $\sim 100\,\mathrm{meV}$ above the Fermi level into the outermost edge state [45, 46, 33]. The application of a strong magnetic field also suppresses phonon emission essentially isolating the electron and enabling a picture of a simple, single-particle experiment [36]. These electrons have been aptly named "hot-electrons", opening up a new energy domain for which the fundamental electron behaviour in solid-state can be studied. We refer to these devices which use these high energy electrons as hot-electron quantum-optics (HEQO) devices.

1.4 Thesis overview

We begin in part I where the main ideas and background will be introduced. We then continue with two main investigations that will be considered in this thesis: part II comprising the electrostatic modelling of experimental devices and part III comprising dynamic simulations of such devices. We then finish in part IV with a conclusion and future work.

Here I will give a brief overview of the two main parts of this thesis.

Part II: Electrostatic model

In order to create working dynamic simulations of single electrons in HEQO devices, we need to have an understanding of the potential energy that is felt by the injected hot-electrons to study their transport within experimental devices. Therefore, to understand the behaviour of these hot-electrons, we require an accurate and efficient modelling of their electrostatic environment.

Electron quantum optic devices use a variety of techniques to manipulate the behaviour of electrons. In Chapter 3 we study two fabrication techniques used in electron quantum optic devices: etching and surface gates. We look at each one separately and follow the work of Davies [47, 32] to understand how both of these techniques can affect the energetic landscape seen by electrons. We apply these methods to simple models of devices which have characteristic physical properties of the HEQO devices we will be studying.

We expand on this further in Chapter 4 by introducing a method that allows us to calculate the electrostatic potential for devices that use both surface gates and etching. We call this the projected surface method and introduce it with simple models of quantum wires. We find that it gives a good approximation when compared to other methods such as the finite element method to calculate what the electrostatic potential looks like in the region of the devices occupied by the electrons.

We then take the projected surface method and apply it to a realistic device known as the time-of-flight experiment [45, 48] in Chapter 5. This experiment allows for a time resolved method of calculating the drift velocity of an electron. We test our method by performing a semi-classical analysis on the calculated potential due to the geometry of etching and patterning of depletion gates. We show that we can calculate the velocity of the electron with good approximation compared to experimental data. This analysis also allows us to make observations that couldn't be measured in experiment and offer data which could aid in the design of future experiments.

Part III: Dynamic simulations

We then look to study how a hot electron will travel around the energetic landscape calculated using the projected surface method for experimental devices. We begin in chapter 6 where we outline the process of modelling an electron as a Gaussian wave packet and calculate how it evolves in a system with a potential energy calculated for the experimental device. This follows the work of Andrea Bertoni, who we have collaborated with in an effort to adapt this numerical method to hot electrons. In this chapter we introduce the Trotter-Suzuki factorisation and the Fourier split step method and how they can be used to solve the Schrödinger equation efficiently. We show examples of how the simulation will look and run while exploring some limitations to the numerical method when considering hot electrons.

We continue to then apply the simulation to an experimental device. We follow on from part II by doing a dynamic simulation of the time of flight experiment. We then have an idea of how the hot electron will travel in this device and are able to get a time resolved method for the velocity of the electron. This will allow us to compare to both the experimental data and our analysis done on the electrostatic potential calculated for this device.

Finally, we look at a fundamental component of electronic interferometry: the quantum point contact, in chapter 8. we look at a simple quantum point contact model where a saddle-point potential is created and observe how the wave packet in the simulation interacts with such a system. We are able to conduct multiple simulations, each for a given energy, for variations of the design to find how the constriction in the potential energy affects the transmission rate. We then adapt this design to include more characteristics which are used mostly in HEQO devices. We conduct multiple simulations again, however now we study how the magnetic field affects the transmission rate. We finally look at a realistic quantum point contact, the model of which was given to us by Masaya Katoaka and Patrick See. We perform simulations on this model and then look at how we can adapt and redesign, taking into consideration what we have learnt from the previous variations of designs we simulate.

Chapter 2

Electronic transport

In this chapter I will introduce the theoretical background and derivations required to understand the systems we wish to study in this thesis. It will provide the building blocks which allow us to create models and perform dynamic simulations of experimental electron quantum optic devices.

2.1 Mesoscopic physics

There are a vast array of questions a scientist can ask to inspire their investigations. Arguably, one of the most common questions is: How small can we make this until it breaks? This question was asked of the conductance, G, of a two-dimensional conductor with a width W and length L. The equation of conductance is well known as

$$G = \frac{\sigma W}{L} \tag{2.1}$$

in which the conductivity of the material is given as σ. The something the investigation looked to break was the ohmic behaviour of the conductor but not too small to be considered microscopic. This goldilocks zone is referred to as mesoscopic.

There are three characteristic length scales:

- The de Broglie wavelength, λ_B.
- The mean free path, L_m.
- Phase relaxation length, L_ϕ.

When the dimensions of the conductor are larger than these characteristic length then ohmic behaviours are observed. The de Broglie wavelength refers to dual nature of wave-particles, a fundamental concept crucial for electron quantum optics. It is given as

$$\lambda_B = h/mv, \tag{2.2}$$

associated with the energy of the particle and is dependent on the velocity, v, and the mass, m, of the particle.

The mean free path is the distance the particle will travel before it loses its initial momentum given by

$$L_m = v\tau_m, \tag{2.3}$$

which again is dependent on the velocity but now also the momentum relaxation time, τ_m.

The phase relaxation length, similar to the mean free path, is the distance the particle travels before it loses its initial phase governed by the phase relaxation time τ_ϕ. If the phase relaxation time is smaller than the momentum relaxation time then we can describe this length as

$$L_\phi = v\tau_\phi, \tag{2.4}$$

which is often the case for high-mobility semiconductors. However, if we were observing electrons in low-mobility semiconductors, where the phase relaxation time is larger than the momentum relaxation time, then it results in a phase relaxation length of

$$L_\phi^2 = \frac{v^2\tau_m\tau_\phi}{2}. \tag{2.5}$$

This is a result of the motion of electrons over a phase-relaxation time not being ballistic. Once an amount of time equal to the momentum relaxation time has passed, the velocity of each electron trajectory is completely randomised. To calculate the average distance travelled, the root mean squared distance is calculated, resulting in an equation of the phase relaxation length as shown in Eq. 2.5 [49].

The variation in these length scales differs hugely from material to material as it is affected by temperature, magnetic fields etc. A landmark experiment studying the mesoscopic transport phenomena used a ring-shaped conductor made from a patterned polycrystalline gold film. Its dimensions were 100 nm in diameter and 40 μm thick. It showed oscillations in the resistance of the ring with changes in the magnetic field applied to it. However, as valuable as these pioneering experiments were they were conducted mostly on metal. Over the past 50 years most of the work has been performed on semiconducting heterostructures. In particular, I will be focussing my research on AlGaAs/GaAs heterostructure devices. In addition, our attention will be on hot-electrons which have higher

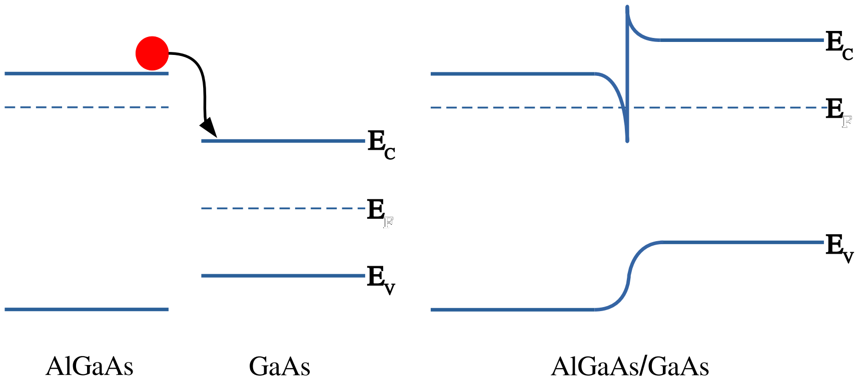

Figure 2.1: Energy bands diagram showing the conduction band, valence band, and Fermi energy for the n-doped AlGaAs and GaAs layers before (left) and after (right) they come into contact. AlGaAs has a higher Fermi energy than GaAs, so as they come into contact their is a spill over of negatively charged electrons leaving behind positively charge holes. This separation in charges induces an electrostatic potential which causes the conduction and valence bands to bend. The Fermi energy balances out through both layers and leaves behind a layer of electrons between the intersection known as the 2DEG.

energy than their “cold”-electron (i.e. electrons closer to the Fermi energy) counterparts. This means their source of decoherence is very different and they have very short lifetimes, typically of the order of picoseconds [45]. In this thesis we will assume that the size of the hot-electron quantum optics devices have paths the hot-electron will travel along with a length $L < L_\phi$, and as such the effects of phase relaxation can be ignored. The mean free path of these hot-electrons are difficult to approximate, especially as there are not functioning MZI experiments to provide us the results. However, under various mechanisms that are required for performing experiments with hot-electrons, an estimate can be made that they have mean free path lengths of the order of tens of microns [50]. We also note here that in this thesis we do not include scattering of hot-electrons to lower energy levels. However, a possible approach would require combining a classical path with a classical rate equation to get some idea of the evolution, acquiring a “semi-classical approach” [36, 51].

2.2 AlGaAs/GaAs heterostrucure and the two-dimensional electron gas

The Heterostructure of the devices I will be presenting are modelled around the materials AlGaAs (Aluminium Gallium Arsenide) and GaAs (Gallium Arsenide). In terms of the characteristic lengths, it is found that for GaAs the mean free path is $L_m \approx 10\,\text{nm}$ [52] and for the phase relaxation length it is approximately the same. The generic layout involves a cap layer of GaAs, followed by an n-doped layer of AlGaAs where the source of the electrons is found. Below this is a spacer layer of undoped AlGaAs with GaAs being the foundation of the device.

The formation of the two-dimensional electron gas (2DEG) occurs because of the n-doped AlGaAs layer. Ignoring the undoped AlGaAs layer for now, the doped layer has a high excess of negatively charged donors (electrons) causing the Fermi level to be much higher than the GaAs. As the two come into contact there is a spillage of electrons from the AlGaAs into the GaAs. The transfer of the electrons leaves behind positively charged donors (holes) which creates a separation of charges inducing an electrostatic potential. The conduction and valence bands begin to bend due to the potential and peak because of the sharp rise in the electron density at the interface of the two materials which can be seen in Fig. 2.1 thus forming a thin conducting layer known as the 2DEG. It can then be manipulated by the application of a surface gate with a voltage, V_g, which is placed on top of the cap layer of GaAs.

The vital characteristic of this heterostructure is the low scattering rate. With the introduction of the undoped layer of AlGaAs, the spacer layer, the scattering rate can be lowered further by increasing the separation of charges. This does come at a cost, however, of reducing the carrier concentration. Typically, with these materials the carrier concentration is found to be $2 \times 10^{11}\ \text{cm}^{-2}$ and $2 \times 10^{12}\ \text{cm}^{-2}$ [49].

2.3 Classical Hall effect

We have a source of electrons found within a 2DEG in an AlGaAs/GaAs heterostructure and we look now to study the transport of electrons within these mesoscopic devices. We start by observing a classically charged particle in a uniform magnetic field. Within a 2DEG, each particle has a charge q, mass m, and velocity of $\mathbf{v}$. However, when a uniform magnetic field B is applied perpendicular to this two-dimensional plane of electrons, the particles start to move in a circular motion. With a mass and a motion, we can describe the force felt by the electron know as the Lorentz force. This describes the centripetal

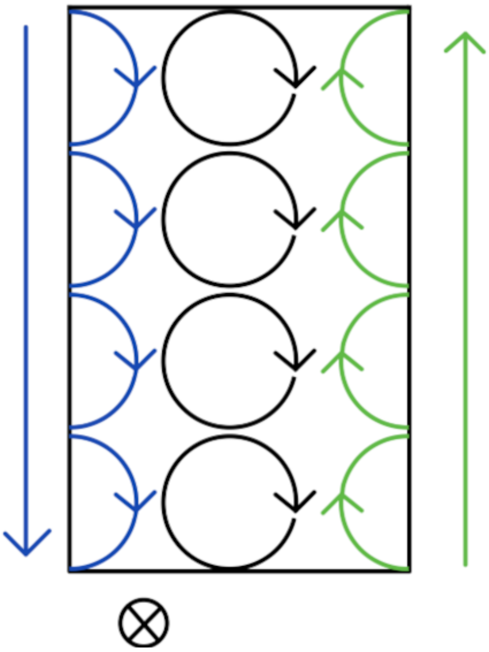

Figure 2.2: Cyclotron orbit of an electron within an electron gas with a magnetic field applied perpendicular to the plane in the direction labelled. The electrons in the centre travel in a circular motion, the radius of which depends on the magnetic field. The electrons closer to the edge collide with the boundary where the disruption of the orbit causes it to skip along the edge. These skipping orbits are chiral as the left side (blue) travels downwards and the right side (green) travels upwards.

force of the particle toward the centre of its orbit and is described as:

$$\mathbf{F}_L = q\mathbf{v} \times \mathbf{B}. \tag{2.6}$$

The circular motion is expressed as the cyclotron orbit which we can deduce the radius of by expressing the Lorentz force in terms of mass and the centripetal acceleration

$$q\mathbf{v} \times \mathbf{B} = -m\frac{v^2}{r}\hat{r}, \tag{2.7}$$

which, taking **v** and **B** to be orthogonal we find the cyclotron radius

$$r_c = \left|\frac{mv}{qB}\right| \tag{2.8}$$

and is rearranged to form the cyclotron frequency

$$\omega_c = \frac{v}{r_c} = \frac{qB}{m}. \tag{2.9}$$

We note here that the sign of the cyclotron frequency has a physical meaning. For $\omega_c > 0$ we find the orbit travelling in a clockwise motion while for $\omega_c < 0$ implies a counter-clockwise orbit. These directions become important when considering the type of orbits when the motion is restricted to a two-dimensional plane.

The first of two orbits we consider occurs when the particle is far from any potential barrier and the orbit is unimpeded. This is shown as the black, full cyclotron orbit in Fig. 2.2. Although the electron is moving, its movement across the plane has a net velocity of zero. When an orbit comes into contact with the potential barrier it rebounds elastically and the orbit is halved and travels along the edge as shown by the blue and green orbits in the figure. Here we observe a net velocity that is dependent on the magnetic field and is known as a skipping orbit for the“bouncing” motion along the barrier. The skipping orbits are observed to be chiral as the directions of travel on opposing boundaries are opposite to each other.

2.4 Quantum Hall effect

We have seen how in the classical picture we can expect a charged particle to behave in a magnetic field. However, we are most interested in the quantum perspective, especially as we observe systems where the temperature is lowered to cryogenic levels and the magnetic fields are very strong. The first experiment exploring the quantum regime of the Hall effect was performed by Klaus von Klitzing [53]. Experimenting on a 2DEG in a semiconductor, it was discovered the energy levels of electron orbitals were quantised in integer multiples of h/e^2, two constants of nature: h Planck’s constant and e the electron charge. Further experiments then showed that these electron orbitals can also be quantised in fractional multiples of h/e^2 [54]. We focus on the integer quantum Hall effect to consider how a charge particle may behave in a magnetic field from the quantum viewpoint. Klitzing showed that, for certain ranges of magnetic fields there are plateaus in the resistivity felt by the 2DEG. These plateaus would be joined together by sharp jumps with a positive proportionality between the increase in the magnetic field and an increase in the resistance. The experiment was so accurate that these plateaus are used as standards for measuring resistance [55].

In this thesis we will be observing systems in the quantum Hall regime where we will be studying experiments performed in refrigerators at cryogenic temperatures of around $T \approx 4\,\mathrm{K}$ [45] and magnetic fields in excess of $5\,\mathrm{T}$ which is usual for electronic interferometers [7].

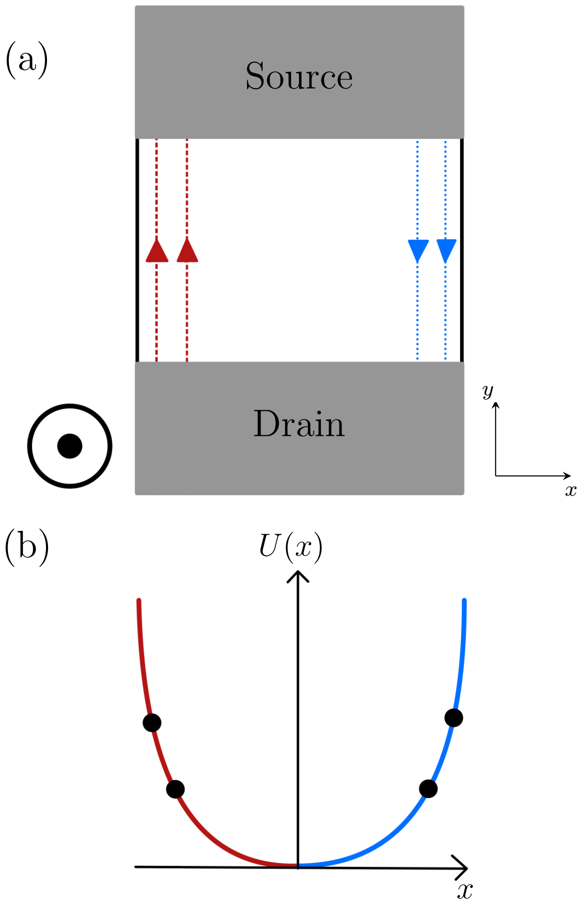

Figure 2.3: (a) A simple bar geometry with the edge channels shown as the red, dashed lines and the blue dotted lines. Multiple edge channels are displayed representing the different energies and the chirality can be seen from the opposed directions for either edge, as described in Fig. 2.2. (b) The parabolic potential energy, $U(x)$, plotted for x to match with the geometry in (a). Black dots are plotted to represent the corresponding positions of energy for the edge channels in (a) directly above.

2.5 Landau levels and edge states

Observing electrons found within a 2DEG, such as the one in Fig. 2.3a (with contacts applied to the top and bottom), we can describe them by

$$\left[E_c + \frac{1}{2m_e^*}(i\hbar\nabla + e\mathbf{A})^2 + U(\mathbf{R})\right]\Psi(\mathbf{R}) = E\Psi(\mathbf{R}) \tag{2.10}$$

where E_c is the bulk band bottom energy, $U(\mathbf{R})$ is the confinement energy in each of the three-dimensions, $\mathbf{R} = (x, y, z)$, $\mathbf{A}$ is the vector potential and $m_e^* = 0.067m_e$ is the effective mass of an electron in GaAs [49]. Here we denote the electron charge as $e > 0$.This is the

Schrödinger equation, where the Hamiltonian is

$$\hat{H}(\mathbf{R}) = E_c + \frac{1}{2m_e^*}(i\hbar\nabla + e\mathbf{A})^2 + U(\mathbf{T}). \tag{2.11}$$

For the continuity in later chapters we choose a system which is unconfined in the y-direction, which means that the y-component is zero such that

$$U(\mathbf{R}) = U(x) + U(z) \tag{2.12}$$

where we have assumed that the potentials are decoupled. We want to describe a system which we will be observing later on with our HEQO devices and as such we will be working in the quantum Hall regime, with a strong magnetic field. We choose to work in the Landau gauge, however there are two possible choices:

$$\mathbf{A}_L = B(0, x, 0), \tag{2.13}$$

$$\mathbf{A}'_L = B(-y, 0, 0). \tag{2.14}$$

depending on the direction of travel. Because of our confining potential in the x dimension, the direction of motion will be in the y direction and we choose the Landau Gauge $\mathbf{A}_L = B(0, x, 0) = eBxe_y$.

We expand on the Hamiltonian in Eq. (2.11) to

$$\hat{H}(\mathbf{R}) = E_c + \frac{1}{2m_e^*}(\hat{p} - eBxe_y)^2 + U(x) + U(z) \tag{2.15}$$

which is separated into the respective components

$$\hat{H}(\mathbf{R}) = E_c + \frac{1}{2m_e^*}p_x^2 + \frac{1}{2m_e^*}(p_y^2 - eBx) + U(x) + \frac{1}{2m_e^*}p_z^2 + U(z). \tag{2.16}$$

We introduce the quantum numbers n and k which represent the Landau level and the momentum of our system. We can then solve the Schrödinger equation

$$\hat{H}(\mathbf{R})\Psi_{n,k}(\mathbf{R}) = E_{n,k}\Psi_{n,k}(\mathbf{R}) \tag{2.17}$$

with the solution

$$\Psi_{n,k}(\mathbf{R}) = \chi_{mk_y}(x)\psi_{k_y}(y)\phi(z). \tag{2.18}$$

This separation of the x, y, z components allow us to look closer at how the electrons are confined in each dimension. We first note that the 2DEG we are studying is only allowed to freely propagate in the x and y directions, meaning that there is a strong confinement. The confining potential $U(z)$ can be modelled as an infinite square well. To model the tight confinement we assume this well is extremely narrow and that energy levels are found far apart from one another. In such a case, the electrons cannot move between these energy levels and are quantised so we assume a lowest energy sub-band for our calculations.

In the y direction, the electrons are allowed to propage freely and are only defined by the momentum k_y. An unconfined electron can be described by a plane wave

$$\psi_{k_y}(y) = \frac{1}{\sqrt{L_y}} e^{ik_y y} \tag{2.19}$$

which is normalised over the length of the conductor L_y. For the x direction there are some slight complications. There is weak parabolic confinment which means that the electrons are quantised in terms of Landau level, m. The difference between Landau levels is quite large at around 10 meV such that we assume that the electron will stay in the Landau level it is in. Here we assume it is in the lowest. We can also account for some movement in the x direction due to the weak confinement so we include the momentum k. We use a weak parabolic confinement

$$U(x) = \frac{1}{2} m_e^* \omega_x^2 x^2, \tag{2.20}$$

governed by the confinement frequency ω_x, with an example of the potential $U(x)$ shown in Fig. 2.3b. For the x direction we find the Hamiltonian becomes

$$\hat{H}_{k_y} = \frac{1}{2m_e^*}(\hbar k_y - eBx)^2 + \frac{1}{2m_e^*} p_x^2 + \frac{1}{2} m_e^* \omega_x^2 x^2, \tag{2.21}$$

with the solution

$$\hat{H} k_y(x) \chi_{n,k_y}(x) = E_k \chi_{n,k_y}(x). \tag{2.22}$$

Now, $\chi_{n,k_y}(x)$ represent the eigenfunction of the Hamiltonian. In order to expand Eq. (2.21) further we introduce two characteristic properties to simplify our calculations. The cyclotron frequency

$$\omega_c = \frac{eB}{m_e^*} \tag{2.23}$$

and the guiding wave-centre coordinate

$$x_G(k_y) = \frac{\omega_c^2}{\mathit{\Omega}^2} \frac{\hbar k_y}{eB} = \frac{\omega_c}{\mathit{\Omega}^2} \frac{\hbar k_y}{m_e^*} \tag{2.24}$$

where we have introduced also the compound frequency $\varOmega^2 = \omega_c^2 + \omega_x^2$ which includes the confining frequency in the x direction. The Hamiltonian now becomes

$$\begin{aligned}\hat{H}_n k_y(x) &= \frac{1}{2m_e^*}(\hbar k_y - m_e^*\omega_c x)^2 + \frac{1}{2m_e^*}p_x^2 + \frac{1}{2}m_e^*\omega_x^2 x^2 \\ &= \frac{1}{2m_e^*}p_x^2 + \frac{\hbar^2 k_y^2}{2m_e^*} + \frac{1}{2}m_e^*\omega_x^2 x^2 \\ &= \frac{1}{2m_e^*}p_x^2 + \frac{1}{2m_e^*}\left[\frac{\varOmega^4}{\omega_c^2}m_e^* x_G^2\right] - \varOmega^2 m_e^* x_G x + \frac{1}{2}m_e^*\omega_x^2 x^2 \\ &= \frac{1}{2m_e^*}p_x^2 + \frac{1}{2m_e^*}\varOmega^2\left[\frac{\varOmega^2}{\omega_c^2}x_G^2 - 2xx_G + x^2\right] \\ &= \frac{1}{2m_e^*}p_x^2 + \frac{1}{2m_e^*}\varOmega^2\frac{\omega_x^2}{\omega_c^2}x_G^2 + \frac{1}{2}m_e^*\varOmega^2(x-x_G)^2 \\ &= \frac{1}{2m_e^*}p_x^2 + \frac{\hbar^2 k_y^2}{2m_e^*}\frac{\omega_x^2}{\varOmega^2} + \frac{1}{2}m_e^*\varOmega^2(x-x_G)^2. \end{aligned} \tag{2.25}$$

This Hamiltonian resembles a harmonic oscillator with a displacement governed by the guiding wave-centre x_G. This has well known eigenfunctions

$$\chi_{n,k_y}(x) = \frac{1}{l_\varOmega}u_n\left(\frac{x - x_G(k_y)}{l_\varOmega}\right), \tag{2.26}$$

with the effective confinement length $l_\varOmega = \sqrt{\frac{\hbar}{m_e^*\varOmega}}$, defining the size of the parabolic trap, and the coefficient which includes the Hermite polynomials H_n

$$u_n(s) = \frac{1}{\sqrt{2^n n!}}\frac{1}{\pi^{1/4}}e^{-s^2/2}H_n(s). \tag{2.27}$$

As we will only be considering the lowest Landau level then $H_0(s) = 1$ and we denote

$$u_0(s) = \frac{e^{-s^2/2}}{\pi^{1/4}} \tag{2.28}$$

and we get the eigenfunction

$$\chi_{0k_y}(x) = \sqrt{\frac{1}{l_\varOmega}\pi^{1/2}}\exp\left[-\frac{1}{2}\left(\frac{x-x_G}{l_\varOmega}\right)^2\right]. \tag{2.29}$$

We solve the Schrödinger equation by multiplying Eq. (2.22) by the complex conjugate of the eigenfunction, $\chi^*_{n'k'_y}(x)$ giving

$$\chi^*_{n',k'_y}(x)\hat{H}_{n,k_y}\chi_{n,k_y}(x) = \chi^*_{n',k'_y}(x)E_k\chi_{n,k_y}(x). \tag{2.30}$$

We then integrate over x

$$\begin{aligned}
&\int \chi^*_{m',k'_y}(x)\hat{H}_{k_y}\chi_{n,k_y}(x)\mathrm{d}x = \int \chi^*_{n',k'_y}(x)E_k\chi_{n,k_y}(x)\mathrm{d}x \\
\Rightarrow &\int \chi^*_{n',k'_y}(x)\hat{H}_{k_y}\chi_{n,k_y}(x)\mathrm{d}x = E_k\int \chi^*_{n',k'_y}(x)\chi_{n,k_y}(x)\mathrm{d}x \\
\Rightarrow &\int \chi^*_{n',k'_y}(x)\hat{H}_{k_y}\chi_{n,k_y}(x)\mathrm{d}x = E_k\delta_{n'n}\delta_{k'_yk_y} \qquad (2.31)
\end{aligned}$$

and get the Kronecker delta functions where $\delta_{n'n} = 1$ if $n' = n$ and zero otheriwse (and with momentum). In this case, $n' = n$ and $k'_y = k_y$ in order to have a non-zero solution.

We then found that we can describe the dispersion relation of the electrons as

$$\begin{aligned}
E_k = &\frac{1}{l_\Omega\pi^{1/2}}\int \exp\left[-\frac{1}{2}\left(\frac{x-x_G(k)}{l_\Omega}\right)\right] \\
&\times\left[\frac{1}{2m_e^*}p_x^2 + \frac{\hbar^2k_y^2}{2m_e^*}\frac{\omega_y^2}{\Omega^2} + \frac{1}{2}m_e^*\Omega^2(x-x_G)^2\right]\exp\left[-\frac{1}{2}\left(\frac{x-x_G(k)}{l_\Omega}\right)\right]\mathrm{d}x \\
= &\frac{1}{l_\Omega\pi^{1/2}}\int \chi_{n,k_y}\exp\left[-\left(\frac{x-x_G(k)}{l_\Omega}\right)\right]\sqrt{\frac{1}{l_\Omega\pi^{1/2}}}\left[+\frac{\hbar^2k_y^2}{2m_e^*}\frac{\omega_y^2}{\Omega^2} + \frac{1}{\hbar\Omega}\right]\mathrm{d}x \qquad (2.32)
\end{aligned}$$

after calculating for the momentum operator. The resulting dispersion relation is given as

$$E_k = \frac{1}{2}\hbar\Omega + \frac{\hbar^2k_y^2}{2m_e^*}\frac{\omega_x^2}{\Omega^2} \qquad (2.33)$$

which will describe the systems we will be studying.

2.5.1 Velocity

We can calculate the velocity from the dispersion relation as

$$v(n,k_y) = \frac{1}{\hbar}\frac{\partial E(n,k)}{\partial k_y} = \frac{\hbar k_y}{m_e^*}\omega_x^2\Omega^2 \qquad (2.34)$$

which describes the drift velocity of electrons in our conductor with a strong magnetic field applied perpendicular to its motion. In this thesis, we will be conducting dynamic simulations of electrons travelling in edge-channels described by the energy dispersion. However, we have derived the eigenfunctions of the Schrödinger equation for a parabolic confinement. This confinement offers a good description of narrow regions where electrons can travel, such as quantum wires, but we will see that this isn't always the case in the devices we wish to study. In wider confinement potentials we won't be able to obtain analytic solutions but will be able to approximate a solution in high magnetic fields.

If the confinement were absent, where $U(x) = 0$, then the energy dispersion becomes[49]

$$E_{n,k} = E_c + (n + \frac{1}{2})\hbar\omega_c. \tag{2.35}$$

By performing the lowest order perturbation theory we can include the confining potential

$$E_{n,k} \approx E_c + (n + \frac{1}{2})\hbar\omega_c + \langle n, k| U(x) |n, k\rangle \tag{2.36}$$

where the state (n, k) is centered around x_k. Assuming that the confining potential is uniform and constant for each state then

$$E_{n,k} = E_c + (n + \frac{1}{2})\hbar\omega_c + U(x_k) \tag{2.37}$$

where we have mapped the coordinates of x points to a wave number by $x_k = \hbar k/eB$. Now, we can see the relation to the semi-classical view of the cyclotron orbits where away from boundaries the states look like Landau levels which are unconfined and have a full cyclotron orbit. However, near the edges we find edge states which are channels which electrons travel along.

In this case, the velocity can be calculated as

$$v(n, k) = \frac{1}{\hbar}\frac{\partial E(n, k)}{\partial k} = \frac{1}{\hbar}\frac{\partial U(x_k)}{\partial k}\frac{\partial x_k}{\partial k} = \frac{1}{eB}\frac{\partial U(y)}{\partial x} \tag{2.38}$$

which relates the motion of the electron to the gradient of the potential which will play an important role in our analysis of HEQO devices later on.

2.6 Landauer-Büttiker formalism

The Landauer formalism is used to describe the mesoscopic transport of a system where a current through a conductor is expressed by the probability that the electron is transmitted from one contact to another. It was first applied to tunnelling junctions [56]. When considering large samples that follow Ohm's law, we can describe the conductance through a sample as

$$G = \frac{\sigma W}{L} \tag{2.39}$$

where W is the width of the sample and L is the length, which is dependent on the properties of the system in question. However, we now consider the quantum view for electrons.

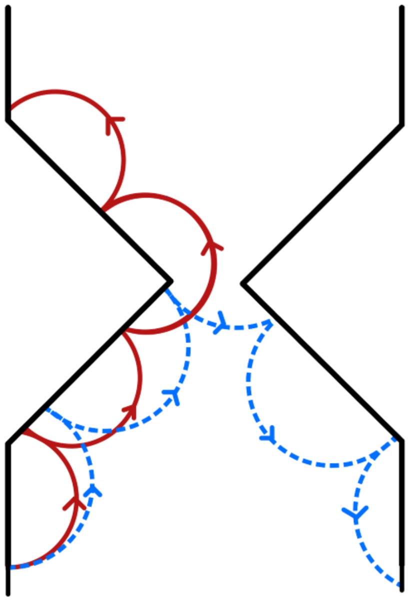

Figure 2.4: Quantum point contact showing a constriction between two conducting region of a 2DEG. The boundary edges (black) are constricted to a narrow point while in the semi-classical view we have represented the skipping orbits can travel along the boundaries to either be transmitted through (solid, red) or reflected away (dashed, blue) from the constricted region.

We will consider two conducting regions separated by a constriction as shown in Fig. 2.4. This model defines a quantum point contact where we have constricted a two-dimensional region of transport into one-dimension. Represented in the figure are the cyclotron orbits for electrons lying close to the boundary representing the semi-classical view of how the electrons interact with the constriction showing a path the electron can follow to be transmitted (solid, red skipping orbit) or be reflected (dashed, blue skipping orbit).

To determine the current in the constriction we consider a cube in k-space which is centred around the three-dimensional wavevector $\mathbf{k}$. The number of states in this cube which are available, taking into account the 1/2 spin of electrons and the Pauli principle, is $2_s(\mathcal{V}\ \mathrm{d}k_x\ \mathrm{d}k_y\ \mathrm{d}k_z)/(2\pi)^3$, where 2_s represents the atomic orbital for two electrons in an s-type subshell. We define the fraction of filled states in the cube as the filling factor $f(\mathbf{k})$ and the usual notation of particle density n, energy density ϵ, and current density $\mathbf{j}$. These values can be calculated by

$$\begin{bmatrix} n \\ \epsilon \\ \mathbf{j} \end{bmatrix} = \int 2_s \frac{\mathrm{d}^3 k}{(2\pi)^3} \begin{bmatrix} 1 \\ E(\mathbf{k}) \\ e\mathbf{v}(\mathbf{k}) \end{bmatrix} f(\mathbf{k}). \tag{2.40}$$

We adapt this slightly to change the integration over k_y to be a summation over the discretised value k_y^n such that

$$\int \frac{\mathrm{d}k_y}{2\pi} \to ab \sum_n ... \tag{2.41}$$

which we then get the full current by multiplying the current density by the cross-section area $a_\infty b_\infty$ (where we have assumed the waveguide is ideal as $x \to \pm\infty$) to get

$$I = 2_s e \sum_n \int_{-\infty}^{\infty} \frac{\mathrm{d}k_x}{2\pi} v_x(k_x) f_n(k_x). \tag{2.42}$$

The filling factors within the current are affected by the open channels. For fully closed channels the electrons which pass through the cross-section area are reflected and also subsequently pass the same cross-section. There is then an equal amount of right and left travelling electrons which implied that the filling factors are identical. In this case the velocities are opposite and we get a net zero current.

For open channels we denote that electrons with $k_x > 0$ and travelling from the left reservoir have a filling factor $f_L(E) \equiv f_F(E - \mu_L)$ and for the right reservoir we have $f_R(E) \equiv f_F(E - \mu_R)$ where $k_x < 0$ and f_F is the Fermi-Dirac distribution. The dependence now on energy for the filling factor over the wavevector k_x means we can cancel out the velocity as

$$v_x = \frac{1}{\hbar}\frac{\partial E}{\partial k_x} \tag{2.43}$$

$$\Rightarrow \mathrm{d}E = \hbar v(k_x)\mathrm{d}k_x \tag{2.44}$$

such that we can denote the velocity as

$$I = \frac{2_s e}{2\pi\hbar} \sum_{n:open} \int \mathrm{d}E \left[f_L(E) - f_R(E)\right]. \tag{2.45}$$

Integrating over energy gives a factor $\mu_L - \mu_R$, a difference in the chemical potential which corresponds to the voltage difference applied $V = (\mu_L - \mu_R)/e$, which drives the current. This gives a current value

$$I = \frac{2_s e}{2\pi\hbar} N_{open}(\mu_L - \mu_R). \tag{2.46}$$

This integration is performed when we assume that temperature tends to zero. When $V = 0$ there is no current as the system will be in a state of thermodynamic equilibrium. As the factor $\mu_L - \mu_R$ will be the same for all open channels, we find that the current is proportional to the number of open channels and voltage and we can describe the current by

$$I = G_Q N_{open} V \tag{2.47}$$

where we introduce the conductance quantum $G_Q = 2_s e^2/(2\pi\hbar)$. This shows that the conductance of the system is quantised and is not dependent on the properties of the material.

First let us separate the wave function in the left, L, and the right, R, conducting region [57]

$$\psi(x_L, y_L) = \sum_n \frac{1}{\sqrt{2\pi\hbar v_n}} \Phi_n(y_l) \left[a_{Ln} e^{ik_x^{(n)} x_L} + b_{Ln} e^{-ik_x^{(n)} x_L}\right] \tag{2.48}$$

$$\psi(x_R, y_R) = \sum_m \frac{1}{\sqrt{2\pi\hbar v_m}} \Phi_m(y_R) \left[a_{Rm} e^{-ik_x^{(m)} x_R} + b_{Rm} e^{-ik_x^{(m)} x_R}\right] \tag{2.49}$$

where we have denoted the transport channels in the left and right waveguides as n and m respectively. We have also introduced the amplitudes of the plane waves as a and b. The energies of the transverse motion fixes the value of the wave vector $k_x^{(n)} = \sqrt{2m(E - E_n)/\hbar}$ (and similarly for m). Thus, the transport is due to propagation and we have to define the wave vector as real. As such, there will be a finite number of channels which are open for transport at a fixed energy E.

The amplitude coefficients can be separated into waves which are initialised from the respective reservoirs a_{Ln} and a_{Rm} and waves which that have interacted with the scattering region b_{Ln} and b_{Rm}. The latter can either be transmitted through the scattering region or reflected. These coefficients are therefore not independent such that

$$b_{\alpha l} = \sum_{\beta=L,R} \sum_{l'} s_{\alpha l, \beta l'} a_{\beta l'} \tag{2.50}$$

where $l = n, m$. Depending on the number of open channels N_L and N_R, the proportionality coefficients are combined into a $(N_L + N_R) \times (N_L + N_R)$ scattering matrix

$$\hat{s} = \begin{pmatrix} \hat{s}_{LL} & \hat{s}_{LR} \\ \hat{s}_{RL} & \hat{s}_{RR} \end{pmatrix} = \begin{pmatrix} \hat{r} & \hat{t}' \\ \hat{t} & \hat{r}' \end{pmatrix}. \tag{2.51}$$

Expanding the equation for current we get

$$\begin{aligned}
I = 2_s e \sum_n \int_0^\infty \frac{\mathrm{d}k_x}{2\pi} v_x(k_x) f_L(E) \\
+ \int_{-\infty}^{0} \frac{\mathrm{d}k_x}{2\pi} v_x(k_x)[R_n(E) f_L(E) + (1 - R_n(E)) f_R(E)] \\
= 2_s e \sum_n \int_0^\infty \frac{\mathrm{d}k_x}{2\pi} v_x(k_x)(1 - R_n(E))[f_L(E) - f_R(E)]. \qquad (2.52)
\end{aligned}$$

By satisfying the unitary conditions that $\hat{s}^\dagger \hat{s} = \hat{1}$ we can prove that $1 - R_n = \sum_M |t_{mn}|^2 = (\hat{t}^\dagger \hat{t})_n n$ such that

$$I = \frac{2_s e}{2\pi} \int_0^\infty \mathrm{d}E \ \mathrm{Tr}\left[\hat{t}^\dagger \hat{t}\right] [f_L(E) - f_R(E)]. \qquad (2.53)$$

We can therefore conclude that the transmission eigenvalues depend on energy. However, if the applied voltage is much smaller than the energy then they are evaluated at the Fermi surface and we can describe the conductance as

$$G = G_Q \sum_p T_p(\mu) \qquad (2.54)$$

where T_p is the transmission eigenvalues. Equation 2.54 describes the two terminal Landauer formula.

Part II

Electrostatic model

Chapter 3

Modelling the patterned 2DEG

We have shown in the previous section that the motion of the electron has been restricted to two-dimensions through the form of the 2DEG within the AlGaAs/GaAs heterostructure. In this chapter, we study how we can restrict this motion further by using fabrication techniques to form edge-channels for injected hot-electrons to travel along. This is done through manipulation of the potential energy at the depth where the hot-electrons reside (the depth of the 2DEG). Our aim is to model how these fabrication techniques will manipulate the electrostatic potential within the heterostructure and thus the potential energy felt by the electrons in the 2DEG.

We will study two fabrication techniques which have been used in HEQO devices: wet chemical etching, and application of Ti/Au gates with applied DC voltages. We will look in detail, separately, how each technique plays a role in shaping the electrostatic potential using modelling techniques. For etching, we review a paper by Davies [47] which uses a particular integral and complimentary function, splitting the electrostatic potential into a sum of two differing potentials; one a solution to Poisson's equation and one a solution to Laplace's equation. We use this to calculate boundary conditions on the surface of the etched heterostructure for two different cases depending on the depth of etching. It is here we find that in order to understand the confinement of the electrons, due to the electrostatic potential, it is the solution to Laplace's equation which we wish to calculate. Using the well known finite element method we present and discuss the resultant electrostatic potential for a simple model.

We then continue, studying the effect of Ti/Au surface gates applied to the surface of the heterostructure with an applied negative biases. The effect the gate has on the surface changes the boundary conditions and we show using the finite element method this change. We expand on our calculations of surface gates by discussing the method

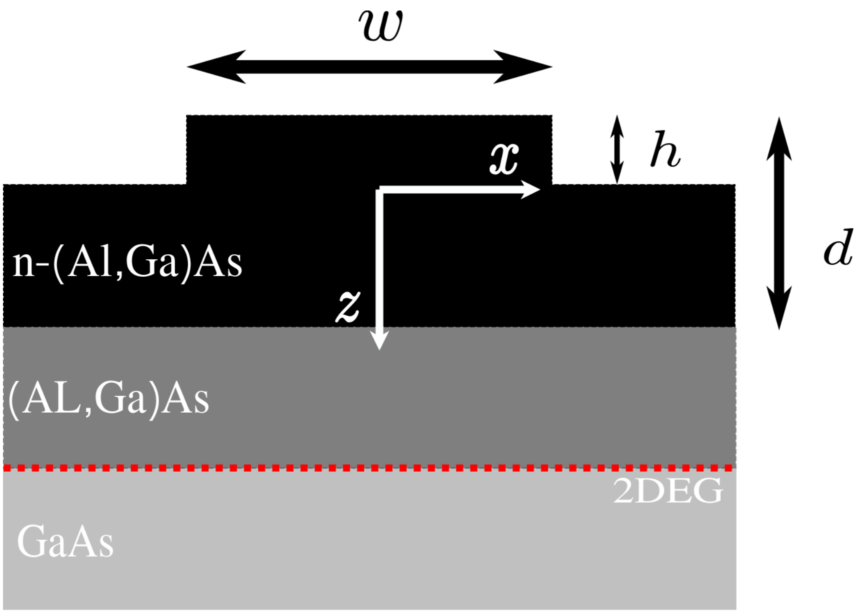

Figure 3.1: A cross-section of a shallow etched AlGaAs/GaAs heterostructure used by Davies [47] to calculate the boundary conditions for ϕ to satisfy Poisson's equation. An etch is made to a depth which does not go past the bottom of the n-doped AlGaAs layer. The depth of etching is labelled as h and the depth of the n-doped AlGaAs layer is labelled as d. An arbitrary width of the etched mesa is given as w.

laid out by a second paper by Davies [32] which allows us to obtain an exact solution for the electrostatic potential at the depth of the 2DEG using a closed form equation. We compare and discuss the two methods for modelling a surface gate with a simple model.

As the size of HEQO devices are of the order of microns, the surface volume ratio is extremely large. As such, the effect of any alteration made on the surface is exaggerated within the volume of the heterostructure. The two approaches used to model of the etching and application of surface gates offer solutions to two very different problems but obtaining the same result. Our goal in this chapter is to take the advantages from both methods and build upon them to be used on HEQO devices where both etching and surface gates are used.

3.1 Etching

The source of electric field within the heterostructure is dispersed from the n-doped layer of AlGaAs, which has a specific number density of electrons, N_D. By patterning the structure of this layer one can manipulate the electrostatic potential at the depth of the 2DEG. By etching into the heterostructure, changing the depth of the n-doped AlGaAs layer, the electric field will not be uniformly dispersed throughout. This will result in a variation of the electrostatic potential which in turn varies the potential energy, creating edge-channels where hot-electrons can travel.

There are two main types of etching that can be performed to acquire such confinements: a deep etch, which etches down past the interface of the undoped spacer AlGaAs layer and GaAs foundation layer where the 2DEG resides, and a shallow etch, which does not pass through the 2DEG. Each technique has its own advantages, however as the experimental devices we consider in this thesis uses a shallow etched wire we shall focus our study on this method. A shallow etch has two main advantages over other models when developing experimental devices. First, the mobility of the electrons is maintained due to the shallowness of the etch. Secondly, it allows for the smallest possible devices to be made as it reduces the risk of damage to the heterostructure (especially over a deep etching which will reduce structural integrity). These advantages are ideal for future development of this HEQO devices.

3.1.1 Boundary conditions

For the electrostatic model we follow the method of Davies [47]. Here he sets out the aim of estimating the electronic properties of (quantum) wires at threshold. This is acceptable for the use of modelling HEQO devices as it it assumes that there are so few electrons present in the channels that it is no longer necessary for the solution to be self-consistent. This is ideal for the purpose of HEQO devices as we assume that the hot-electron is energetically and spatially separated from background electrons. Thus, an injected hot-electron can be regarded as moving in purely external potential and as such can be found by electrostatic modelling. It should be noted that for real devices there may be surface states resulting from surface electrons, oxidation or both, which would lead to more complicated boundary conditions and could also be a potential source of decoherence. For the purposes of this thesis, their effects are ignored, as their presence may create non-uniform and varied magnitudes of potentials felt by the electrons.

Figure 3.1 shows the xz-plane cross section of a shallow etched heterostructure presented by Davies. To explain the calculation of the boundary conditions of the surface of an etched heterostructure, we will use this model to outline the general method. Here, an etched mesa is created by etching away certain region. For the purposes of future calculations, we denote the surface of the exposed etched surface to be at $z = 0$ and the positive z direction going into the heterostructure. For symmetry we also denote $x = 0$ at the centre of the model.

To begin, we look to calculate the boundary condition of a simple model of a shallow etched wire shown in Fig. 3.1. With these boundary conditions, the electrostatic potential can be calculated at the depth of the 2DEG within the structure. We define the electrostatic potential as φ, which is subjected to the boundary condition that it vanishes on the surface and that $\partial\varphi/\partial z \to 0$ as $z \to \infty$. We assume that the potential experienced by the 2DEG is determined solely by the patterning of the heterostructure surface (etching or surface gates) and donor ions (which are assumed to be uniformly distributed in the doped layer).

Davies's approach uses the method of 'particular integral and complementary function' where the potential becomes the sum of two potentials such that $\varphi = \varphi_1 + \varphi_2$. Because of this splitting, we can assign one of the potentials to be a solution to the inhomogeneous equation of the electrostatic potential while the other is the solution to the corresponding homogenous equation. Thus, φ_1 is assigned to be the solution to Poisson's equation

$$\nabla^2 \varphi_1 = -\frac{\rho}{\varepsilon\varepsilon_0} \tag{3.1}$$

but is not required to satisfy all the boundary conditions. Here, we define ρ as the charge density which is homogeneous in the $x - y$ cross section we observe in our model we are studying. We also define ε as the permittivity of the material (which is given the value of 13 for the GaAs heterostructure), and ε_0 as the permittivity of free space. Then, φ_2 is given as the solution of Laplace's equation

$$\nabla^2 \varphi_2 = 0 \tag{3.2}$$

such that the sum of the two $\varphi = \varphi_1 + \varphi_2$ satisfies all the boundary conditions.

Looking at the solution of Poisson's equation first we can see that its dependence on the charge density ρ means that the concentration of donors in the layers of the heterostructure will affect it. As φ_1 is a function of z we find that in the region of the doped layer, the solution is parabolic while in the undoped region it is constant. Assuming the boundary conditions that at $z = 0$ the potential vanishes and as $z \to \infty$ the derivative of the potential vanishes, we find the solutions to be:

$$\varphi_1(x, z) = -\frac{eN_D}{\varepsilon\varepsilon_0}\left[\frac{1}{2}z^2 - (d - h)z\right] \tag{3.3}$$

in the doped region and

$$\varphi_1(x, z) = -\frac{eN_D}{\varepsilon\varepsilon_0}\frac{1}{2}(d - h)^2 \equiv \mathit{\Phi}_1 \tag{3.4}$$

in the undoped region. As we have assumed that in the undoped region the potential is constant where the electrons are found, φ_1 shows no information about how the electrons are confined. As it is not a requirement for φ_1 to satisfy all the boundary conditions, in order for the potential φ to be a full solution of Poisson's equation, φ_2 must be made to obey the boundary condition for all parts of our model found at $z \leq 0$. Thus the potential well, which we are most interested in as it provides edge-channels for the electrons to travel along, is found entirely by φ_2.

For clarity, we refer to the top of the etched rib as the etched mesa, the sidewalls of the etched rib as the exposed sidewalls, and the surface of the etched regions as the exposed etched surface. When calculating φ_2 we must obey the condition that $\varphi = \varphi_1 + \varphi_2$. As such, we find that $\varphi_2 = -\varphi_1$ as $\varphi = 0$ on the surface. The boundary condition of the etched mesa is constant and given as:

$$\varphi_2 = \frac{eN_D}{\varepsilon\varepsilon_0} h(d - \frac{1}{2}h) \equiv \Phi_0. \tag{3.5}$$

For the sidewalls, they are dependent on z as the potential decreases as it reaches the exposed etched surface. It is the same as Equation 3.3 but positive:

$$\varphi_2 = \frac{eN_D}{\varepsilon\varepsilon_0} \Big[\frac{1}{2}z^2 - (d-h)z\Big], \tag{3.6}$$

which means it is also parabolic. Finally we find the boundary condition for the exposed etched surface to be:

$$\varphi_2 = 0, \tag{3.7}$$

which is obeyed by φ_1. As well as satisfying these boundary conditions the derivative of φ_2 must vanish for large z.

3.2 Shallow etched wire

We now want to look at shallow etched wires which will be used by the HEQO devices under our study. From a numerical calculation point of view we need to consider two cases: an etching that does not pass the bottom of the n-doped AlGaAs layer, or an etching that passes this layer and goes further into the undoped spacer AlGaAs layer. Using the method of Davies [47] we will calculate the boundary conditions for both cases and compare their differences. We begin by deriving the solution to Poisson's equation, φ_1, and the subsequent solutions to Laplace's equation, φ_2, for both cases. First, we define the dimensions of the layers of our heterostructure as follows: c as the cap layer of GaAs,

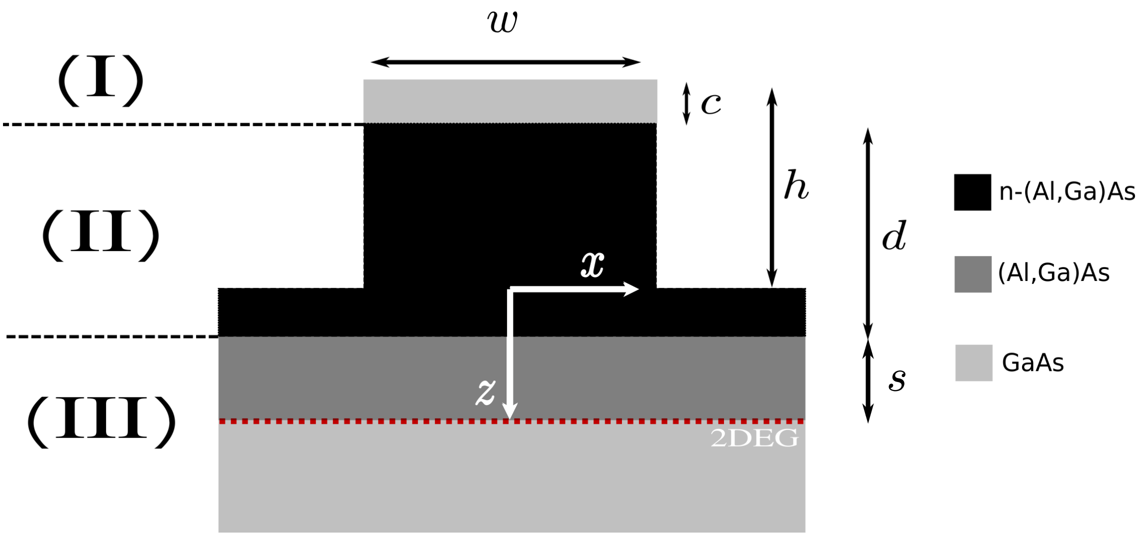

Figure 3.2: Shallow etched wire with a rib of width w with etch no deeper than doping. The depth of the layers are given as c for the cap layer of GaAs, d for the n-doped AlGaAs layer, and s for the undoped AlGaAs layer. The depth of the etching is given as h and the 2DEG can be found at $c + d + s$. This model is split into three regions: region (I) for the cap layer, region(II) for the n-doped AlGaAs layer, and region (III) for the rest of the structure. Region(III) contains the 2DEG. In this model $z = 0$ nm is found at the exposed etched surface and $x = 0$ nm at the centre of the etched rib.

d as the n-doped AlGaAs layer, and s as the spacer layer of undoped AlGaAs. The 2DEG is found at $c+d+s$ and the foundation of the structure below it is a large layer of GaAs, usually 1000 nm deep. However, for our initial modelling we take all edges of the bulk of the heterostructure to be an infinite distance away. The etching depth must remain shallow and so there are two cases we will study: etching not reaching the bottom of the n-doped AlGaAs layer, i.e. $h < d+c$, and etching that goes into the AlGaAs spacer layer, i.e. $d+c < h < d+c+s$.

Case 1: Etch no deeper than doping

This case is represented in Figure 3.2 which shows an etching that does not go past the doped layer of AlGaAs. This is similar to Davies' model in Fig. 3.1 but with a cap layer of undoped GaAs on the top of the etched rib's surface.

Using the dimensions given in Figure 3.2 we first separate the structure into three regions (I), (II), and (III). Region (I) contains the undoped cap layer of GaAs, region (II) contains the n-doped (Al,Ga)As layer while region (III) contains the rest of the structure where the two-dimensional electron gas (2DEG) resides. Then, the solution to φ_1 in its general form is:

i) Region (I)

$$\varphi_1^{(I)} = Az + B \qquad z < (c - h) \tag{3.8}$$

ii) Region (II)

$$\varphi_1^{(II)} = Cz^2 + Dz + E \qquad (c - h) < z < [(d + c) - h] \tag{3.9}$$

iii) Region (III)

$$\varphi_1^{(III)} = Fz + G \qquad z > [(d + c) - h] \tag{3.10}$$

Region (II)

First we look at region (II). Here $\varphi_1^{(II)}$ must satisfy Poisson's equation such that $\nabla^2 \varphi_1^{(II)} = -\frac{eN_D}{\varepsilon\varepsilon_0}$. This reduces to:

$$C = -\frac{eN_D}{\varepsilon\varepsilon_0}\frac{1}{2}. \tag{3.11}$$

We also know that within this region when $z = 0$ the electrostatic potential must vanish to satisfy the boundary condition (BC) on the surface of the semiconductor. Therefore we find that:

$$E = 0. \tag{3.12}$$

Interface(II)/(III)

Next we look at the boundary between region (II) and region(III) found at $z = [(d + c) - h]$. First we note that as $z \to \infty$ then $\varphi_1^{(III)} \to 0$. Thus we can immediately state that

$$F = 0. \tag{3.13}$$

We also want to model the electric field and the electrostatic potential as being continuous at the boundaries between each region. This implies:

$$\begin{aligned} \frac{\partial \varphi_1^{(II)}}{\partial z} &= \frac{\partial \varphi_1^{(III)}}{\partial z} \\ 2Cz + D &= 0 \\ \Rightarrow D &= \frac{eN_D}{\varepsilon\varepsilon_0}[(d + c) - h] \end{aligned} \tag{3.14}$$

and that

$$\begin{aligned} \varphi_1^{(II)} &= \varphi_1^{(III)} \\ Cz^2 + Dz &= G \\ \Rightarrow G &= \frac{eN_D}{\varepsilon\varepsilon_0}\frac{1}{2}[(d+c)-h]^2 \end{aligned} \tag{3.15}$$

Region (I)/(II)

Finally we look at the interface between region (I) and region (II) found at $z = (c-h)$ to find the variables within the region containing the cap layer of undoped GaAs. Again we want to model the electric field as being continuous across these regions:

$$\begin{aligned} \frac{\partial\varphi_1^{(I)}}{\partial z} &= \frac{\partial\varphi_1^{(II)}}{\partial z} \\ A &= 2Cz + D \\ \Rightarrow A &= \frac{eN_D}{\varepsilon\varepsilon_0}d \end{aligned} \tag{3.16}$$

as well as the potential

$$\begin{aligned} \varphi_1^{(I)} &= \varphi_1^{(II)} \\ Az + B &= Cz^2 + Bz \\ B &= Cz^2 + Bz - Az \\ \Rightarrow B &= \frac{eN_D}{\varepsilon\varepsilon_0}\frac{1}{2}(c-h)^2 \end{aligned} \tag{3.17}$$

Final solution

i) Region (I) where $z < (c-h)$:

$$\varphi_1^{(I)} = \frac{eN_D}{\varepsilon\varepsilon_0}[dz + \frac{1}{2}(c-h)^2] \tag{3.18}$$

ii) Region (II) where $(c-h) < z < [(d+c)-h]$:

$$\varphi_1^{(II)} = -\frac{eN_D}{\varepsilon\varepsilon_0}\{\frac{1}{2}z^2 - [(d+c)-h]z\} \tag{3.19}$$

iii) Region (III) where $z > [(d+c)-h]$:

$$\varphi_1^{(III)} = \frac{eN_D}{\varepsilon\varepsilon_0}\frac{1}{2}[(d+c)-h]^2 \tag{3.20}$$

and for φ_2 on each boundary we get:

i) The top of the etched rib ($|x| < w/2$, $z = -h$):

$$\varphi_2 = -\varphi_1^{(I)}(z = -h) = -\frac{eN_D}{\varepsilon\varepsilon_0}\{-dh + \frac{1}{2}(c-h)^2\} \tag{3.21}$$

ii) The sidewalls of the cap layer ($x = \pm w/2$, $-h < z < (c-h)$):

$$\varphi_2 = -\varphi_1^{(I)}(z) = -\frac{eN_D}{\varepsilon\varepsilon_0}[dz + \frac{1}{2}(c-h)^2] \tag{3.22}$$

iii) The sidewalls of the n-doped AlGaAs layer ($x \pm w/2$, $-h + c < z < [(c+d) - h]$)

$$\varphi_2 = \varphi_1^{(II)}(z) = \frac{eN_D}{\varepsilon\varepsilon_0}\{\frac{1}{2}z^2 - [(d+c) - h]z\} \tag{3.23}$$

iv) The remaining surfaces:

$$\varphi_2 = 0 \tag{3.24}$$

The last BC comes from the requirement that at $z = 0$ the potential goes to zero. As mentioned previously, this is a complex structure and only approximate solutions can be made analytically.

Case 2: etch deeper than doping

We now look at the model where $d + c < h$ as shown in Figure 3.3. As before we give general solutions to each region:

i) Region (I)

$$\varphi_1^{(I)} = Az + B \qquad z < (c-h) \tag{3.25}$$

ii) Region (II)

$$\varphi_1^{(II)} = Cz^2 + Dz + E \qquad (c-h) < z < [(d+c) - h] \tag{3.26}$$

iii) Region (III)

$$\varphi_1^{(III)} = Fz + G \qquad z > [(d+c) - h] \tag{3.27}$$

As before we can solve Poisson's equation in region (II) such that:

$$C = -\frac{eN_D}{\varepsilon\varepsilon_0}\frac{1}{2} \tag{3.28}$$

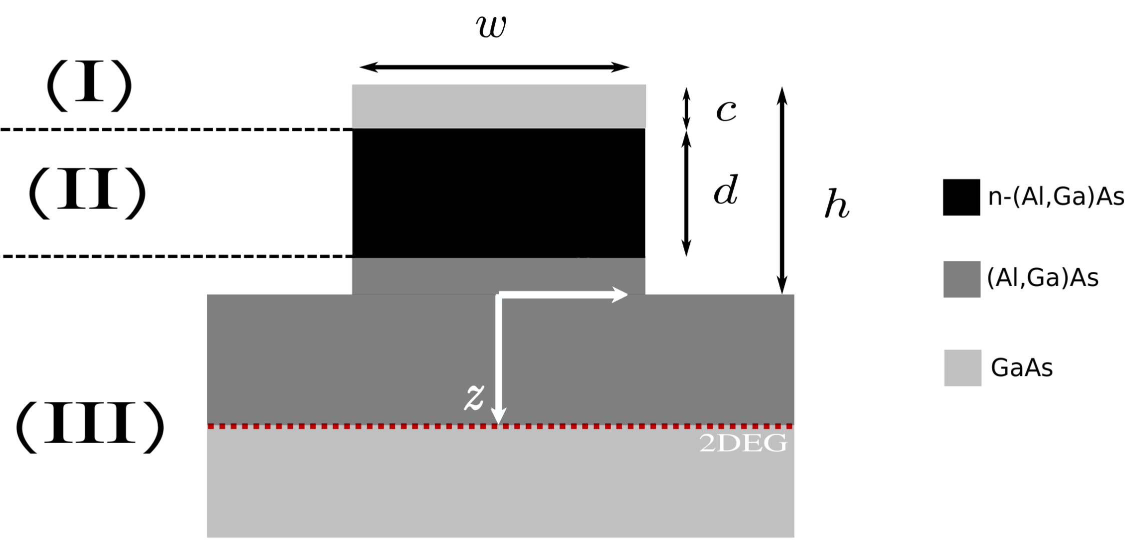

Figure 3.3: A model of a shallow etched wire with an etch deeper than doping. The same labels for the depths of layers and separation of regions as Figure 3.2 but now the etching goes past the n-doped layer of AlGaAs.

In region (III) lies the undoped (Al,Ga)As layer where the boundary condition of $\varphi_1(z=0)=0$. Then from Equation 3.27 we get:

$$G = 0. \tag{3.29}$$

The equation should also satisfy the condition that the electrostatic potential vanishes as $z \to \infty$

$$\Rightarrow F = 0 \tag{3.30}$$

Interface (II)/(III)

As the boundaries are continuous we get the two general equations that are true at the depth $z = [(d+c)-h]$:

$$Cz^2 + Dz + E = 0 \tag{3.31}$$

$$2Cz + D = 0 \tag{3.32}$$

From Equation 3.32 we deduce D:

$$D = \frac{eN_D}{\varepsilon\varepsilon_0}[(d+c)-h] \tag{3.33}$$

and then we find E:

$$\begin{aligned} E &= -Cz^2 - Dz \\ &= \frac{eN_D}{\varepsilon\varepsilon_0}\frac{1}{2}[(d+c)-h]^2 - \frac{eN_D}{\varepsilon\varepsilon_0}[(d+c)-h]^2 \\ &= -\frac{eN_D}{\varepsilon\varepsilon_0}\frac{1}{2}[(d+c)-h]^2 \end{aligned} \tag{3.34}$$

Interface (I)/(II)

From continuous boundaries at $z = (c-h)$ we find:

$$Cz^2 + Dz + E = Az + B \tag{3.35}$$

$$2Cz + D = A \tag{3.36}$$

where A is simple to solve:

$$\begin{aligned} A &= -\frac{eN_D}{\varepsilon\varepsilon_0}(c-h) + \frac{eN_D}{\varepsilon\varepsilon_0}[(d+c)-h] \\ &= \frac{eN_D}{\varepsilon\varepsilon_0}d \end{aligned} \tag{3.37}$$

and therefore we can rearrange Equation 3.35 to find B:

$$\begin{aligned} B &= Cz^2 + Dz + E - Az \\ &= -\frac{eN_D}{\varepsilon\varepsilon_0}(c-h)^2 + \frac{eN_D}{\varepsilon\varepsilon_0}[(d+c)-h](c-h) \\ &\quad - \frac{eN_D}{\varepsilon\varepsilon_0}[(d+c)-h]^2 - \frac{eN_D}{\varepsilon\varepsilon_0}d(c-h) \end{aligned} \tag{3.38}$$

Final solution

i) Region (I) where $z < (c-h)$:

$$\varphi_1^{(I)} = \frac{eN_D}{\varepsilon\varepsilon_0}[dz + \frac{1}{2}(c-h)^2 - ((d+c)-h)^2] \tag{3.39}$$

ii) Region (II) where $(c-h) < z < [(d+c)-h]$:

$$\varphi_1^{(II)} = -\frac{eN_D}{\varepsilon\varepsilon_0}\{\frac{1}{2}z^2 - [(d+c)-h]z + [(d-c)-h]^2\} \tag{3.40}$$

iii) Region (III) where $z > [(d+c)-h]$:

$$\varphi_1^{(III)} = 0 \tag{3.41}$$

An important aspect of this calculation is the solution in region (III) where the 2DEG resides. For this model there is no additional potential at the 2DEG as $\varphi_1^{(III)} = 0$. By applying the dimensions $c + d = h$ implies $[(d + c) - h] = 0$ would reduce these solutions to be identical to the previous case of $h < (d + c)$.

We then calculate the boundary conditions for φ_2 on each boundary as:

i) The top of the etched rib ($|x| < w/2$, $z = -h$):

$$\varphi_2(z = -h) = -\frac{eN_D}{\varepsilon_r\varepsilon_0}\{-dh + \frac{1}{2}(c - h)^2 - [(d + c) - h]^2\} \tag{3.42}$$

ii) The sidewalls of the cap layer ($x = \pm w/2$, $-h < z < -h + c$):

$$\varphi_2 = -\frac{eN_D}{\varepsilon\varepsilon_0}[dz + \frac{1}{2}(c - h)^2] \tag{3.43}$$

iii) The sidewalls of the n-doped AlGaAs layer ($x \pm w/2$, $-h + c < z < -h + (c + d)$)

$$\varphi_2 = -\frac{eN_D}{\varepsilon_r\varepsilon_0}\{\frac{1}{2}z^2 - [(d + c) - h]z + [(d - c) - h]^2\} \tag{3.44}$$

iv) The remaining surfaces including the sidewall of the undoped AlGaAs layer:

$$\varphi_2 = 0 \tag{3.45}$$

These values are then set as the Dirchlet Boundary conditions that the solution φ_2 must satisfy at those boundaries.

3.3 Modelling the surface

Clearly the behaviour of the exposed surface is crucial when modelling the electrostatic potential at the 2DEG due to alterations to the surface, which is emphasised by previous work [58]. Here we show two ways of modelling the 2DEG response to changes on the surface of our model:

1. **Pinned surface** - Usually, when modelling experimental devices using a III-V heterostructure at room temperature, the Fermi energy E_f is pinned at a fixed energy below the conduction band on the exposed etched mesa of the structure. Without a surface gate with an applied voltage, the Fermi energy is in equilibrium throughout. However, when there is a change which affects the electrostatic potential at the the

surface there is uncertainty of whether the Fermi energy is pinned to the 2DEG or to the altered surface. The latter poses a clear problem; the difference between the band gap and the altered surface would be zero from within the material and edge-states could not be formed and hence no channels for electrons to travel along. It is then assumed that E_f is pinned to the 2DEG and as such the exposed surface would behave as an equipotential at zero. This is an ideal boundary conditions that offers simplicity to problem of modelling the electrostatic devices.

2. **Frozen surface** - The pinned surface offers simplicity to an increasingly complex problem. However, it is mostly used for experimental models conducted at room temperature. At cryogenic temperatures the frozen surface boundary condition is supposed to be used, although increasing the difficulty of treating the problem analytically. A mixed boundary condition is imposed on the potential at the surface such that the derivative is specified on the etched mesa but not in the region occupied by the altered surface. At equilibrium, where there would be zero change, the common potential between the surface and the 2DEG is zero. When the altered surface does have an effect on the electrostatic potential, changes can be superposed on this state with the exposed unaltered surface remaining fixed. The complexity of the geometry of altering the surface (through etching or application of surface gates which we discuss later on) must be taken into account as it should be used for much simpler designs.

Although the HEQO devices we will study are performed in a refrigerator at cryogenic temperatures, we elect to use the pinned surface. This boundary condition has been used before on similar models of devices [59, 60]. We will show later on how the use of this boundary condition when comparing theoretical results from our models with experimental results gives a good approximation.

3.4 Finite element method

In the previous two sections we outlined the method for calculating the boundary conditions for a heterostructure which has been etched to form a shallow etched wire. We now look to calculate how these boundary conditions disperse through our model in order to study the electrostatic potential, φ_2, which confines the electrons at the 2DEG. Here we introduce the finite element method (FEM), which requires numerical computation and for the calculations we present, we have used MATLAB [61] which has included a Partial Differential Toolbox. This programme uses the FEM for bounded domains of 2-D or 3-D space [62, 63]. Although our model here is two-dimensional and quite simple, we will later expand on future models complexity, involving etching and surface gates. This is an ideal method due to its ability to describe a complicated geometry as a system of subdomains. Ideally, the size of the meshing can be changed depending on intricacy of the structure. This greatly reduces the original PDE of one large domain into smaller, less costly subdomains of simpler equations.

A general PDE is given in the form of:

$$-\nabla \cdot (c\nabla u) + au = f \tag{3.46}$$

considered in the domain Ω and u is the solution we want to find. For a full proof we will suppose the equation is subject to Dirichlet and Neumann boundary conditions in the $\partial\Omega_D$ and $\partial\Omega_N$ domains respectively. The difference between the two is that when Dirchlet boundary conditions are imposed on a PDE, the solution must take those exact value at the boundary. In the case of Neumann boundary conditions, the boundaries must have the values of the derivative of the solution.

The PDE is is currently in a form which has second order spatial derivatives and is very general (strong form). To simplify this we put it into an integral form (weak form) by applying a test function and integrating over a domain Ω such that

$$\int_\Omega (-\nabla \cdot (c\nabla u) + au - f)v d\Omega = 0 \tag{3.47}$$

where v is the test function. Green's formula is used to integrate by parts creating terms in the second-order:

$$\int_\Omega (c\nabla u \nabla v + auv)d\Omega - \int_{\Omega_N} \vec{n} \cdot (c\nabla u)d(\partial\Omega_N) + \int_{\Omega_D} \vec{n} \cdot (c\nabla u)d(\partial\Omega_D) = \int_\Omega fvd(\partial\Omega). \tag{3.48}$$

As we want boundary conditions to be set to exact values we can ignore the domain with the Neumann BC (second term). The meshing is then layered over the structure we are calculating for, discretising the the domain into subdomains or elements Ω^e. In other words, we are projecting the weak form of the PDE onto a finite-dimensional subspace i.e. a subdomain which can formed due to meshing. Using the notation u_h and v_h as the equivalent functions defined in Ω^e the PDE becomes:

$$\int_{\Omega^e} (c\nabla u_h \nabla v_h + au_h v_h)d\Omega^e + \int_{\Omega^e_D} \vec{n} \cdot (c\nabla u_h)d(\partial\Omega^e_D) = \int_{\Omega^e} fv_h d(\partial\Omega^e) \tag{3.49}$$

being our discretised weak form of the PDE. To express u_h we let Φ_i be the piecewise

Dimensions of Structure		
Variable	Description	Size
c	Cap layer of undoped GaAs	10 nm
d	n-doped layer of AlGaAs	40 nm
s	Undoped layer of AlGaAs	40 nm
h	Total depth of etching	60 nm

Table 3.1: Table of parameters for the depth of each layer found in the heterostructure.

polynomial basis function for the subspaces $i = 1, 2, ..., N_p$. Thus it is a linear combination of these basis functions:

$$u_h = \sum_{1}^{N_p} U_i \Phi_i \tag{3.50}$$

where U_i is an unknown scalar coefficient. This can be substituted into the discretised weak form PDE with the test functions $v_h = \phi_i$ being performed in the integrations. Thus the FEM yields a system of N_p equations in terms of N_p unknowns U_i. To calculate the Laplace equation we apply the coefficients of the PDE as $c = 1$, $a = 0$, and $f = 0$ for the Laplace equation:

$$\nabla^2 u = 0 \tag{3.51}$$

3.4.1 Electrostatic potential

We now have the foundation for building an electrostatic model of a shallow etched wire. With the boundary conditions calculated from Davies we can apply these to the FEM to find the electrostatic potential at the depth of the 2DEG. For our model we use realistic heterostructure parameters which can be found in Table 3.1. For these parameters we find that the the etching goes past the depth of the n-doped AlGaAs layer and as such we will use the boundary conditions outlined in case 2.

The model shown in Fig. 3.2 show the layers of materials which are formed on top of a layer of GaAs 1000 nm thick. As the etch goes no deeper than the doping, we find the solution to Poisson's equation in the region of the 2DEG using Eq. (3.41) that $\varphi_1^{(III)} = 0$. Then, the full details of the potential and the confinement lie in the solution to Laplace's equation. From Eq. (3.42) we calculate the boundary condition of the surface of the etched mesa using the parameters in Table 3.1 and for a number density of charge particles $N_D = 8 \times 10^{17}\,\mathrm{cm}^{-3}$ giving a value of $\Phi_0 = 1.392\,\mathrm{V}$ uniformly spread across the etched mesa. The sidewalls of the GaAs cap layer follow the boundary condition of Eq. (3.43), linearly dependent on z. The exposed sidewalls of the etched doped layer follow Eq. (3.44)

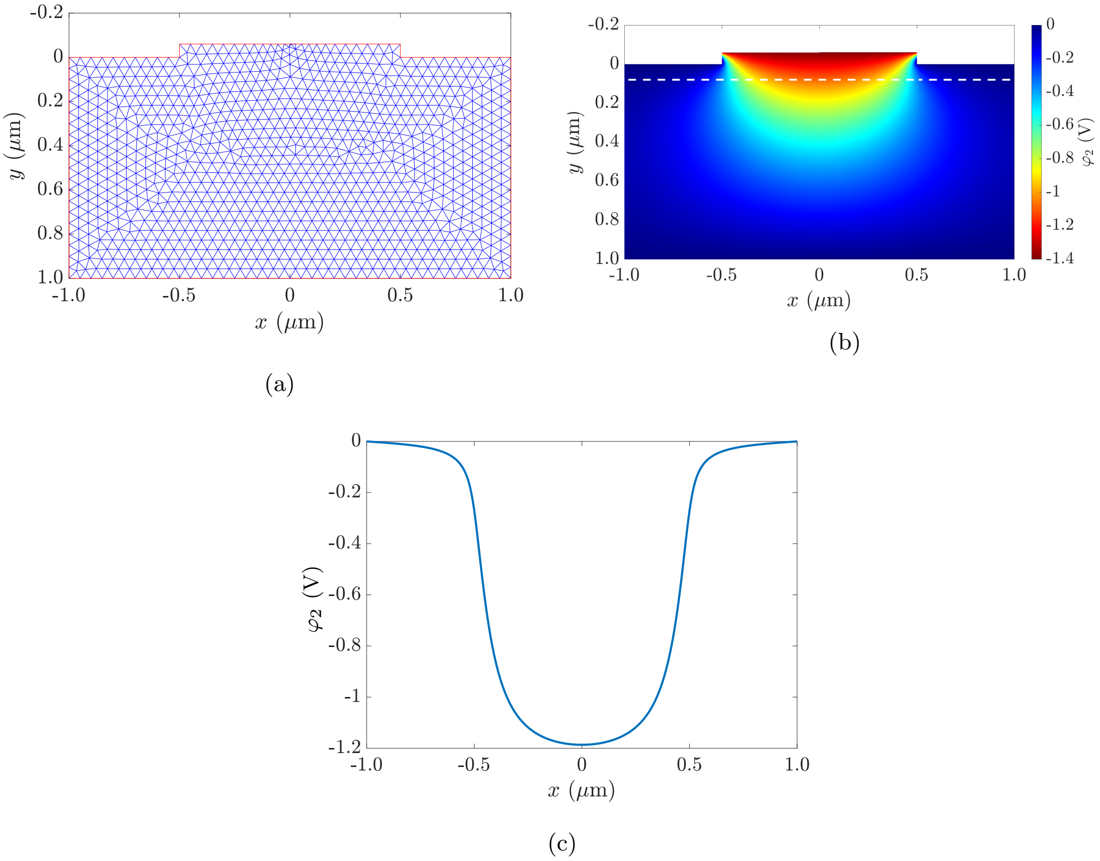

(a)

(b)

(c)

Figure 3.4: (a) Meshing of the shallow etched wire in Fig. 3.3. The domain size is 2 μm × 1 μm and the size of the meshing is limited to a maximum of 50 nm, for visual purposes. An etched mesa of width $w = 1\,\mu$m is centred around $x = 0$ and a depth of $h = 60\,$nm. (b) Electrostatic potential of the model shown in Fig. 3.4a using the FEM based on Fig. 3.3. A dashed, white line represents the position of the 2DEG found within the heterostructure based on the parameters of Table 3.1. (c) Potential energy at the depth of the 2DEG, taken along the x-axis at $y = 30\,$nm (dashed, white line) in Fig. 3.4b.

which is parabolically dependent on z. While the rest of the surface is set to be zero.

Applying these boundary conditions to the FEM we first must create a mesh over our model to create an array of subdomains. Figure 3.4a shows the domain of our model in Fig. 3.2 with a triangulated meshing. The size of the triangles can be varied to adjust the resolution of the calculation. In this case, the meshing is made to be relatively large for visual purposes. However, for the actual calculations we use much smaller meshing. The size of the meshing will vary for our model of the SEW as a constant size of triangles cannot be used to fit fully inside the domain. Here we show a meshing limited to a maximum triangular size of 50 nm (the size refers to the height of the triangle). In particular for this visual meshing in the figure, the exposed sidewalls of the etched rib has an edge of one triangles containing the subdomain calculation which involves the boundary condition of Eq. (3.44) and Eq. (3.43).

Figure 3.4b shows the electrostatic potential φ_2 of the entire model of the shallow etched wire. From this figure we can highlight the differences in the boundary conditions applied to the surfaces. Although the etched mesa has a constant, uniform electrostatic potential, the two boundary conditions on the sidewall have a strong effect on its dispersion into the heterostructure. The slow, linear decrease of φ_2 on the etched sidewall of the capped layer followed by a quicker, parabolic decrease of the exposed n-doped layer shows a shaping that will form the basis of an energy well. This shaping is further exaggerated by the zero boundary conditions on the exposed etched surface. The FEM calculates the Laplace equation for each subdomain created in the triangular meshing. Applying the boundary conditions on the surface of our model, Fig. 3.4b shows how the electrostatic potential φ_2 permeates within the structure.

The etched rib can be seen to provide the source for the electrostatic potential, dispersing out radially. The edges and base of the bulk of the structure is set to Neumann boundary conditions such that they do not affect the electrostatic potential and we keep our assumption of our simplified model that $\varphi \to 0$ as $z, x \to \pm\infty$. The etched sidewalls show a parabolic variation in φ_2, going to zero as it reaches $z = 0$. This variation along the exposed sidewall can be seen to manipulate the electrostatic potential greatly. Directly below the etched rib is where the electrostatic potential remains strongest for each layer in the z direction. The combination of etching and the boundary condition of exposed etched surfaces set to zero explain how the electrostatic potential is dispersed, creating edge states for the hot-electron to travel along only in the area.

Figure. 3.4c shows the electrostatic potential, φ_2, at the depth of the 2DEG. Here the effect of the etching can be clearly seen, creating variations in the electrostatic potential for areas closest the etched region. The result of this creates edge-states in which an injected hot-electron can travel. As we observe regions outside the etched mesa, the electrostatic potential goes to zero. The maximum absolute electrostatic potential at the surface of the etched mesa was calculated to be $\Phi_0 = -1.392\,\mathrm{V}$. At the depth of the 2DEG the maximum absolute electrostatic is found at $x = 0$ with a value $\varphi_2 = 1.187\,\mathrm{V}$. The dispersion of φ_2 through 90 nm of heterostructure has reduced by 15%.

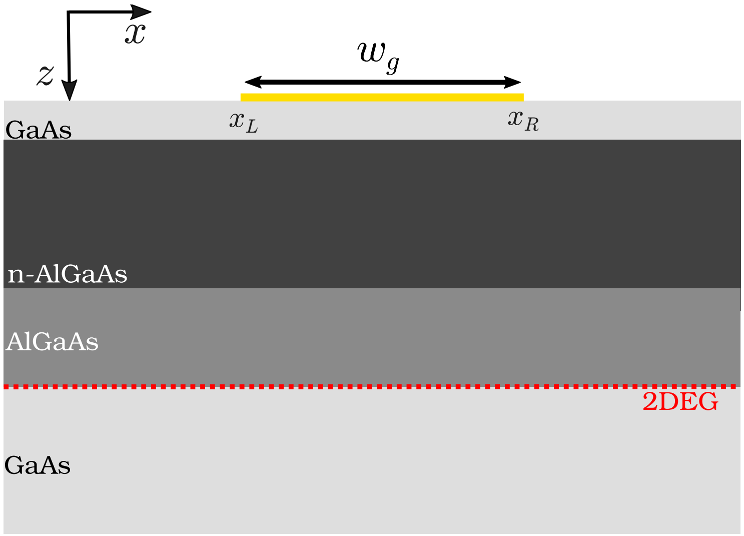

Figure 3.5: A two-dimensional cross-section of the AlGaAs/GaAs heterostructure where the surface is found in x-y plane and z is going into the structure. The surface is covered by a Ti/Au gate (shown in gold) with x_L and x_R denoting the x coordinate of the left and right edge of the surface gate respectively.

3.5 Surface gates

The use of etching is one way of manipulating the motion of electrons. A second technique that is used when fabricating HEQO devices is the use of Ti/Au gates laid on the surface of the heterostructure with an applied voltage. In the same way as the etching, a negative DC voltage applied to the surface can change the electrostatic potential throughout the heterostructure and affect the 2DEG within. They have been used to produce devices such as quantum wires [64], quantum point contacts [65], and quantum dots [66]. We approach the modelling of this fabrication technique by studying a model shown in Fig. 3.5, which shows an AlGaAs heterostructure with a surface gate (gold) of width w_g in the region between the x coordinate points x_L and x_R.

Although we could apply the FEM for this model, taking into account the boundary conditions that the surface imposes, we take a new approach by reviewing the use of an analytical approach formulated by a second paper by Davies [32] and has been employed to model a variety of devices [65, 67, 68]. Here, Davies identified a few challenges that make the modelling of these surface gate patterned devices difficult:

1. Complicated geometry. The complexity of the surface gate structures has not simplified over the last 50 years where gates can be as small as 100 nm with the 2DEG only a depth of 50 nm from the surface. Due to this, the modelling must take into account the three-dimensional geometry of the device.

2. Self-consistency with the electrostatic potential is a difficult numerical task. The dimensions of the region occupied by the electrons are comparable with their wavelength and so a quantum mechanical treatment of the electrons may be needed. This is especially import with the modelling of a quantum dot.
3. The small size of these devices (on the scale of microns) means that the surface has a large influence on the inside where the 2DEG resides, exaggerating the effects of electric fields.

The first and third challenge hasn't changed over time and we will see in the rest of the chapter how it can become more complicated with the addition of etching. The second problem, with regards to hot-electrons, is not something that we take into consideration. As explained before, the hot-electron is thought to be isolated from background electrons energetically, from the high emitted energy of the electron, and spatially where we inject the hot-electrons into regions where the 2DEG is depleted. Therefore, self-consistent calculation would be negligible and so these calculations are not required for the modelling of HEQO devices within the scope of this thesis. Self-consistency can be included in these calculations [69, 70] were we to model devices where the depleted 2DEG wasn't as great or the emitted energy of the hot-electron wasn't as high. It is clear that self-consistency would improve the calculation of the boundary conditions, however, for the purposes of this thesis we continue with the assumptions we have made above to highlight the uniqueness of the hot-electrons we are studying and with the motivation that we are looking for a simple method to calculate the potential of complex devices.

Another challenge with modelling surface gates is that a metallic gate introduces a work function and can lead to screening effects, which can reduce the effect of the doped layer. This screening effect would likely lead to a change in the number density of charged particles, N_D. Experimentally, we know the density of impurities but we cannot be sure about whether all of them are ionising. As we are trying to model heterostructures with complicated geometries, we keep things simple by assuming that the density of impurities are fully ionised and we do not take into account screening effect from the metallic surface gates. Although, if we were to take this effect into account, it would mean that the our calculated value of Φ_0 is reduced. We will discuss in the next chapter what this effect can mean for our calculations.

Davies looks to calculate the electrostatic potential in a plane at a depth d below the surface of a heterostructure where a surface gate occupies some region. As for the previous models and all subsequent models of this thesis, the surface occupies the x-y plane and z is measured into the heterostructure.

Davies [32] derives an equation for the potential due to a surface gate in an AlGaAs/GaAs heterostructure. The problem here, as with the FEM, is to find a solution to Laplace's equation $\nabla\varphi_2^2 = 0$ subject to the boundary conditions of $\varphi_2(\mathbf{r}, 0)$ on the plane and that $\varphi_2 \to 0$ as $z \to \infty$. Davies begins by making a 2D Fourier transform on the surface boundary condition $\varphi_2(\mathbf{r}, 0)$ to $\tilde{\varphi_2}(\mathbf{q}, 0)$ where the dependence on z becomes a decaying exponential which satisfies the aforementioned boundary condition and Laplace's equation. Hence, the general Fourier transform can be stated as $\tilde{\varphi_2}(\mathbf{q}, z) = \tilde{\varphi_2}(\mathbf{q}, 0)\exp(-|qz|)$, the equivalence of which is a convolution in real space. Performing the inverse Foruier transform leads to a general result given for the surface gate equation:

$$\varphi_2(\mathbf{r}, z) = \int \frac{|z|}{2\pi(z^2 + |\mathbf{r} - \mathbf{r}'|^2)^{3/2}} \varphi_2(\mathbf{r}', 0) d\mathbf{r}' \tag{3.52}$$

where $\mathbf{r} = (x, y)$ is the two-dimensional vector. As we are working in the x and z plane we can integrate this equation to get rid of the y dependence.

$$\begin{aligned} \varphi_2(x, z) &= \int_{-\infty}^{\infty} \left(\int_{-\infty}^{\infty} \frac{|z|}{2\pi(z^2 + (x - x')^2 + y'^2)^{3/2}} dy' \right) \varphi_2(x', 0) dx' \\ &= \frac{z}{2\pi} \int_{-\infty}^{\infty} \left(\left[\frac{y'}{((x - x')^2 + z^2)((x - x')^2 + y'^2 + z^2)^{1/2}} \right]_{-\infty}^{\infty} \right) \varphi_2(x', 0) dx'. \end{aligned} \tag{3.53}$$

By splitting the intervals from $-\infty$ to 1 and 1 to ∞ such that:

$$\begin{aligned} &\left[\frac{y'}{((x - x')^2 + z^2)((x - x')^2 + y'^2 + z^2)^{1/2}} \right]_{-\infty}^{1} \\ &+ \left[\frac{y'}{((x - x')^2 + z^2)((x - x')^2 + y'^2 + z^2)^{1/2}} \right]_{1}^{\infty} \\ &= \frac{2}{(x - x')^2 + z^2} \end{aligned} \tag{3.54}$$

we simplify the solution to the integral on y' and return it back into the integral on x' leaving us with

$$\varphi_2(x, z) = \frac{z}{2\pi} \int_{-\infty}^{\infty} \frac{2}{(x - x')^2 + z^2} \varphi_2(x', 0) dx' \tag{3.55}$$

which is a general solution for the entire length of the x-axis. We will assume that a gate is found from the points $x_L < x < x_R$ which in this region $\varphi_2(x, 0) = V_g$. For all other values of x the potential is zero ($\varphi_2(x,0) = 0$). Solving for these potentials we find:

$$\begin{aligned}\varphi_2(x,z) &= \frac{zV_g}{2\pi}\int_{x_L}^{x_R}\frac{2}{(x-x')^2+z^2}dx' \\ &= \frac{zV_g}{2\pi}\Bigg[-\frac{2}{z}\tan^{-1}\Big(\frac{x-x'}{z}\Big)\Bigg]_{x_L}^{x_R} \\ &= \frac{V_g}{\pi}\Bigg(-\tan^{-1}\Big(\frac{x-x_R}{z}\Big)+\tan^{-1}\Big(\frac{x-x_L}{z}\Big)\Bigg)\end{aligned} \tag{3.56}$$

finally acquiring the potential due to a surface gate with an applied voltage V_g:

$$\varphi_2 = \frac{V_g}{\pi}\Bigg(-\tan^{-1}\Big(\frac{x-x_R}{z}\Big)+\tan^{-1}\Big(\frac{x-x_L}{z}\Big)\Bigg). \tag{3.57}$$

In NPL's heterostructure the 2DEG is found 90 nm from the surface of the etched rib, according to Table 3.1. As preliminary calculation we begin by assuming here a voltage of $V_g = -1$ V is applied to the surface gate, which has a width of $w_g = 1$ μm. Using Eq. (3.57) we can use the analytical approach to solve for the electrostatic potential at the depth of the 2DEG.

An important feature of Davies's surface gate equation is that once the calculation is made for the electrostatic potential, any changes in the value of V_g is can be added to the resultant calculation. As a way of example, we will calculate the electrostatic potential by taking away the values of the boundary conditions on the surface such that the free surface has a boundary condition of $\varphi_2 = 0$ and the surface gate $\varphi_2 = V_g$. This simplifies the calculation to the performance of Eq. (3.57) where $V_g = -1$ V. For comparison we also perform the FEM, applying the same boundary conditions.

For the FEM applied voltage to the surface gate imposes a boundary condition on the surface, spanning from x-coordinate points on the surface. Due to this, and keeping consistency with the pinned surface, the boundary conditions on the top surface are:

$$\varphi_2 = 0 \text{ for } -\infty < x < x_L \ \& \ x_R < x < \infty \tag{3.58}$$

and

$$\varphi_2 = V_g \text{ for } x_L < x < x_R, \tag{3.59}$$

which can be implemented into the FEM numerical calculations.

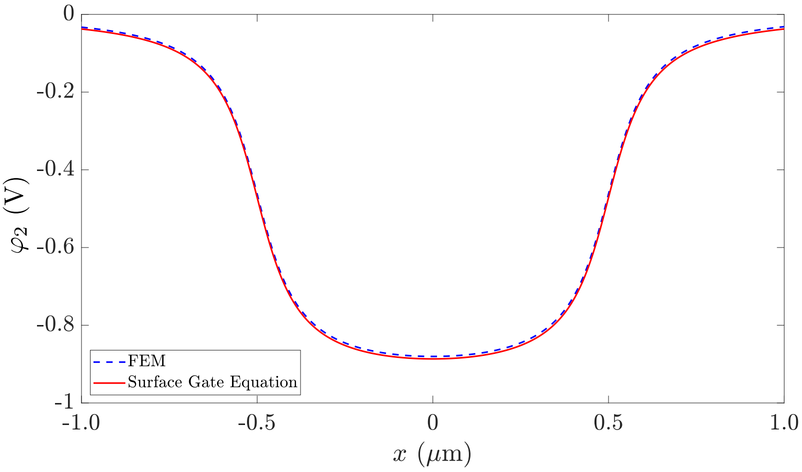

(a)

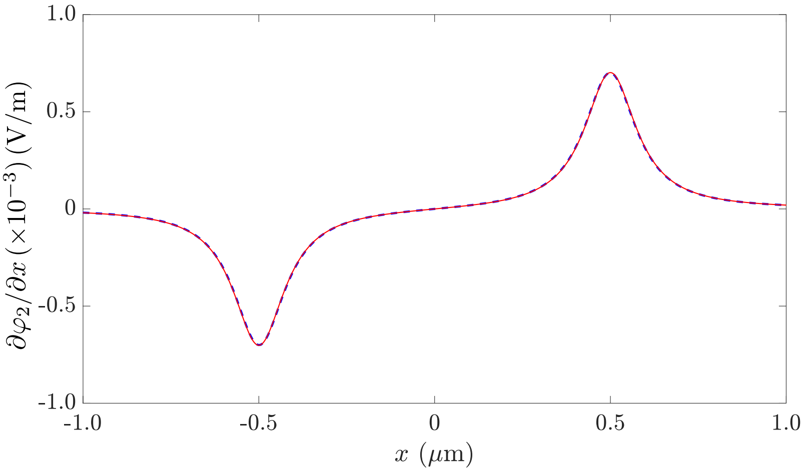

(b)

Figure 3.6: (a) Comparison of the electrostatic potential φ_2 calculated using Davies's surface gate equation (sold, red line) and the FEM (dashed, blue line). A surface gate of width $w_g = 1$ μm was applied to the surface of a AlGaAs/GaAs heterostructure where the 2DEG resides 90 nm below the surface. A gap of 1 μm of exposed free surface was left either side of the surface gate for the FEM calculation. (b) The electric field for each potential given in (a).

Figure.3.6a shows the plot for the electrostatic potential calculated using Eq. (3.57) (solid, blue line) and the FEM (dashed, blue line). Both method show similar results, with Davies' equation have a slightly larger magnitude of φ_2. At the maximum the FEM results in $\varphi_2 = -0.88$ V while for Davie's equation it reaches $\varphi_2 = -0.887$, a difference of approximately 0.8%. In Fig.3.6b we show the gradient of the potentials seen in Fig.3.6a. Although there were slight variations in the value of φ_2, all be it very small, the difference did not affect the gradient, i.e. the dispersion of the electric field $E = \partial\varphi_2/\partial x$. As with the shallow etched wire, we find that the meshing of the FEM creates discrepancies. Both results are exact solutions but using Davies' method, reduced to one-dimension, gives us more accuracy with the number of points calculated with the same computational power as the FEM.

3.6 Chapter summary

In this chapter, we have shown separately two methods used to fabricate HEQO devices from an AlGaAs/GaAs heterostructure. For each technique we have calculate the electrostatic potential which allows us to model how these techniques can be used in confining electrons and construct pathways for injected hot-electrons in order to manipulate them. In particular, we have shown the process of calculating the boundary conditions of an AlGaAs/GaAs heterostructure that has been chemically etched in order to manipulate the motion of electrons injected from single electron sources. By following the method of Davies [47] we have shown that in order to model the electrostatic potential at the depth of the 2DEG we need to solve Laplace's equation to obtain information about the confinement of the electrons. By introducing the FEM, we were able to use these boundary conditions to calculate how the electrostatic potential disperses throughout the device, affecting the 2DEG.

We then studied the technique of applying Ti/Au surface gates with applied biases to the surface of the heterostructure. We expanded on the use of the FEM to calculate the electrostatic potential and introduce Davies equation for modelling a surface gate [32]. This showed to give very good approximations for the electrostatic potential at the depth of the 2DEG when compared to the numerical calculation of the FEM. This is an important step in the process of our modelling. Davies method has allowed us to get accurate results comparable to the FEM but with the opportunity to represent these results analytically. Because of this, a single equation can be used, after inputting the right parameters into the integrals, to obtain an electrostatic potential at the depth of the 2DEG, without the need of fully modelling the entire device in question.

However, HEQO devices, especially the ones that we study, will utilise both techniques at the same time. In this case, consideration of modelling the two separately is not efficient nor practical. In the next chapter we will combine the two works of Davies [47, 32] into one method, with the advantage of being able to calculate an entire HEQO device model in one equation.

Chapter 4

Projected surface method

In the previous chapter we introduced two fabrication techniques used for manipulating electrons within a heterostructure containing a 2DEG. In both cases, the electrostatic potential was altered such that edge-states were created providing channels where injected hot-electrons can travel along. However, the HEQO devices we study in this thesis utilise both etching and applied surface gates and so we look to create a method which will encompass both. To further add complications, the the devices are much more complicated to just model in two-dimension and a full three-dimensional model is required. In such a case, the computational cost of using the FEM will greatly increase with a decrease in accuracy due to the fineness of meshing required for the numerical calculations.

In this chapter we provide a method which utilises both the surface gate equation and calculation of boundary conditions for etched heterostructures laid out by Davies [47]. We call this method the projected surface method.

4.1 Shallow etched wire with a surface gate

The use of surface gates and etching separately can provide channels for hot-electrons to travel in. However, combining the two together proves to be an important feature of HEQO devices. The use of a surface gate applied to the etched rib depletes all the background electrons directly below the gate. In such a case, the hot-electron is not only energetically separated from the 2DEG because of its higher injected energy, but the addition of the surface gate with an applied voltage spatially separates it from bulk electrons.

A simple model of a shallow etched wire with a surface gate is shown in Fig. 4.1. Again, the parameters used follow Table 3.1 where the depth of the etching reaches the bottom layer of the *n*-doped AlGaAs layer. A Ti/Au surface gate (shown in gold) is applied on

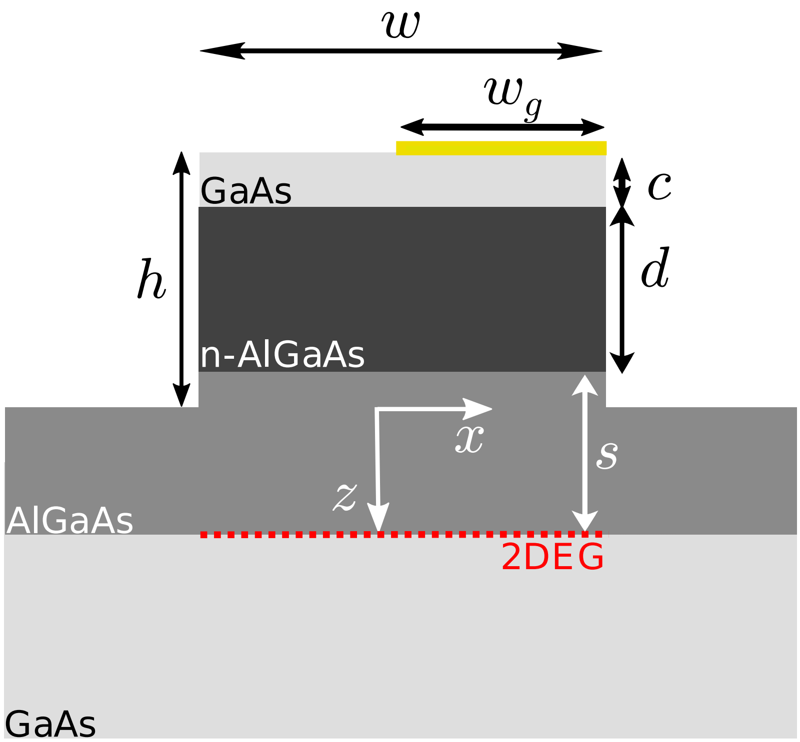

Figure 4.1: A shallow etched wire with a surface gate (gold) applied to the top surface of the etched mesa. The etching passes through the n-doped AlGaAs layer and is based on the model found in Chapter 3. For our calculations we use the parameters found in Table 3.1 and the surface gate will cover half of the surface of the etched mesa.

top of the etched rib. For the rest of this thesis, we use the same width of surface gate as the experimental devices we model given as $w_g = 0.5\ \mu$m. As with the previous chapter defining the etching, we keep $z = 0$ to be at the depth of the etching, where positive z goes into the structure perpendicular to the plane of the 2DEG.

For ease of representation we introduce a “window function” $f(\mathbf{r})$ which takes the value 1 in the areas not affected by etching and 0 everywhere where the heterostructure has been etched. In addition, we apply the same representation to the surface gate by describing the voltage profile applied to them which we denote as the gate function $V(\mathbf{r})$. A benefit of the gate function is that for devices that require multiple surface gates that may have different voltages applied can all be described by this one function.

4.2 Method

For the purposes of clarity we reiterate the following assumptions that were made in the previous chapter. We assume that the potential experienced by the hot electron is determined solely by the applied surface gates and donor ions (assumed to be uniformly

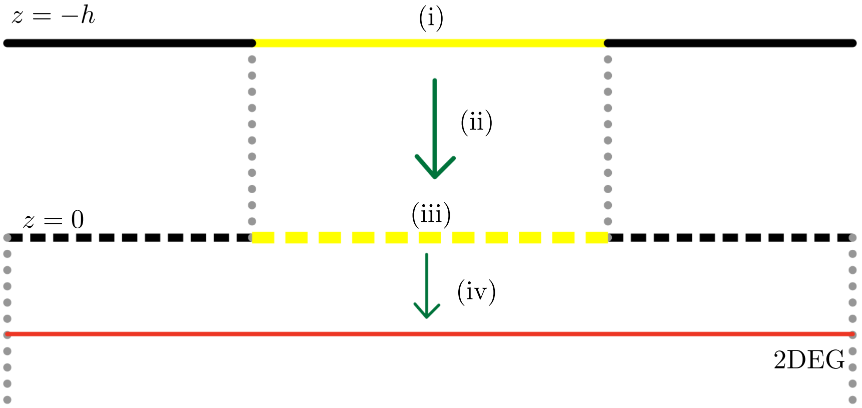

Figure 4.2: A diagram explaining the step by step process of the projected surface method. The outline of the shallow etched wire can be seen by the grey, dotted lines connected to the solid, yellow line and the dashed, black lines. (i) the top of the etched rib is treated like a surface gate (represented as a solid, yellow line). The empty space either side of the top of the etched surface (solid, black lines) are given the boundary conditions of zero. (ii) The first projection calculates the dispersion of the electrostatic potential from $z = -h$ down to $z = 0$. (iii) the boundary conditions are then forced on to electrostatic potential of the first projection where the black,dashed line are set to zero. The calculated electrostatic potential is represented as a surface gate (dashed, yellow line) which has an electrostatic potential which varies in x and we called the projected surface gate. (iv) the second projection is then performed with the projected surface gate and gives us the final electrostatic potential found at the depth of the 2DEG.

distributed in the doped layer), i.e. no self-consistent effects are considered. This assumption is frequently made in modelling gated nanostructures [68, 67, 65] but it is particularly well justified in the hot-electron case as here single electrons are injected into regions underneath the depletion gates where bulk electron density is depleted. With ρ_D as the charge density of the donor ions left by the etching, our task is to solve Poisson's equation:

$$\nabla^2 \varphi = -\frac{\rho_D(\mathbf{R})}{\varepsilon_r \varepsilon_0}, \tag{4.1}$$

subject to boundary conditions defined by the gate voltage function $V_g(\mathbf{r})$ and etching function $f(\mathbf{r})$. Here we use the notation $\mathbf{R} = (x, y, z)$ and $\mathbf{r} = (x, y)$. In addition, the electric field vanishes as $z \to \infty$ [47].
Following the same method as explained in Chapter 3, we begin by decomposing our solution into particular integral and complementary function, $\varphi = \varphi_1 + \varphi_2$ [47]. Choosing φ_1 as solution to Poisson's equation, it is a function of z only, and can be found exactly (see Chapter 3).

Potential φ_2 is then the solution of the corresponding homogeneous Laplace equation $\nabla^2 \varphi_2 = 0$ subject to $\varphi_2 = -\varphi_1 + \varphi$ on the boundaries. In particular, the boundary conditions on the top mesa, in terms of our window functions, read

$$\varphi_2(\mathbf{r}, z = -h) = \varPhi_0 f(\mathbf{r}) + V_g(\mathbf{r}), \tag{4.2}$$

in which we get for $h = c + d$

$$\varPhi_0 = -\frac{eN_D}{\varepsilon_r \varepsilon_0}\{-dh + \frac{1}{2}(c-h)^2\}. \tag{4.3}$$

On the exposed sidewalls of the etched mesa, we have the boundary condition $\varphi_2(z) = -\varphi_1(z)$ with $\varphi_1(z)$ given in Eq. 3.3

In the absence of boundary conditions other than those found at the height of the mesa surface ($z = -h$) the solution of Laplace's equation for the potential at a depth z would be

$$\varphi_2(\mathbf{r}, z) = \int \mathrm{d}\mathbf{r}' K(|\mathbf{r} - \mathbf{r}'|, z + h)\varphi_2(\mathbf{r}', -h), \tag{4.4}$$

with propagator

$$K(r, z) = \frac{|z|}{2\pi(z^2 + r^2)^{3/2}}, \tag{4.5}$$

and where $\varphi_2(\mathbf{r}', -h)$ is as given in Eq. (4.2). Based on this, we write down an approximate expression for the potential at the depth $z = s$ of the 2DEG obtained in two steps. First we use the propagator of Eq. (4.5) to project the mesa boundary conditions down to the level of the bottom of the etching ($z = 0$). We then approximate the full potential at this depth by multiplying this with the etched function $f(\mathbf{r})$, which imposes the surface boundary condition on φ_2 at this point. To obtain the potential at $z = s$ we once more propagate downwards with Eq. (4.5). Since $\varphi_1(\mathbf{r}, s) = 0$, we have $\varphi(\mathbf{r}, s) = \varphi_2(\mathbf{r}, s)$ and thus the resultant approximate closed-form expression for the potential at the 2DEG is

$$\begin{aligned}\varphi(\mathbf{r}, s) = &\int \mathrm{d}\mathbf{r}' K(|\mathbf{r} - \mathbf{r}'|, s) f(\mathbf{r}') \\ &\times \int \mathrm{d}\mathbf{r}'' K(|\mathbf{r}' - \mathbf{r}''|, h)\varphi_2(\mathbf{r}'', -h)\end{aligned} \tag{4.6}$$

A detailed diagram showing the process of Eq. 4.6 and hence the projected surface method can be seen in Fig. 4.2.

In certain cases (see below) one of the two integrals in Eq. (4.6) can be evaluated analytically, but generally we evaluate both numerically. This we do by uniformly discretising

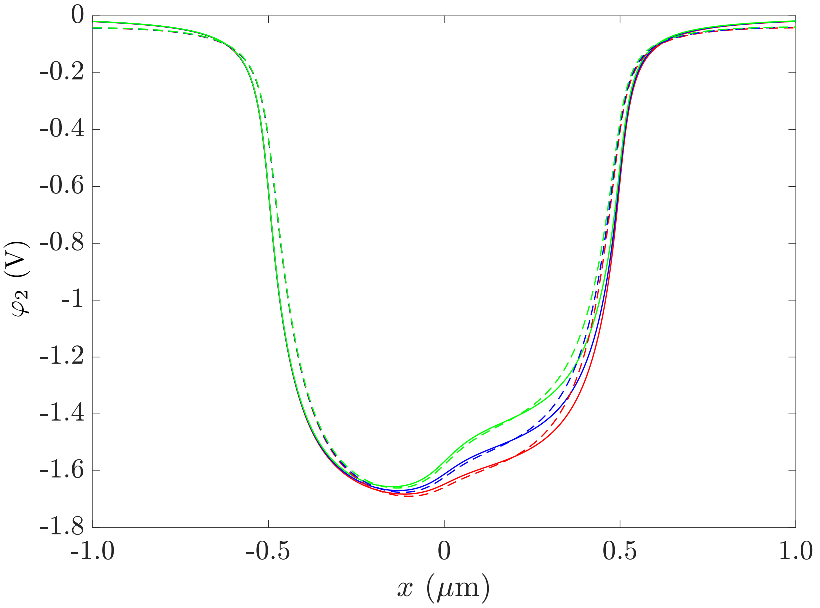

Figure 4.3: The electrostatic potential calculated at the depth of the 2DEG using the projected surface method (solid lines) and the FEM (dashed lines). A surface gate of width $w_g = 0.5$ μm occupies the region $0 < x < 0.5$ μm and is shown having three voltages applied: $V_g = -0.35$ V (green), $V_g = -0.25$ V (blue), and $V_g = -0.17$ V (red). The shallow etched rib measures $w = 1$ μm wide and the 2DEG is found 90 nm away from the top of the etched rib's surface.

the $x - y$ plane in a rectangular grid with a step size of $\mathit{\Delta}$. The propagator $K(r, z)$ is a peaked function of r with width $\sqrt{2}z$. Thus, in order to accurately resolve this function and obtain a good approximation to the integrals in Eq. (4.6), we require $\mathit{\Delta} \ll \sqrt{2}z$ for the relevant values of z, i.e. we require $\mathit{\Delta} \ll \sqrt{2}h$ and $\mathit{\Delta} \ll \sqrt{2}s$.

Once in possession of the potential, we can obtain an expression for the instantaneous electron velocity based on the perturbative method in Ref. [49]. Let y' be the instantaneous transport direction and x' the direction transverse to it. Then, under the assumption that the scale of variation of the potential is large compared with both the cyclotron radius and the size of the wave packet in the transport direction, the energy of an electron at $\mathbf{r}' = (x', y')$ can be written approximately as $E = \frac{1}{2}\hbar\omega_c + U(\mathbf{r}')$ where ω_c is the cyclotron frequency and $U(\mathbf{r}') = -e\varphi_2(\mathbf{r}')$ is the potential energy at the depth of the 2DEG. This expression assumes that the electron remains in the lowest Landau level. In the local coordinates system, the speed of the electron in the y' direction is given by $v = (eB)^{-1}\partial U/\partial x'$. Moving back into the original coordinate system and defining electric field $\mathbf{E} = -\nabla\varphi_2$, we

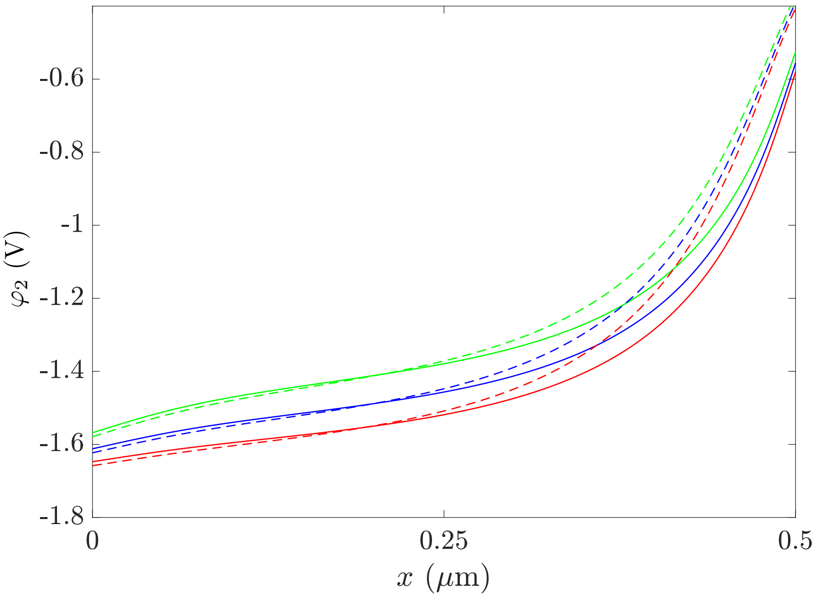

Figure 4.4: A closer view of the electrostatic potential φ_2 shown in Fig. 4.3. The region shown is directly underneath the surface gate where the etched mesa ends at $x = 0.5\,\mu$m.

find the drift velocity of the electron to be

$$\mathbf{v} = \frac{1}{B^2}\mathbf{E} \times \mathbf{B}, \tag{4.7}$$

derived from the Lorentz force of an electron in a magnetic and electric field, $F_L = e\mathbf{E} + e\mathbf{v} \times \mathbf{B}$, and matches the semi-classical drift velocity [13]. We assume that the electron travels along an edge channel with constant φ_2 and we will in the next chapter how we can perform analysis on the hot-electrons velocity.

4.3 One-dimensional transport

We first apply the projected surface method to a 2D cross-section of a simple shallow etched wire with a surface gate shown in Fig.4.1. An etched rib of width w has a surface gate applied to it's surface of width w_g. For our calculations we use $w = 1$ μm and $w_g = 0.5$ μm, such that the gate covers half the etched rib's surface, with the usual parameters for the rest of the heterostructure (see Table 3.1). This model can be considered as a cross-section of an infinitely long shallow-etched wire with a surface gate. This simplifies the problem by solving for the electrostatic potential translationally invariant in the transport direction. We note here that we will refer to modelling a 2D model as 1D transport modelling as we have restricted the motion of the electron to 1D.

Figure 4.3 shows the electrostatic potential calculated using the projected surface method (solid lines) and the FEM (dashed lines) both for the full domain in x and for the region directly below the surface gate found in $0 < x < 0.5$ μm. The figures shows the calculations for three difference voltages applied to the surface gate: $V_g = -0.35$ V (green), $V_g = -0.25$ V (blue), and $V_g = -0.17$ V (red). These values of voltages applied to the surface gate are chosen to be the same as the experimental values we will analyse in the next chapter. The most notable difference between the two calculations, for the multiple V_g, is the difference in φ” close to the edges of the etched rib. The FEM narrows the electrostatic potential much more than the projected surface method. There are two factors to consider: the boundary condition of the exposed etched sidewall, and the meshing used by the FEM. As calculated in the previous chapter the boundary condition of the exposed etched sidewall is parabolic in z and dependent on the depth of etching and the depth of the n-doped AlGaAs layer. However, this boundary condition is not accounted for in the projected surface method. The shallowness of the etching creates volumes within the 3D model that have sharp edges and require small sized meshing to accurately calculate the effect the boundary conditions have.

It can be seen more clearly in Fig.4.4, under the surface gate where it is assumed injected electrons would be found, that there are regions where the difference between ϕ for the projected surface method and the FEM are not as great and are equal. In the next chapter we will show that, compared with experimental results, the electrons will be seen to occupy the regions where we can see a closer match in electrostatic potential in this figure.

A reason why there is such a difference, however, may be due to the lack of implementation of the boundary condition of the exposed sidewall of the etched rib. However, even though the projected surface method does not take this into account, we find that it results in a good approximation with the benefits of offering an analytical expression and simplicity in its calculation. We will show in a later chapter on realistic device potentials that the approximation made by the projected surface method is suitable when comparing with experimental results.

4.4 Two-dimensional transport

We continue with our testing of the projected surface method to modelling a full 3D device. This 3D model consists of the model shown in Fig. 4.5a. The etched mesa continues

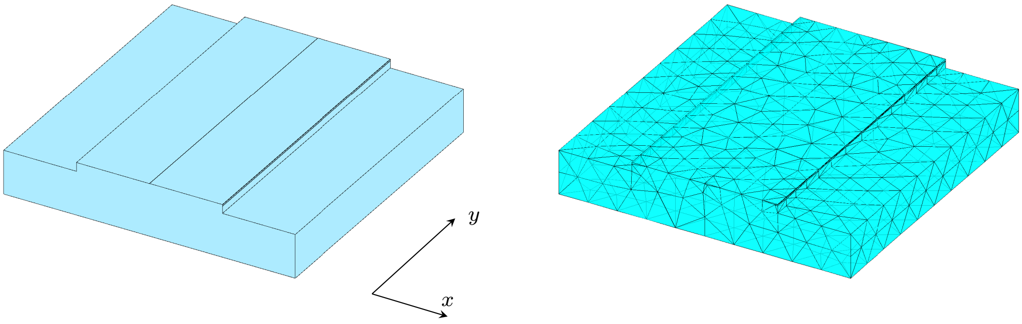

(a) (b)

Figure 4.5: (a) Three-dimensional model of a shallow etched quantum wire used by the FEM. The model is the exact same as Fig. 4.1 in the x direction but extended in the y-direction. As the potential is therefore invariant in the y direction it can be scalable to any size. For our calculations we choose the length of the shallow etched wire to be $5\,\mu$m. The etched mesa can be seen in the centre of the bulk of the model, where a line intersects it down the middle. This line represents the divide between the free surface of the etched mesa (left side) and the depletion gate (right side). (b) The tetrahedral meshing of the model (a). In this case, a large size meshing is used for visualisation purposes and a smaller meshing size would be used for the numerical calculations.

to have the same parameters as the previous one-dimensional transport model. Although this model still restricts the electron to 1D travelling in one direction along the wire, for future, more complicated models, we refer to it as a 2D transport model.

The FEM requires boundary conditions applied to all surfaces of the model and a tetrahedral mesh (shown in Fig. 4.5b) within the structure in order to calculate Laplace's equation for each subdomain. Therefore, in order to calculate the electrostatic potential at the depth of the 2DEG the entire model must be calculated for. However, the projected surface method only requires the boundary conditions of the top surface of the etched rib, including the depletion gate, and the free surface exposed from etching. In addition, the calculation can be done only once for the exact depth of the 2DEG without wasting computational cost on the rest of the model which is unimportant. For our calculations, we assume this model is identical in the x direction to the model shown in Fig. 4.1 with the same parameters of the layers in the z direction. This means that the model is invariant in the y direction and therefore scalable, however in our numerical calculation we assume the length of the shallow etched wire is $L_y = 5\,\mu$m. The model shown in Fig. 4.5a is only used for the FEM calculation, which in itself is already an extra computational task to create, while we only use details about where the etched region, depletion gate, and free surface mesa lie on the surface of the model.

Figure 4.6a shows the (x, y)-plane of the electrostatic potential at the depth of the

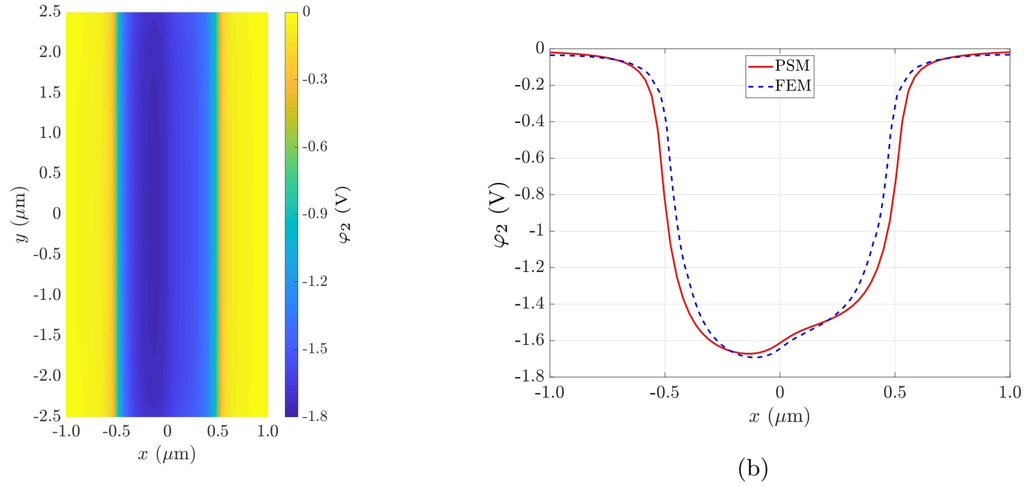

(b)

(a)

Figure 4.6: (a) The electrostatic potential in the xy-plan at the depth of the 2DEG inside the shallow etched wire calculated using the projected surface method. A depletion gate with a voltage $V_g = -0.25\,\text{V}$ is applied. (b) The electrostatic potentials from (a) at $y = 0$ taken along the x-axis. The red line represents φ_2 calculated by the projected surface method and the dashed blue line represents φ_2 calculated by the FEM.

2DEG calculated using the projected surface method. For this result, only the window functions describing the position of the etched region, the free surface of the etched mesa, and the depletion gate are required. This model specifically shows a quantum wire, in which an electron would be travelling in the y-direction. Although it is technically a restriction to a 1D transport movement, a different model could be used to change the direction of the electron along the xy-plane, as we will see in later chapters.

Figure 4.6b shows the comparison for the calculation of the electrostatic potential at the depth of the 2DEG for the model shown in Figure 4.6a using the projected surface method (solid, red line) and the FEM (dashed, blue line). A voltage $V_g = -0.25$ V is applied to the surface gate. For 1D transport, the results are shown to be the same as for the 2D transport, in which the FEM has narrowed the electrostatic potential slightly more than the projected surface method. In this case, modelling 2D transport, the effect of the sidewalls are slightly greater than that of the 1D. When considering the change in the meshing of the FEM, using triangles in 1D and tetrahedrals in 2D, the complexity in the calculations increase and reduce accuracy with the limitations on the cost of computation.

4.5 Chapter summary

We have shown in this chapter the projected surface method and applied it to 1D and 2D transport models using a simple shallow etched wire with a surface gate, a typical component of a HEQO device. The comparison between the projected surface method and the FEM highlights some assumptions made for the projected surface method and how approximate the results are. However, for the important features we wish to study within HEQO devices such as trajectory and velocity of electrons it gives good results that we can continue with and apply to realistic device potentials. It is important to note that the projected surface method does not offer an exact solution but instead offers advantages over other methods of the FEM. We have taken the approach of being able to analytically solve the electrostatic potential due to a surface gate, using Davies' surface gate method [32] which is an exact solution, and tried to shape it into a form which will also accommodate regions of etching in our heterostructures. Although the models we have shown in this chapter are rather simple they have proven useful in creating the foundation from which we are able to make and test the projected surface method. In the next chapter we will take the projected surface method further by looking to apply it to a realistic device model. We will also show how we can use the electrostatic potential to calculate properties of the experimental devices and compare with the experimental data to test our method further.

Chapter 5

Realistic device potentials

Having shown that the projected surface gate method provides an electrostatic potential which is comparable to the an electrostatic potential calculated using the FEM, we progress further looking into more detail of the certain experiments. In particular we look at the TOF experiment and a MZI.

5.1 Time of flight experiment

The TOF experiment is used to determine the velocity of injected hot-electrons using a time-resolved method [45] and can offer an energetic landscape for hot-electrons to travel to study their LO-phonon emission rates [48]. Figure 5.1 shows the (x, y) plane of the surface of the TOF device. The figure shows two different types of surface gates which we define as: the depletion gate (grey) which depletes background electrons while creating the edge states where the hot-electron will travel, and the deflection gate (green) which depending on the applied voltage will control the path the electron will take. The dark blue region represents the area where the heterostructure is etched while the rest of the figure shows the etched mesa. The hot-electron is injected into the bottom left of the model (black dot), underneath the depletion gate with applied voltage V_g, travelling toward the deflection gate. At this point there are two paths the electron can travel depending on the deflection gate voltage V_d. A large negative bias will cause the electron to be deflected upward (positive y direction) following the depletion gate. A low negative bias will allows the electron to travel underneath the deflection gate and back under the depletion gate on the right of the model. Then, both paths recombine and continue on to a detector (outside of our model). The emission and detection time can be recorded and by knowing the difference in the distance of the two paths, measured by the geometry of the model and not the electron's actual path, the drift velocity can be deduced.

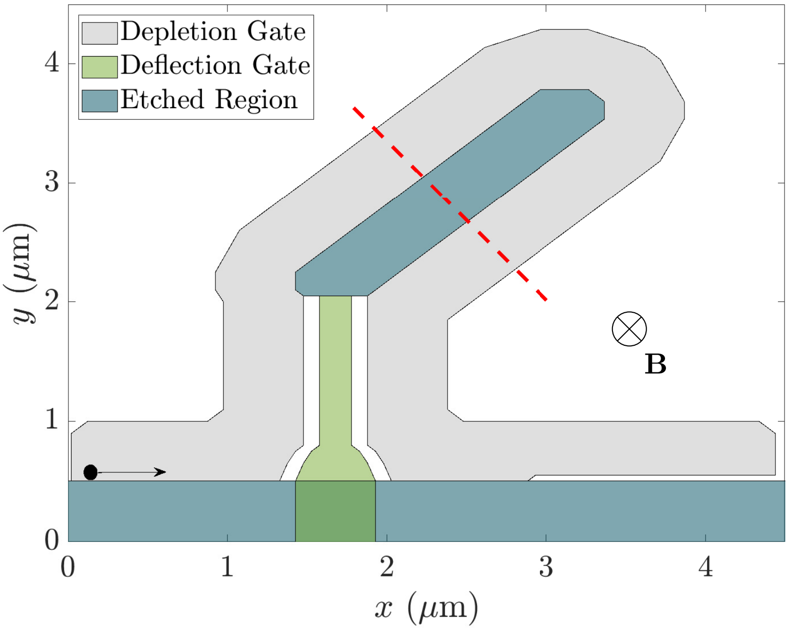

Figure 5.1: Time-of-flight model showing surface geometry with electrostatic gates and chemically etched regions. The design is based on that in Ref. [45], but with a truncated loop section. Hot electrons are injected into the bottom left of the device (black dot) and travel along an edge channel beneath the depletion gate (grey) on the edge of the etched region (blue). Depending on the voltage V_d applied to the deflection gate (green) electrons either travel underneath it via a short path or are deflected by it and thus travel around the long path of the loop. The red dashed line shows the location of the section shown in Fig. 5.2.

In the long path of the TOF experiment, it is the straight portions of loop that constitute the majority of the electron paths in the circuit. We can thus obtain a picture of electron travel in the loop arms by considering a problem translationally invariant in the transport direction with a cross section as in Fig. 5.2, where the red, dashed line in Fig. 5.1 is drawn. The model is now essentially two shallow etched wires with surface gates of width w_g separated by an etched region of width w_e. As with previous models, $z = 0$ is defined at surface of the exposed etched region and $x = 0$ is at the centre of the model with symmetric structure either side.

5.2 One-dimensional transport

Although we showed in Chapter 4 the projected surface method for one-dimensional transport, we take this opportunity to apply it to a model which is more realistic by studying a model with two etched mesas with depletion gates in close proximity. We consider transport under one of the two depletion gates as, apart from direction of travel, transport in each half is identical. We still consider both halves in the potential calculations,

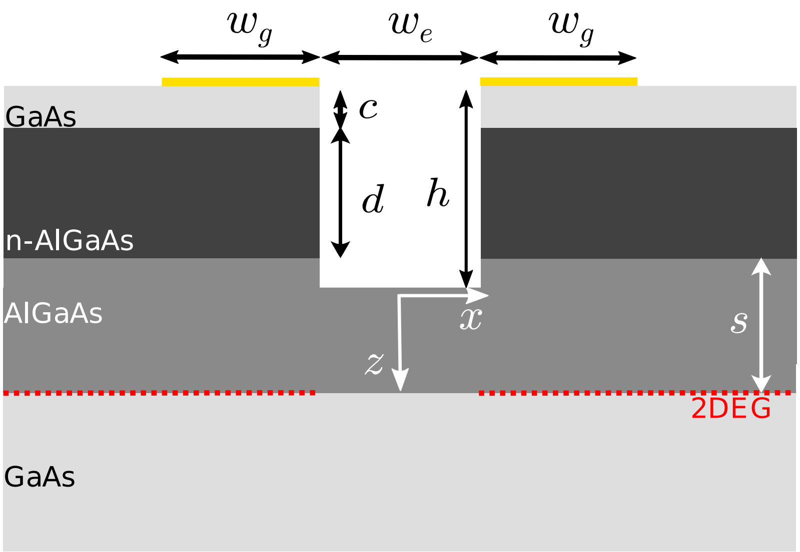

Figure 5.2: Two-dimensional cross-section along the red, dashed line in Fig. 5.1. The hetereostucture consists of a cap layer of GaAs, a layer of n-doped AlGaAs and a spacer layer of undoped AlGaAs of depth with depths c, d , and s respectively. Etching to a depth h is present, with the distance between the etched mesas given as w_e, arranged symmetrically about $x = 0$. The depletion gate is shown in yellow with a width of each part w_g. For our calculations we set $z = 0$ at the bottom of the etching with the positive direction into the bulk. Table 3.1 shows the parameters for the depth of each layer and the etching for this model.

however, as the potential under one gate is affected by the other. With y the transport direction, the window functions are functions of x only: we have $f(x) = \theta\left(|x| - \frac{1}{2}w_e\right)$ and $V(x) = \theta\left(|x| - \frac{1}{2}w_e\right)\theta\left(-|x| + \frac{1}{2}w_e + w_g\right)$ where θ is the unit step function. Then, because of translational invariance, we can integrate out the y coordinate in the propagator of Eq. (4.5) to obtain $\widetilde{K}(x,z) = \int K(\mathbf{r},z)dy = |z|/[\pi(x^2+z^2)]$. Then, because the potential at $z = -h$ is piecewise constant, we can perform the first of the integrals in Eq. (4.6) (corresponding to the projection from $z = -h$ to $z = 0$) analytically, with the result

$$\begin{aligned}\varphi_2(x,s) \quad = \quad & \sum_{\sigma,\sigma'=\pm1}\int_{\frac{1}{2}w_e}^{\infty} \mathrm{d}x'\,\widetilde{K}(|x+\sigma' x'|, s) \\ & \times\left[\Phi_0 g\left(\sigma x', \tfrac{1}{2}w_e, \infty, h\right)\right. \\ & \left. + V_g g\left(\sigma x', \tfrac{1}{2}w_e, \tfrac{1}{2}w_e + w_g, h\right)\right], \qquad (5.1)\end{aligned}$$

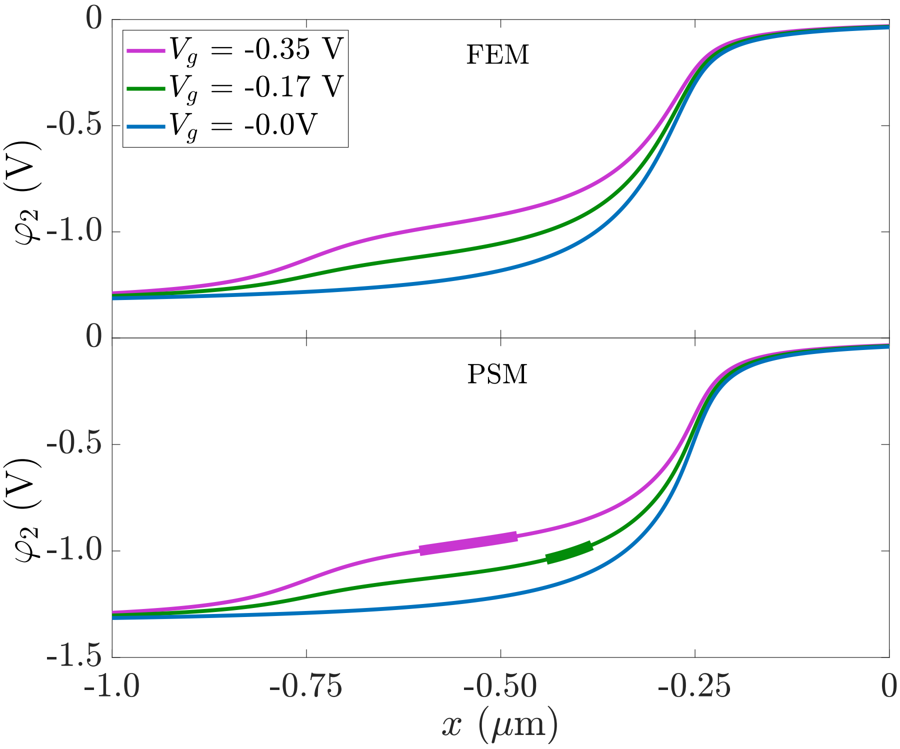

Figure 5.3: Electrostatic potential of the 1D transport model with cross-section in Fig. 5.2 calculated using: (Top) the finite element method (FEM) and (Bottom) the projected surface method (PSM). The complete potential is symmetric about $x = 0$ and here we plot only the left side i.e. $x < 0$. The widths of the etched region and width of depletion gate were $w_e = w_g = 500\,\mathrm{nm}$ and results for three different depletion gate voltage V_g are shown. The thicker regions on the bottom curves highlight the regions where the electrons have velocities comparable with those seen in the experiment [48] as shown in Fig 5.4.

.

in terms of the function

$$
\begin{aligned}
g(x, A, B, z) &\equiv \int_A^B \mathrm{d}x' \widetilde{K}(|x - x'|, z) \\
&= \frac{1}{\pi}\left\{\tan^{-1}\left[\frac{x-A}{|z|}\right] - \tan^{-1}\left[\frac{x-B}{|z|}\right]\right\}.
\end{aligned}
$$

To evaluate the performance of the projected surface method we compare results with those from a FEM calculation [71]. We apply the parameters $w_e = w_g = 500\,\mathrm{nm}$ to match with the geometry of the TOF experiment [48] and consider results for three different gate voltages. As the model is symmetric about $x = 0$ for the following calculations we will focus our attention on the edge state created by the left depletion gate and etched mesa. The FEM is performed on a two-dimensional domain, the size of which is chosen so that the artificial boundary conditions do not affect the potential in the region of electron

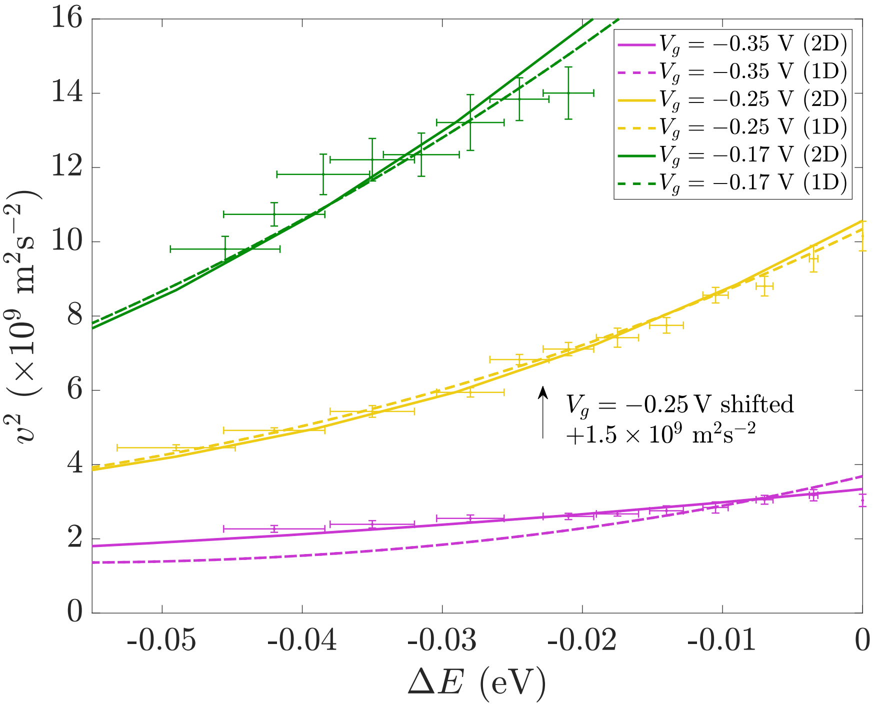

Figure 5.4: Square of electron velocity v^2 against the relative energy $\mathit{\Delta} E$ for depletion gate voltages $V_g = -0.17\,$V (purple), $V_g = -0.24\,$V (blue), and $V_g = -0.35\,$V (green). The points with error bars are experimental results provided from Ref. [48], the dashed lines show results obtained from the 1D transport model, and the solid lines shows those from the full TOF model of Sec. 5.3. Theoretical results have been fitted to experimental data with a single parameter, E_{fit}, that sets to zero for $\mathit{\Delta} E$. For clarity the $V_g = -0.25\,$V results have been shifted upwards by $+1.5 \times 10^9$ m^{2}s^{-2}.

transport. Numerically we found that a domain 4 μm either side of $x = 0$ and a depth of $z = 10$ μm was required to obtain convergence. The FEM was implemented on this area with a triangular meshing for which the maximum vertex spacing was set at 3 nm. The projected surface method expression only has a single integral to be evaluated numerically, and convergence for this was obtained with an upper limit of integration of 3 μm and with a step size of $\mathit{\Delta} = 1\,$nm.

Figure 5.3 shows a comparison between the electrostatic potential calculated with the FEM (top) and the projected surface method (bottom). The highest and lowest absolute values of ϕ are found underneath the free surface and the etched surface respectively. Separating the two is a third region the height of which is controlled by the depletion-gate voltage. The FEM and projected surface method calculations show good agreement, giving potentials of similar shape and magnitude with the highest and lowest values differing by about 1%. We also observe small differences in the gradient of ϕ but these are again of the order of 1%. Since this gradient gives the transverse electric field, by Eq. (4.7), the differences in the velocities predicted by the two methods will also be of the order 1%.

In Fig. 5.4 we compare the results of the projected surface method velocity calculation with those obtained in the experiment of Ref. [48]. In the experimental data, the energy $\varDelta E$ is an arbitrary relative energy defined such that $\varDelta E = 0$ for the highest energy considered for the given depletion gate voltage. We can derive the corresponding quantity in our calculation from Eq. 2.37 from which we find $\varDelta E = E - \frac{1}{2}\hbar\omega_c + E_{\text{fit}} = U(x) + E_{\text{fit}}$ where E_{fit} is a free parameter that reflects the unknown offset between experimental and theoretical energies and that we treat here as a fit parameter. We also use our calculated electrostatic potential to get he potential energy such that $U(x) = -e\varphi_2$. We assume that the rest of the electrostatic potential, φ_1, will incorporated by E_{fit}. We mentioned in the previous chapter how we have ignored the screening effect caused by metallic gates. As discussed, were we to take it into account it would likely lead to a reduction in N_D and hence a reduction in our calculation of $\varPhi_0$. As such, our free fit parameter can allow us to offset such a reduction, assuming that effect was not proportionately large. As in Ref. [48], we plot v^2 against the energy because of the expectation of a linear relationship between these quantities in the case of parabolic potential confinement. The dashed lines in Fig. 5.4 show the results of our calculations with E_{fit} found with a least-squares fit. Between the experimental data and our calculations there is a good agreement in magnitude of v^2 and general trend with $\varDelta E$. For $V_g = -0.35\,\text{V}$ our 1D calculations overestimate the observed velocities somewhat but show similar trend.

Having obtained E_{fit}, we can invert the relationship between $\varDelta E$ and $U(\mathbf{x})$ to identify the transverse position of electron for the energy ranges considered in Fig. 5.4. These regions are indicated in the bottom panel of Fig. 5.3 for $V_g = -0.17\,\text{V}$ and $V_g = -0.35\,\text{V}$ In both cases, the occupied regions of the potential lie under the depletion gate with the $V_g = -0.35\,\text{V}$ results lying further away from the etched region, i.e. more towards to the outside of the loop. For $V_g = -0.17\,\text{V}$ the occupied potential is close to being parabolic across the probed region, and thus the relationship between $\varDelta E$ and v^2 is approximately linear. For $V_g = -0.35\,\text{V}$, the occupied potential is at the edge of the shelf region where it is almost a linear potential and this gives rise to an almost-flat v^2–$\varDelta E$ curve.

5.3 Full TOF model

We now apply the projected surface method to the model of the full TOF geometry shown in Fig. 5.1 and evaluate the integrals in Eq. (5.1) by discretising the surface with a square mesh of spacing $\varDelta = 1\,\text{nm}$. Once in possession of the 2D electrostatic potential at the

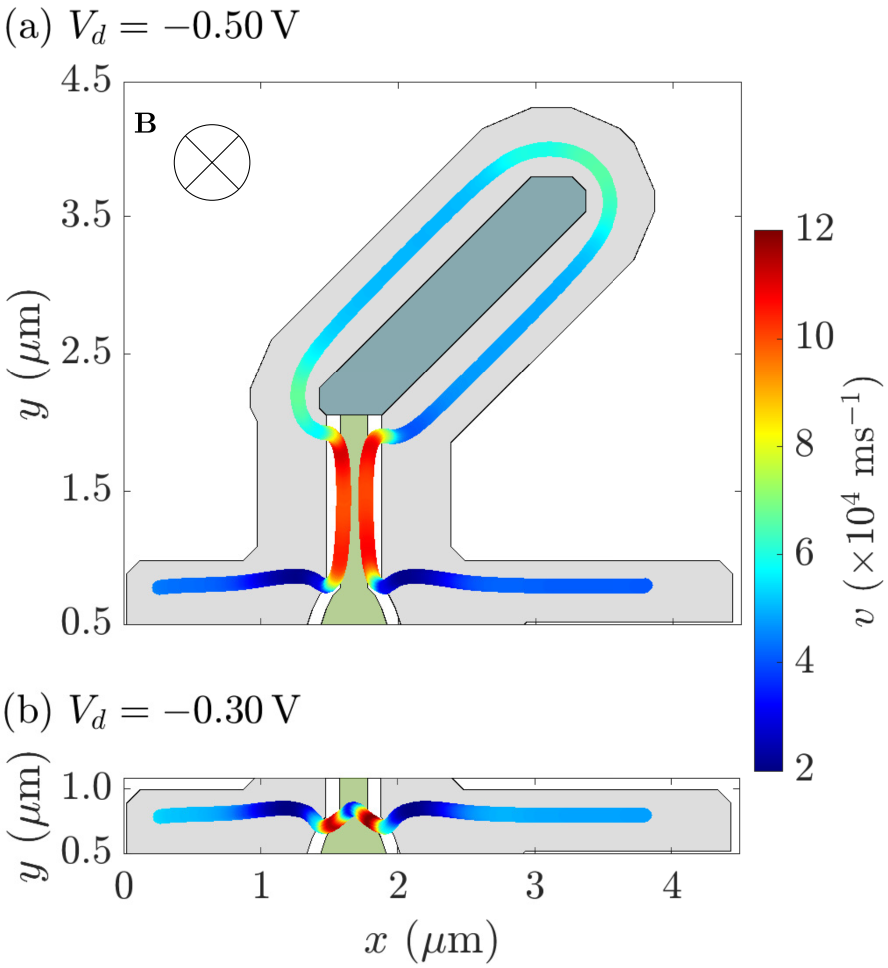

Figure 5.5: Two hot-electron trajectories through the TOF geometry of Fig. 5.1 where the instantaneous velocity is shown with a colour scale. (a) The long path has the applied deflection gate voltage $V_d = -0.50\,\mathrm{V}$, following the majority of the depletion gate. (b) The short path has a voltage $V_d = -0.30\,\mathrm{V}$ and shows the hot-electron travelling underneath the deflection gate. Both paths have a depletion gate voltage $V_g = -0.25\,\mathrm{V}$ and show variations in the velocity, the most notable of changes occurring around the deflection gate.

depth of the 2DEG we identify electron trajectories as continuous equipotentials selected by the starting position of the electron at the bottom left of the device as in Fig. 5.1. As the electric field is in the y-direction in the injection region, the energy of the electron is varied by changing its initial position relative to the y-axis. Figure 5.5 shows two trajectories obtained with the same injection point and depletion gate voltage ($V_g = -0.25\,\mathrm{V}$), but with two different values of deflection gate voltage: $V_d = -0.50\,\mathrm{V}$ and $V_d = -0.30\,\mathrm{V}$. This change in the deflection gate voltage is sufficient to control whether the electron takes the long ($V_d = -0.50\,\mathrm{V}$, Fig. 5.5(a)) or the short ($V_d = -0.30\,\mathrm{V}$, Fig. 5.5(b)) path in the TOF model. Note that even when set to $-0.30\,\mathrm{V}$ and the short path is selected, the trajec-

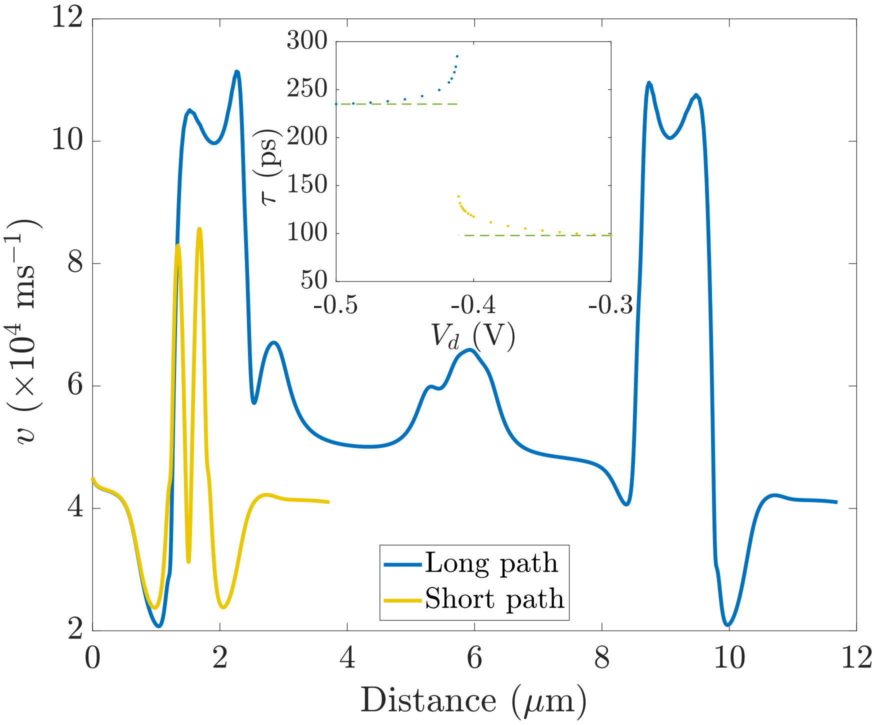

Figure 5.6: Plot of the instantaneous velocity against distance travelled along two trajectories: the long path with $V_d = -0.50\,\mathrm{V}$ (blue) and the short path with $V_d = -0.30\,\mathrm{V}$ (red). The inset shows the time of flight of a hot electron at a constant energy as a function of the deflection gate voltage, V_d. The dashed lines shows the value of τ for a voltage V_d in the saturation region for the long path and the short path. The difference between the two represents $\Delta\tau$ and is used to calculate the drift velocity.

tory of the electron is still affected by the deflection gate giving a path that is not straight.

The instantaneous velocity of the electron along the trajectory is indicated by the plot colour in Fig. 5.5 and is also shown for the two highlighted trajectories as a function of distance travelled in Fig. 5.6. Away from the deflection gate area, the electron velocity is reasonably constant with a value of around $5.6 \times 10^4\,\mathrm{ms}^{-1}$ for the parameters used here. In contrast, the rapid variations in the potential around the deflection gate give rise to large variations in the electron speed, with a minimum of $2.1 \times 10^4\,\mathrm{ms}^{-1}$ and a maximum $11.1 \times 10^4\,\mathrm{ms}^{-1}$ for $V_d = -0.50\,\mathrm{V}$.

Whilst the instantaneous velocity gives insight into the electron behaviour, it is not directly accessible in experiment. Rather, experiments have access to the total time of flight τ from source to detector which, when combined with an estimate of the path length, can give an estimate of the drift velocity, suitably defined. In our calculation the time of

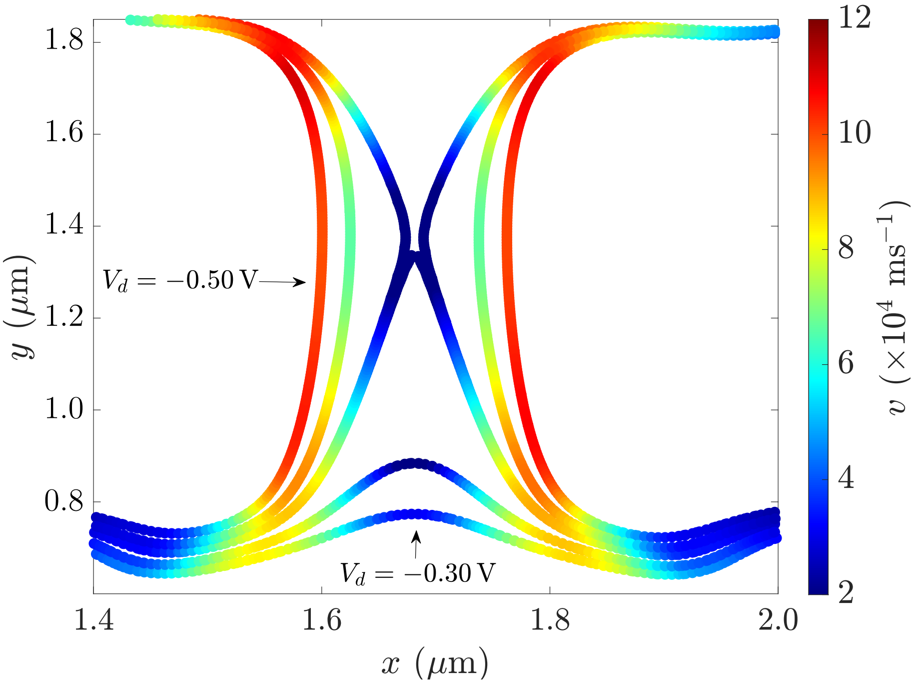

Figure 5.7: A close up view of electron paths around the deflection gate for different values of the deflection gate voltage, V_d. From the bottom up we have short paths gives by voltages $V_d = -0.30$ V (labelled), $V_d = -0.35$ V, and $V_d = -0.404$ V, the latter being the closest to the transition point. Three long-path trajectories are also shown. From left to right, these are at voltages $V_d = -0.50$ V (labelled), $V_d = -0.45$ V, and $V_d = -0.405$ V at the transition point.

flight is obtained via the integral

$$\tau = \int \frac{1}{v(s)} \mathrm{d}s, \tag{5.2}$$

where ds is a line element along the trajectory and $v(s)$ is the instantaneous velocity at a distance s. The inset of Fig. 5.6 shows the time of flight as a function of the deflection gate voltage with other parameters as in Fig. 5.5. We see that at a deflection gate voltage of $V_d = -0.405$ V there is a transition between the electron travelling in the long path and short path. Mirroring the experimental procedure [45], the drift velocity is obtained from this TOF information as follows. To find the difference in TOF, $\Delta\tau$, we use the values of τ for $V_d = -0.50$ V and $V_d = -0.30$ V. These values can be seen in the inset of Fig. 5.6 marked as the dashed lines, which are well within the saturation zone of the long and short path respectively. Then, we take the difference in length of the two paths, ΔL, in Fig. 5.6 and calculate the drift velocity $v_d = \Delta L/\Delta\tau$. For the two paths in Fig. 5.5 the drift velocity is thus calculated to be $v_d = 5.3 \times 10^4$ m/s, which is also 5% different to the instantaneous value found along the straight sections of the loop.

Results for the drift velocity as a function of relative energy ΔE are shown alongside the 1D results and experimental data in Fig. 5.4. For these results, the difference in path length and TOF were measured for two paths acquired using the deflection gate voltages $V_d = -0.50\,\mathrm{V}$ and $V_d = -0.30\,\mathrm{V}$. For depletion gate voltages $V_g = -0.17\,\mathrm{V}$ and $V_g = -0.25\,\mathrm{V}$, results from the 1D and 2D calculations are very similar and give a similar level of fit to the experimental results. For $V_g = -0.35\,\mathrm{V}$, the overall magnitude of the 2D results is closer to the experiment, but these results no longer show the plateau behaviour seen from the 1D calculation and that appears to be present in the experimental data. This is due to the difference in relative energy for the 1D and 2D calculations when comparing with the experimental data. The plateau is still present within the 2D calculations, however the position of the ΔE-range is now closer to the etched edge of the mesa as compared with the 1D calculation in Fig. 5.2. In Fig. 5.7, we focus on the behaviour of electron trajectories around the deflection gate as its voltage is swept through the transition from short to long path. By fine tuning V_d we show additional trajectories in Fig. 5.7 encompassed by the long and short path we have discussed (labelled). At the centre of the figure we see a transition between the long and short path where $V_d = -0.405\,\mathrm{V}$ and $V_d = -0.404\,\mathrm{V}$ respectively. As the absolute voltage is decreased from $V_d = -0.50\,\mathrm{V}$ and increased from $V_d = -0.30\,\mathrm{V}$ two observations can be made: the length of the path increases as it moves closer to the centre of the deflection gate ($x \approx 1.7\ \mu\mathrm{m}$) and the velocity decreases. The latter is much more prominent for the long path and this change can be seen in the inset of of Fig. 5.6 where τ is largest at $V_d = -0.405\,\mathrm{V}$. We also see that the difference between the saturated τ (marked as a dashed line) and largest value of τ for each path is greater for the long path as the effects are doubled as the electron travels around the deflection gate twice.

The TOF experiment calculates the drift velocity with the measured time-of-arrival of the hot-electron and a distance the hot-electron travel. However, the distance it travels is measured using the geometric parameters (i.e. along the edges of the surface gate) of the device which can be difficult to accurately measure [45]. Our semi-classical analysis of the hot-electron paths does show that they do travel close to where they are thought to travel in the experiment. However, even if the true length of the trajectory were known in the experiment, our calculations would be adjusted relative to this change by the energy offset. A key result of this section is that the instantaneous velocity of the hot-electron varies dramatically within the device. By adjusting the energy region to match with the TOF data, it does not matter the overall distance the hot-electron travels, our calculations will still take into account the complex geometry of the device modelled and show characteristic features of the experiment, in particular where the energy of the hot-electron is represented spatially within the device.

It is important to note that throughout this thesis, we have assumed that the hot-electron is travelling in the lowest subband, where our calculations do not consider higher subbands. The reason for this is that the gap between the lowest subband and the next higher subband is $\sim$ 50-100 meV. Another reason is that even if the hot-electron were injected straight into a higher subband, this would result in a slower drift velocity which isn't see in the experiment i.e. there is no sharp change in drift velocity for hot-electrons injected at $\varDelta E = 0$ and the lower energy injections.

In this chapter we have applied our projected surface method to a complex device that uses both etching and multiple types of depletion gates. This method was applied to two models of a hot-electron TOF experiment: a 1D wire and the full 2D geometry. In both cases we used the resulting electrostatic potential to calculate the electron velocity, and both sets of results were shown to give a reasonable account of the experimental drift-velocity data of Ref. [48]. Only at higher absolute depletion gate voltages there were discrepancies both between the two approaches and experimental data. This similarity suggests that composite quantities like the drift velocity and τ in TOF experiments can well be understood in terms of behaviour in the loop arms only. However, if we need a detailed understanding of the trajectories and instantaneous velocity we should use the 2D calculation. This is evident in the calculation of the TOF in the 2D model as a function of deflection gate voltage V_d. These results show the transition point between the long and short path which matches well the experimental results.

Part III

HEQO simulations

Chapter 6

Numerical simulations

In part II we explored the effects that experimental fabrication can have on the foundational heterostructure of HEQO devices and how this can be exploited to manipulate the motion of the electron. Our study has provided us with the projected surface method to allow us to obtain approximations of the electrostatic potential felt by the electrons at the depth of the 2DEG. Furthermore, semi-classical analysis gave us insight into the motion of the electron which we were able to verify the validity of our method with good comparisons to the results of the TOF experiment.

In this chapter we look at the numerical method to simulate an electron, modelled as a Gaussian wave packet, around our modelled potentials. This method was set out by Andrea Bertoni where in Ref. [72] a wave packet is simulated around a Mach-Zehnder interferometer. However, these simulations do not take into account the requirements needed for hot-electrons. We will show the numerical method for evolving a wave packet in time through a modelled system. We then look at the limiting factors we need to take into account when performing these simulations on HEQO devices.

6.1 Numerical method

In order to simulate how an electron propagates within edge channel, we model it as a wave-function and in its simplest form we look to solve the time-dependent Schrödinger equation [73]

$$i\hbar\frac{\partial}{\partial t}\Psi(\boldsymbol{r},t) = \hat{H}\Psi(\boldsymbol{r},t) \tag{6.1}$$

were the Hamiltonian, $\hat{H} = \hat{T} + \hat{V}$, is the sum of the kinetic and potential energy respectively of our system. In the case of modelling experimental devices, we use the potential energy calculated from our computational models to form the geometry of the edge channels in our system. The solution is given as the initial state at $t = 0$ being acted on by the evolution operator given as:

$$\hat{U}(t) = e^{-\frac{i}{\hbar}t\hat{H}} \tag{6.2}$$

which is the operator for the time-dependent Hamiltonian. However, this is not the case as the wave-packet evolves in our system. For this solution to apply, for each time step in the evolution of the wave-packet, the time interval δt must be small enough such that the difference between two consecutive points is infinitesimal. Therefore the evolution operator is given as

$$\hat{U}(\delta t) = e^{-\frac{i}{\hbar}\delta t\cdot\hat{H}(t)} \tag{6.3}$$

as $\delta t \to 0$. To now find how the wave-function has evolved to time t we can perform δt over N successive applications such that $t = N\delta t$.

This gives us a very simple way of implementing the numerical simulation of the wave-function's evolution. However, when looking to perform this calculation there is a problem in the representation of the evolution operator. The kinetic and potential operators do not commute. However, since we are considering a small time interval for our evolution operator we can utilise the Trotter-Suzuki factorisation. This allows us to expand the evolution operator into a product of two exponential operators with a correction in time which we can consider as negligible:

$$\begin{aligned}\hat{U}(t) &= e^{-\frac{i}{\hbar}\delta t\cdot(\hat{T}+\hat{V})}\\ &\approx e^{-\frac{i}{\hbar}\delta t\cdot\hat{T}}e^{-\frac{i}{\hbar}\delta t\cdot\hat{V}}e^{O(\delta t^2)}\\ &\approx= e^{-\frac{i}{\hbar}\delta t\cdot\frac{\hat{V}}{2}}e^{-\frac{i}{\hbar}\delta t\cdot\hat{T}}e^{-\frac{i}{\hbar}\delta t\cdot\frac{\hat{V}}{2}}e^{O(\delta t^3)},\end{aligned} \tag{6.4}$$

where the expansion of the exponential leads to a error of order $O(\delta t^2)$ for each intermediate time step and can be lowered further to $O(\delta t^3)$ by expanding the potential operator into two halves. Now $\hat{U}$ is the product of three unitary operators and the norm of the wave-function will be conserved throughout the evolution.

As the potential $\hat{V} = \hat{V}(\hat{\boldsymbol{r}})$ is a scalar function with the two-dimensional position coordinates $\boldsymbol{r} = (x, y)$. In real space, the application of this operator to the wave-function is trivial. However, when it comes to the kinetic operator $\hat{T} = \hat{T}(\hat{\boldsymbol{r}}, \hat{\boldsymbol{p}})$, the exponential is difficult to calculate as it is a non-local operator. The representation in real space is computationally inefficient due to the second derivative. Therefore, the kinetic operator must be transformed into Fourier space such that:

$$\hat{T} = \frac{\hbar^2 k^2}{2m^*} \tag{6.5}$$

Which allows for much simpler calculations as in this form it is a scalar function. To move between the real and Fourier space we use series of direct and inverse Fourier transforms. By doing so we split each time step into two representations of space in a technique knows as the Fourier Split-Step Method (FFSM). For these calculations we have assumed periodic boundary conditions. This expands our evolution operator to become

$$\hat{U}(\delta t) = e^{-\frac{i}{\hbar}\delta t \cdot \frac{\hat{V}}{2}} \mathcal{F}^{-1} e^{-\frac{i}{\hbar}\delta t \cdot \hat{T}} \mathcal{F} e^{-\frac{i}{\hbar}\delta t \cdot \frac{\hat{V}}{2}}. \tag{6.6}$$

Within this operator we have performed a sequence of direct and inverse Fourier transforms such that

$$\hat{T}\Psi(x,y) = \mathcal{F}^{-1}\hat{T}(\hat{p}_x,\hat{p}_y)\tilde{\Psi}(p_x,p_y) = \mathcal{F}^{-1}T(\hbar k_x,\hbar k_y)\mathcal{F}\Psi(x,y), \tag{6.7}$$

where

$$\mathcal{F}\Psi(x,y) = \frac{1}{2\pi\hbar}\int_{-\infty}^{+\infty} e^{-\frac{i}{\hbar}\mathbf{p}\cdot\mathbf{r}}\Psi(x,y)\mathrm{d}\mathbf{r} = \tilde{\Psi}(\hbar k_x,\hbar k_y), \tag{6.8}$$

given that $\mathbf{p} = \hbar\mathbf{k}$.

Finally, with the application of the FSSM, we find our solution to be:

$$\Psi(\boldsymbol{r},t) = \left(e^{-\frac{i}{\hbar}\delta t \cdot \frac{\hat{V}}{2}} \mathcal{F}^{-1} e^{-\frac{i}{\hbar}\delta t \cdot \hat{T}} \mathcal{F} e^{-\frac{i}{\hbar}\delta t \cdot \frac{\hat{V}}{2}}\right)^N \Psi(\boldsymbol{r},0), \tag{6.9}$$

where we have applied a time loop of N applications such that the total time is $t = N \times \delta t$.

As we are working under quantum Hall conditions the magnetic field must be taken into account. We now consider $\boldsymbol{B} = \nabla \times \boldsymbol{A}$ in the Hamiltonian where $\boldsymbol{A}$ is a vector potential. Represented in real space, the canonical momentum in the kinetic term is replaced with a kinetic momentum $\boldsymbol{p} - q\boldsymbol{A}$ and as the magnetic field is considered uniform we use the Landau Gauge and therefore our kinetic term as now transformed into:

$$\begin{aligned} \hat{T} &= \frac{1}{2m^*}\sum_{i=x,y,z}(p_i - qA_i)^2 \\ &= \hat{T}_{p_y,x}(\hat{x},\hat{p}_y) + \hat{T}_{p_x,y}(\hat{y},\hat{p}_x) \end{aligned} \tag{6.10}$$

for a 2D system. This now requires the application of the FSSM for both $\hat{p}_x$ and $\hat{p}_y$ applied separately for each coordinate. The final wave-function for a 2D system with magnetic field effects is given as:

$$\Psi(\boldsymbol{r},t) = e^{+\frac{i}{\hbar}\delta t \cdot \frac{\hat{V}}{2}}\left(e^{-\frac{i}{\hbar}\delta t \cdot \hat{V}} \mathcal{F}_y^{-1} e^{-\frac{i}{\hbar}\delta t \cdot \hat{T}_{p_y,x}} \mathcal{F}_y \mathcal{F}_x^{-1} e^{-\frac{i}{\hbar}\delta t \cdot \hat{T}_{p_x,y}} \mathcal{F}_x\right) e^{-\frac{i}{\hbar}\delta t \cdot \frac{\hat{V}}{2}}\Psi(\boldsymbol{r},0) \tag{6.11}$$

The movement of the potential operators outside of the N time loop allow for parallel coding of the this simulation, as these half time-steps of the potential operator performed on the initial state can be done at the same time as the time loop [72].

6.1.1 Discretisation procedures and convergence

A feature of this simulation is the use of a discretised space to perform the calculations of the wave packets evolution throughout the domain. More specifically, a 2D grid is discretised by $N_x \times N_y$ points in a domain bounded by dimensions L_x and L_y. In turn, the grid spacing is given as

$$\delta x = \frac{L_x}{N_x} \tag{6.12}$$

$$\delta y = \frac{L_y}{N_y} \tag{6.13}$$

which causes a discretisation in the corresponding reciprocal space. This boundary we have applied to our system we are simulating imposes a boundary over the maximum wave vector allowed such that

$$\delta k_x = \frac{2}{L_x}, \tag{6.14}$$

$$k_x^{\max} = -k_x^{\min} = \frac{\pi}{\delta x}, \tag{6.15}$$

which holds true for the k_y axis too.

Incorporating the magnetic field and using the Landau gauge gives rise to an important feature as it induces a coupling among the x and k_y dimensions which is stated as

$$k_y = -\frac{eBx}{\hbar} \tag{6.16}$$

associating each point in the x axis to a point in a certain wave vector. Additionally, placing the wave vector in the centre of the domain finds a maximum wave vector:

$$\tilde{k}_y^{\max} = \frac{eBL_x}{2\hbar}. \tag{6.17}$$

To avoid the wave function reaching a region of space they can not be properly represented in the restriction that $\tilde{k}_y^{\max} < k_y^{\max}$ is imposed. Other restriction imposed are the step sizes between the discretised points, in both dimensions δx and δy, must be smaller than the magnetic wavelength $l_B = \sqrt{\hbar c/eB}$, the smallest size of a circular orbit of the electron in a magnetic field which is allowed by the uncertainty principle. In this thesis we use magnetic fields ranging from $B = 5\,\mathrm{T}$ and $B = 11\,\mathrm{T}$ which results $l_B \approx 11.2\,\mathrm{nm}$ and $l_B \approx 7.5\,\mathrm{nm}$ respectively.

A fundamental requirement of the Fourier Split-Step method is that the grid spacings δx, δy and the time interval δt have certain prerequisites. We have already stated that δt must be small enough such that the Hamiltonian does not change over this distance but we now require it to be small compared to the transition period between grid points i.e. $\delta x / v_x^{\max}$ where $v_x^{\max}$ is the maximum phase velocity (even if $\hat{H}$ is time independent).

The product $\hbar^{-1}\delta t \cdot V$ with the V component of the time evolution operator must be small enough when compared with the period of the exponential such that

$$\delta t \ll \frac{2\pi\hbar}{\max V}. \tag{6.18}$$

The same must also hold true for the kinetic energy component. A requirement of the simulation relies on the grid spacing δx being small enough when being compared to variations of the wave functions along x. This can also be described by the requirement that the maximum wave vector in Fourier space must be able to describe the highest momentum component of the wave function. Equation 6.17 shows that it is directly proportional the the magnetic field strength. Therefore, as we will be using these numerical simulations for higher magnetic fields required by HEQO devices, will required a much smaller grid spacing. We will see later on how this will affect our simulations.

6.1.2 Wave function

To model how an electron will evolve in a system, we model it as a Gaussian wave packet. The reason for this is that the hot-electrons in the experiments are observed to have a Gaussian distribution, although it is not entirely clear whether this is a true observation of the wave packet or if it is influenced by the detector profile [74, 75]. In any case, we stick with Gaussian wave packets, although there is no restrictions, at least in the transport direction, to the type of wave function profiles which can be used e.g. Lorentzian wave packets can represent levitons [37, 24, 39]. Theoretical work proposes that injected electrons can be modelled as Gaussian wave packets[76].

Sharp barriers are used in order to observe the wave function shape and the local band structure. The confining potential is a smooth Fermi barrier given by

$$V(x) = \frac{V_0}{1 + \exp\left(\frac{x - x_b}{\lambda}\right)} \tag{6.19}$$

where V_0 is the maximum potential, x_b is the x position of the barrier, and λ is a broadening parameter. A Gaussian wave packet travelling in the y direction in a potential $V(x)$ translationally invariant in the y direction. For an initial position y_0 and a standard deviation σ we state

$$\psi(y) = \frac{1}{\sqrt[4]{2\pi\omega^2}} e^{-\frac{(y-y_0)^2}{4\sigma^2}} e^{iky_0} = \frac{1}{\sqrt{2\pi}} \int \mathrm{d}k e^{iky} F(k) \tag{6.20}$$

given that $F(k)$ is the weight of each plane wave which is the Fourier transform of the Gaussian wave packet such that

$$F(k) = \frac{1}{\sqrt{2\pi}} \int \mathrm{d}y e^{-iky} \psi(y) = \sqrt[4]{\frac{s\sigma^2}{\pi}} e^{-\sigma^2(k-k_0)^2} e^{-iky_0} \tag{6.21}$$

which is referred to as the Gaussian weight. Combining a group of edge states with the Gaussian weights results in the wave function that becomes localised in the y direction (given that the edge states are plane waves in the y direction). In turn, the edge states are also localised in the x direction which results in the wave function being localised in x as well. The final expression for the wave function is then

$$\Psi(x,y) = \frac{1}{\sqrt{2\pi}} \sum_n \int \mathrm{d}k F_n(k) e^{iky} \varphi_n(x,k) \tag{6.22}$$

with the addition of the dependence of the quantum number n for the Gaussian weight. For our simulations we focus on edge states that are found only in the lowest Landau level.

The wave function $\varphi_n(x,k)$ are unable to be represented analytically. However, if we use the assumption that x_0 is sufficiently far from our Fermi barrier we can combine the edge states and express the wave function analytically. Analytically integrating Eq. (6.22) gives

$$\begin{aligned} \Psi(x,y) &= N \int \mathrm{d}k F(k) e^{iky} \chi_1(x,k) && (6.23) \\ &= N \int \mathrm{d}k e^{iky} \sqrt[4]{\frac{2\sigma^2}{\pi}} e^{-\sigma^2(k-k_0)^2} e^{-iky_0} \frac{1}{\sqrt[4]{\pi l_B^2}} e^{-\frac{(x-x_0(k))^2}{2l_B^2}} && (6.24) \end{aligned}$$

where χ_1 is the eigenfunction of φ_1 and we find that

$$\Psi(x,y) = \frac{1}{\pi} \frac{\sqrt[4]{\frac{2\sigma^2}{l_B^2}}}{\sqrt{2\sigma^2 + l_B^2}} e^{-k_0\sigma^2} e^{-\frac{x^2}{2l_B^2}} e^{\frac{\left(\mathrm{sgn}(B)x - i(y-y_0) - 2k_0\sigma^2\right)^2}{2(2\sigma^2+l_B^2)}} \tag{6.25}$$

which is represented as

$$\begin{aligned}\mathit{\Psi}(x,y) = N\text{exp}\left[-\frac{2\sigma^2(x+\frac{\hbar k_0}{eB})^2}{2l_B^2(l+B^2+2\sigma^2)}\right] \times \exp\left[-\frac{(y-y_0)^2}{2(l_B^2+2\sigma^2)}\right] \\ \exp\left[i(y-y_0)\frac{k_0 2\sigma^2 - x\text{sgn}(B)}{l_B^2+2\sigma^2}\right]\end{aligned} \tag{6.26}$$

in a localised state. From this state we can attribute the spreading of the Gaussian probability where standard deviation denotes in the x-direction

$$\sigma_x^2 = \frac{1}{2}l_B^2\left(1+\frac{l_B^2}{2\sigma^2}\right) \tag{6.27}$$

and the y-direction

$$\sigma_y = \sigma^2\left(1+\frac{l_B^2}{2\sigma^2}\right). \tag{6.28}$$

For the rest of this thesis a value of $\sigma = 60\,\text{nm}$ will be used to calculate σ_x and σ_y. This value is used as it is a good compromise for the simulations such that the wave packets are small enough to be localized inside the device we are modelling and at the same time their time spreading is small enough to keep this condition true during the total simulation time.

6.2 Time-evolution of edge state wave packets

In order to approximate the time evolution of the wave packet from Eq. (6.22) we must consider a standard deviation σ that is sufficiently high such that the region of states $|k\rangle$ which are being combined are limited in the reciprocal space. As such we can locally approximate the energy band in this region with a parabola. It also means we can assume all eigenfunctions that are combined have approximately the same shape and centre $x_0(k_0)$ such that

$$\varphi_1(x,k) = \varphi_1(x,k_0) \tag{6.29}$$

for all values of k. In this case Eq. (6.22) becomes

$$\begin{aligned}\mathit{\Psi}(x,y) &\approx \frac{1}{\sqrt{2\pi}}\int \mathrm{d}k \sqrt[4]{\frac{2\sigma^2}{\pi}} e^{-\sigma^2(k-k_0)^2} e^{-iky_0} e^{iky} \varphi_1(x,k_0) \\ &= \frac{e^{-\frac{(y-y-0)^2}{4\sigma^2}} e^{ik_0 y}}{\sqrt[4]{2\pi\sigma^2}} \varphi_1(x,k_0)\end{aligned} \tag{6.30}$$

The main difference between the Gaussian wave function of Eq. (6.22) and what we define as the edge state wave packet of Eq. (6.30) is that the periodicity and interference phenomena of the Gaussian wave packet are governed by the wave vector k_0 and the edge state wave packet is characterised by k_0 which itself is not a physical quantity. A new value x_0 for the centre of the well eigenfunctions is needed when performing a translation along the x-axis. Although this does not change the physics of the problem, it does change the value of $k_0 = k_0(x_0)$. Therefore, this parameter cannot be a physical quantity which governs the periodicity of the edge state wave packet [73].

To factor in the time evolution of the wave function we can identify the effect it will have on the x and y components. For the x direction, the wave function will not show change in shape due to the confinement and that we have calculated it for the ground state. However, we have free motion in the y direction governed also by confining potential. For a 1D edge channel, an analytic solution can be found as

$$\Psi(x,y,t) = e^{-\frac{i}{\hbar}t\hat{H}_L}\Psi(x,y). \tag{6.31}$$

Assuming that Eq. (6.30) is a linear combination of eigenstates of $\hat{H}_L$ this is expanded to

$$\Psi(x,y,t) = \frac{1}{\sqrt{2\pi}}\int \mathrm{d}k \sqrt[4]{\frac{2\sigma^2}{\pi}} e^{-\sigma^2(k-k_0)^2} e^{ik(y-y_0)} \varphi_1(x,k_0) e^{-\frac{i}{\hbar}tE_1(k)}. \tag{6.32}$$

If we are assuming a high standard deviation, we can locally approximate the energy band in this region with a parable

$$E_{1,k} = E_1(k) \approx ak^2 + bk + c = a(k-k_1) + c', \tag{6.33}$$

$$b = -2ak_1, \tag{6.34}$$

$$c = ak_1^2 + c'. \tag{6.35}$$

Expanding the integral we get a wave function

$$\Psi(x,y,t) = \varphi_1(x,k_0)\frac{\exp[i(ct/\hbar)] \times \exp\left[\frac{(y-y_0+2ik_0\sigma^2+\frac{bt}{\hbar})^2}{4(i\frac{a}{\hbar}t+\sigma^2)}\right] \times \exp[-k_0^2\sigma^2]}{\sqrt[4]{\frac{2\pi}{\sigma^2}}\sqrt{\sigma^2 + i\frac{at}{\hbar}}}. \tag{6.36}$$

which describes a Gaussian wave packet travelling in the y direction. The physical parameter a describes how the wave packet spreads and for GaAs it is given as $a = 5.7 \times 10^{-10}\,\mathrm{eVm}^2$. Figure. 6.1a shows the potential described by Eq. (6.19) where there is a sharp Fermi distribution for a large potential energy. Figure 6.1b shows a wave packet

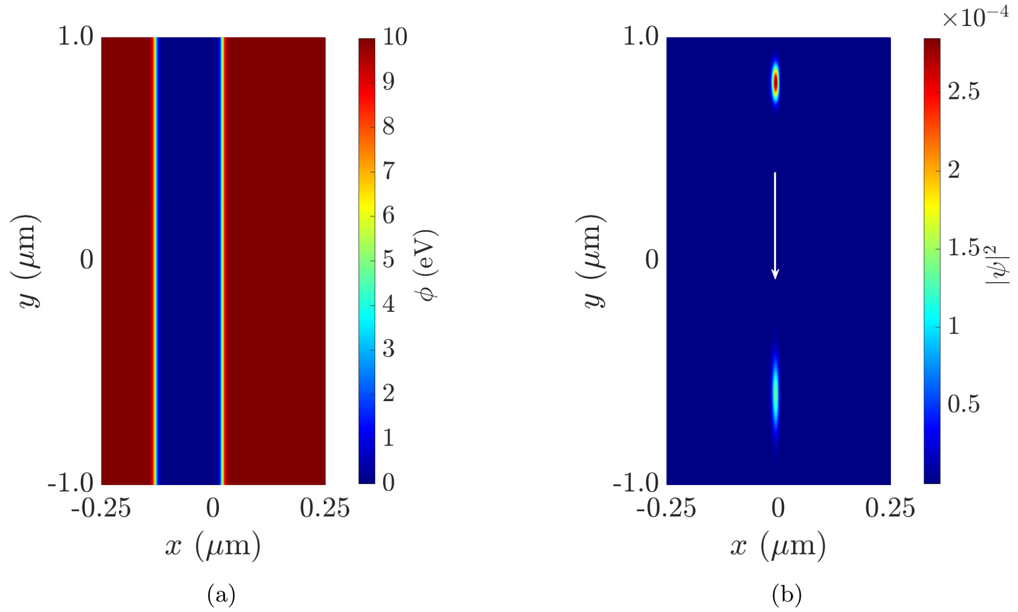

(a) (b)

Figure 6.1: (a) The potential which is based on a Fermi distribution given in Eq. (6.19).(b) Numerical simulation performed on an initialised Gaussian wave packet (top) and evolved in time to its final position (bottom) in the potential shown in (a). A value of $B = 5\,\mathrm{T}$ has been used in this numerical simulation.

initialised in the potential. After performing the numerical simulations on how the wave packet will evolve in the system the final wave packet (bottom of the figure) has been stretched in the direction of travel y. This is consistent with the standard deviation of the approximate wave packet in Eq. (6.36)

$$\sigma^2(t) = \left(\sigma^2 + \frac{a^2t^2}{\sigma^2\hbar^2}\right). \tag{6.37}$$

6.3 Gauge transformation

A limitation to this numerical calculation is the restriction imposed by the discretisation procedures. As we are using the Fourier split-step method which has prerequisites on the interval spacing in the discretised grid, this spacing requirement gets much smaller for larger magnetic fields. This can be seen from the magnetic field dependence on the maximum wave vector in Eq. (6.17). Because of this, simulations of devices such as the TOF experiment (see chapter 5) with domain sizes of 5 μm × 5 μm, for example, pose a challenge. A solution to overcome this is by implementing a gauge transformation. This allows us to change the coordinates of the system, i.e. shift the frame of view we are simulating to a new location and continue the simulation without changing the physical description of he system.

As we are changing the entire potential of the system we are changing the gauge, **A**, that these potentials are represented in. To transform the gauge we use the equation:

$$\mathbf{A}'(x', y') = \mathbf{A}(x, y) + \nabla \Lambda(x, y) \tag{6.38}$$

where Λ is an arbitrary scalar function. As our change in the coordinate system is just a translational shift in the x and y direction we can equate this to:

$$x' = x + x_s \;\; \& \;\; y' = y + y_s \tag{6.39}$$

where $x_s = y_s = 500$ nm. Taking the Landau gauge to be $\mathbf{A} = (-By, 0, 0)$, with the transformed coordinates it becomes $\mathbf{A} = (-B(y + y_s), 0, 0)$. We want our transformed gauge to be the exact same in the new coordinate system, i.e. $\mathbf{A}' = (-By', 0, 0)$. Equation 6.38 then implies that:

$$\begin{aligned} \nabla \Lambda &= (+By_s, 0, 0) \\ \implies \Lambda &= (+By_s x', a, b) \end{aligned} \tag{6.40}$$

where a and b are constants but we can assume $a = b = 0$. To then apply this transformed gauge to the new wave fucntion $\Psi'(x', y')$ we use the equation:

$$\Psi' = e^{\frac{iq\Lambda}{\hbar}} \Psi \tag{6.41}$$

where $q = -e$. We will show how to implement this in the next chapter.

6.4 Measuring the wave packet

A characteristic we want to measure with these simulations is the dispersion rate of the wave packet, as we know that over time the probability distribution of the electron will spread. Although this problem may seem trivial, it begins to get more complicated when the wave packet is travelling along complex patternings enforced by the depletion gates and etching. What limits do we take to ensure that the length of two wave packets are consistent and accurate? Where do we take the measurement? We show in this section our method which we will use to analyse simulations of realistic devices.

The wave packets we model the electrons on have a Gaussian (or normal) distribution

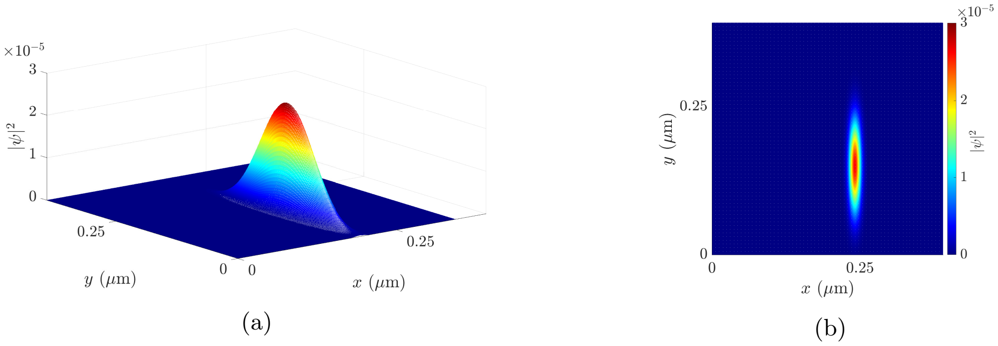

Figure 6.2: A Gaussian wave packet initialised by the numerical simulations outlined in this chapter. (a) Shows a three-dimensional view of the wave packet to show that there is a "spine" of maximum points through the centre. (b) shows a top down view

with a general formula in two-dimensions given as:

$$f(x,y) = A\text{exp}\left[-\frac{1}{2}\left(\frac{x-x_0}{\sigma_x}\right)^2 - \frac{1}{2}\left(\frac{y-y_0}{\sigma_y}\right)^2\right] \tag{6.42}$$

centred around the points x_0 and y_0 with the spread associated by the standard deviation σ in each respective dimension. The Gaussian function in Eq. (6.42) is a peaked function in both x and y which means that there are maximum points within the function that we can easily identify and these maximum points are found at the centre.

To model an electron as a Gaussian wave packet, we give an initial spread which is longer in the direction of travel than in direction of confinement. For example, an electron travelling in the y direction with a confining potential $U(x)$ will be initialised as shown in Fig. 6.2. In particular, we give a three-dimensional representation in Fig. 6.2a which shows the outline of the "spine" of the Gaussian wave packet where we find the maximum points of $|\psi|^2$ in x and y dimensions. The width in the x dimension is shown in more detail in Fig. 6.2b.

Our method involves finding the centre of the Gaussian wave packet which numerically is found by finding the maximum value of $|\psi|^2$ in both the x and y direction. These two values then gives us the coordinates x_0 and y_0 for the centre of the wave packet. We then draw a circle, centred on (x_0, y_0) with an initial radius, which for this case is 50 nm but can be changed depending on the size of the system in question. Within this circle we calculate $\sum |\psi|^2$ to find out how much of $|\psi|^2$ is found in this region. If the value is less than 99% of the total sum then the circle is expanded by a given amount and the calculation performed again. This step is repeated until we get a circle which encompasses 99% of the wave packet. This step is important for making sure that we have consistency

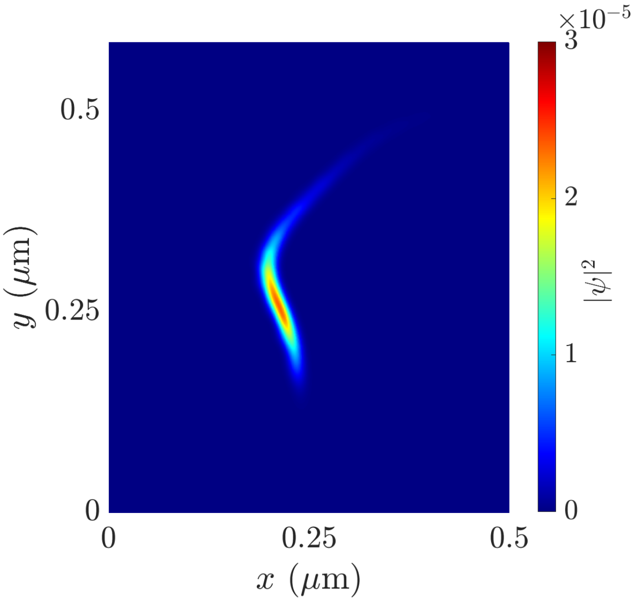

Figure 6.3: An example of a wave packet which has travelled around a curved edge states patterned by a depletion gate and etching. The wave packet has dispersed along the path it is travelling and is measured to be a length of 346.54 nm when the initialised wave packet was 260 nm.

in place for all measurements. The next step involves finding all the maximum value of $|\psi|^2$ for each line of discretised points in the x and y directions within the circle, which outlines the "spine" of the wave packet. Then it is just the case of adding the distance between each point to find the total length.

In the case of Fig. 6.2, this method is trivial and could probably be done by eye. However, because this is an initialised wave packet in the simulation with a known length we can compare the accuracy of our method. Using our method, a length of 259.62 nm was calculated, whereas the input value was 260 nm. This wave packet is initialised in a potential where it is translationally invariant in the y direction and gives us a perfect, unperturbed model to test our measuring method. It is also initialised a short distance away from this point to reduce the natural dispersion. However, this is not the case for every point in time when simulating around a realistic device. Fig. 6.3 shows a more complex wave packet travelling around a more interesting, patterned edge channel. In this case, you can see in the figure that the bulk of the wave packet, and the maximum values, are not centred directly in the middle but rather offset. However, our main aim is to keep consistency in our method for all calculations in order to obtain accurate results.

Chapter 7

Time-of-flight simulation

In the previous chapter we outlined the numerical method for simulating an electron, modelled as a Gaussian wave packet, in a system with a potential energy. We now apply this simulation to a HEQO device, where we have calculated a realistic device potential using the projected surface method which we discussed in detail in chapter 4. We introduced the TOF experiment in chapter 5, showing that through the use of a deflection gate we can inject electrons into two paths of known length. By injecting an electron into each path, the difference in time it takes to travel each path allows for a time resolved method of calculating the velocity. Here, we wish to simulate this experiment to understand the transport of the hot electron between injection and detection.

7.1 Electrostatic model

The model of the TOF experiment was found to have a long path with a distance of $\approx 12\,\mu$m. This was the exact distance calculated that an electron injected at a given energy would travel within our model. Due to the limitations of the simulation at high magnetic field (which was discussedin chapter 6), we are unable to simulate the entire device within one simulated domain. This, in combination with the FSSM working more efficiently in discretised grids of 2^n, we are limited to a grid size of 4096 $\times$ 4096 due to computational cost. At magnetic fields of $B = 11\,\mathrm{T}$, this grid size will allow us to simulate frames which have a domain size of 1 μm $\times$1 μm. To overcome this problem, we employ the use of gauge transformations. By taking a frame of domain size 1 μm $\times$1 μm from the full potential, we can simulate how a hot electron will evolve in this small part of our system. When the wave packet gets close to the boundary of each frames domain, we can shift our frame and perform a gauge transformation. This step will be performed multiple times following the full experiment while focussing on only the edge channel these hot electrons will travel along.

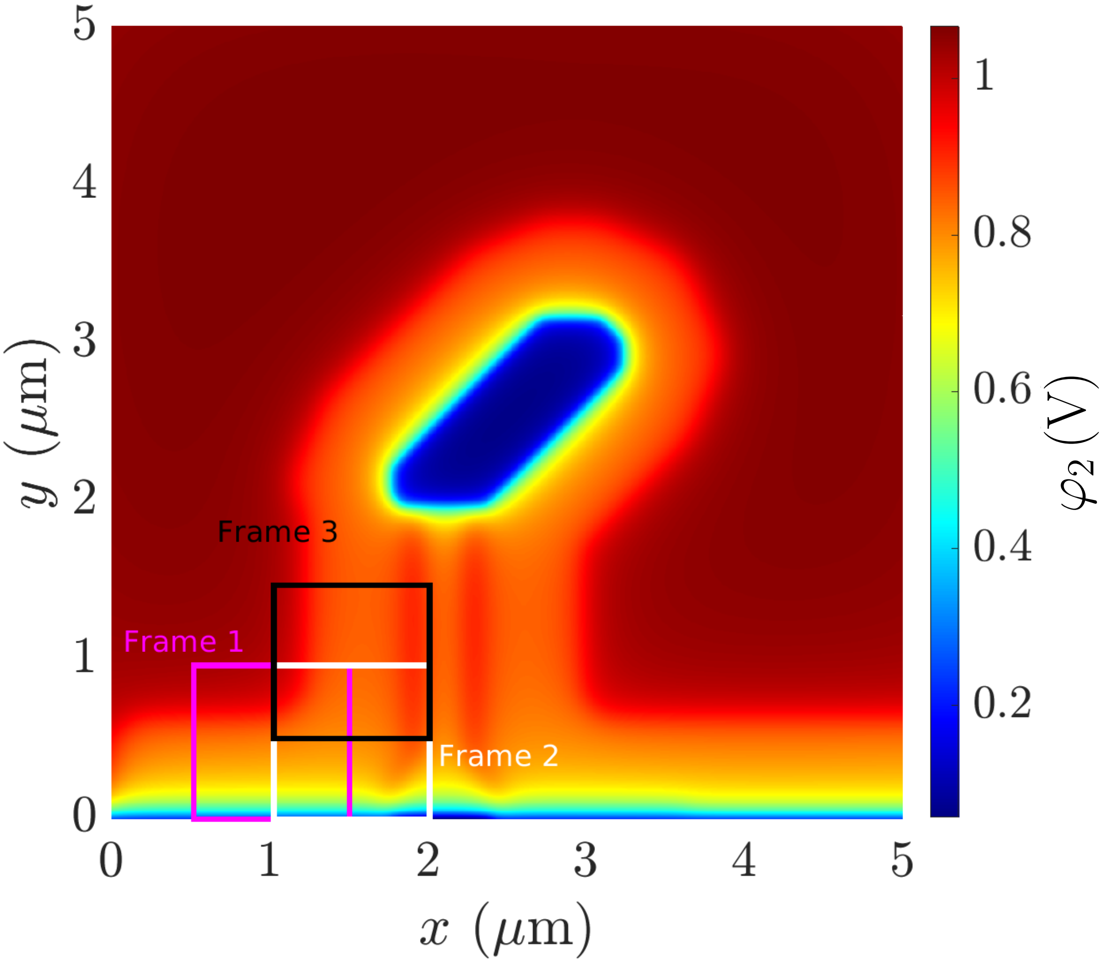

Figure 7.1: The electrostatic potential calculated using the PSM for the TOF experiment. The model has been altered such that the distance of the long path has been shortened. Three exemplary frames are given to represent the frames, each with a 1 μm × 1 μm domain, used in the simulations. The initial frame 1 (pink) is shifted in the x direction by $\Delta x = 0.5\,\mu$m to frame 2 (white). Frame 2 is then shifted in the y direction by $\Delta y = 0.5\,\mu$m to frame 3 (black). This shift is performed the entire way around the long path, where each frame will overlap by $0.5\,\mu$m to allow for the gauge transformation of the wave packet to each frame.

In an effort to reduce the number of frames, we reduce the size of TOF model we have used previously. Figure. 7.1 shows the electrostatic potential of the TOF device we will be performing our dynamic simulations on. The only difference from the model shown previously is the length of the long arm has reduced, without affecting any of the important features such as the radius of curvature at the top of the device or the region around the deflection gate. On the figure is an example of the first three frames we will be performing our simulations in. We start at frame 1 and perform shifts of $0.5\,\mu$m in

Gauge Transformations of TOF Model (Long Path)		
Frame Number	$\mathit{\Delta} x$ (μm)	$\mathit{\Delta} y$ (μm)
Frame 1	-	-
Frame 2	+0.5	-
Frame 3	-	+0.5
Frame 4	+0.5	
Frame 5	-	+0.5
Frame 6	+0.5	+0.5
Frame 7	+0.5	-
Frame 8	-	-0.5
Frame 9	-0.5	-0.5
Frame 10	-	-0.5
Frame 11	-	-0.5
Frame 12	+0.5	-

Table 7.1: A table showing the shifts in the x and y axis from one frame to another, following the path the electron would take when deflected off the deflection gate into the depletion gate, known as the long path. The first three frames are shown in Fig 7.1.

either the x direction, y direction, or both. This shift in position allows for easier and consistent transformations between each frame. These frames are continued through the entirety of the depletion gate, with a total of twelve frames needed to simulate the long path. Table 7.1 shows the shift in x and y directions between the frame and the previous frame. The same is also done for the short path, however this is much more simple where the shift only occurs in the x direction totalling four frames needed each with a shift $\mathit{\Delta} x = 0.5\,\mu$m.

7.2 Dynamic simulations

For these simulations we calculate, using the projected surface method, the electrostatic potential for a TOF experiment with a depletion gate voltage of $V_g = -0.25\,\mathrm{V}$. For the long path, a voltage of $V_d = -0.50\,\mathrm{V}$ is applied to the deflection gate, while for the short path a voltage of $V_d = -0.30\,\mathrm{V}$ is applied. For both sets of simulations, the Gaussian wave packet is initialised at the same energy. A magnetic field strength of $B = 11\,\mathrm{T}$ is used. The figures in this section will show the probability distribution $|\psi|^2$ of the wave packets. The frames will show two or three wave packets each, with arrows showing the direction of motion. Where three wave packets are shown, the time steps δt between each point in the evolution is equal, unless otherwise stated.

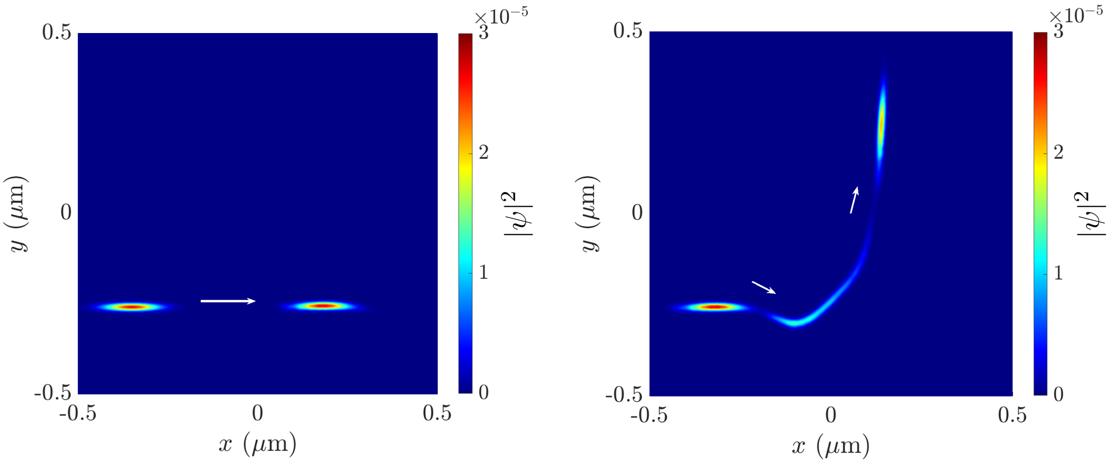

(a) Frame 1

(b) Frame 2

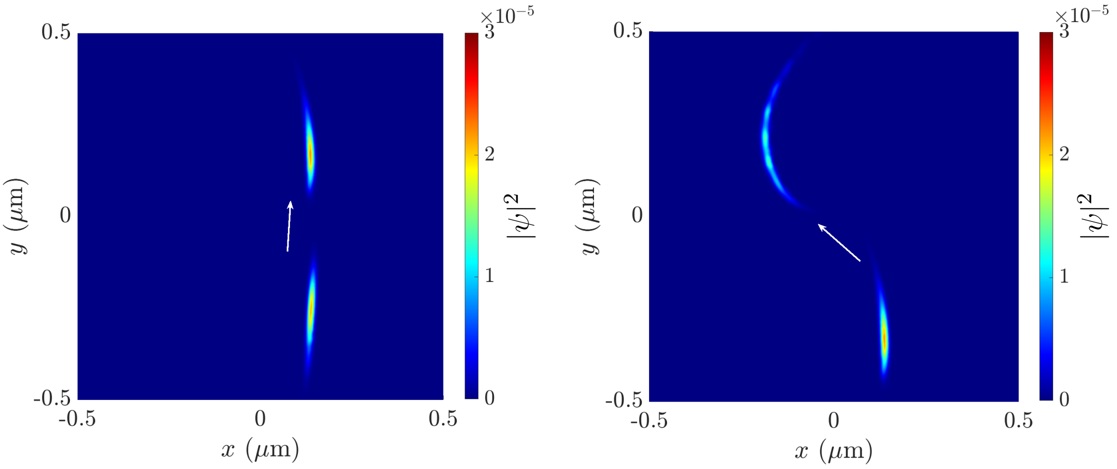

(c) Frame 3

(d) Frame 4

Figure 7.2: The first four frames within which the Gaussian wave packet evolves in time (a) before , (b) & (c) during, and (d) after the interaction with the deflection gate of the TOF experiment. The voltage applied to the depletion gate is $V_g = -0.25\,\mathrm{V}$ and the voltage applied to the deflection gate is $V_d = -0.50\,\mathrm{V}$. The arrows in each figure show the direction of travel and the last wave packet in each frame is the initial wave packet of the next frame.

7.2.1 Long path

We first observe the twelve frames required to simulate the evolution of the Gaussian wave packet around the long path of the TOF experiment. For the following simulations we evolve each wave packet by $\delta t = 1\,\mathrm{fs}$ in time. Observations of these simulations will be made in comparison to Fig. 5.5 and Fig. 5.6 in order to compare the semi-classical calculations of velocity with the time resolved values we can obtain from the simulations.

Figure 7.2 Shows the first four frames of our simulation. This collection of simulations represent the initialised wave packet before (Fig.7.2a), during (Fig.7.2b & 7.2c), and after (Fig. 7.2d) the interaction with the deflection gate. Figure 7.2a is the only frame which will have the straightest confinement potential for our wave packet to travel along, as required to initialise the wave packet. From the results of chapter 5 we saw that semi-classically the velocity does not vary when the wave packet is travelling along a straight edge without any changes in its direction. In this frame we can calculate the centres of the left wave packet ($t = 0\,\mathrm{ps}$) and the right wave packet ($t = 12\,\mathrm{ps}$) to travel a distance $\mathit{\Delta} D = 536.62\,\mathrm{nm}$. Over this distance and time, the calculated velocity between these two wave packets is $v = 4.47 \times 10^4\,\mathrm{ms}^{-1}$. This value shows a good comparison with the semi-classical value at this point.

Figure 7.2b shows the right wave packet from Fig. 7.2a placed in the new frame 2 as the left wave packet, through a gauge transformation. The two wave packets which follow are represented with equal time gaps. Thus, the distance from the left to middle wave packet is much smaller than the distance between the middle and top, right wave packet. This observation is similar to the semi-classical case and from Fig. 7.2c we see the distance travelled between the centres of these wave packets is $\mathit{\Delta} D \approx 429.93\,\mathrm{nm}$ over a time of $t = 6\,\mathrm{ps}$ between them for a time resolved velocity of $v = 7.17 \times 10^4\,\mathrm{ms}^{-1}$.

From the semi-classical results, this region encompassed by these four frames showed large variations in the velocity, which we can observe and calculate with a time-resolved method with these simulations. However, an important feature we can study from this is the dispersion of the wave packet. When travelling along straight edges of the confinement potential, there is little variation in the length of the wave packet. However, when the wave packet enters a region in the path where the velocity decreases, either from the semi-classical figures or from these simulations, the wave packet begins to spread in the direction of travel. This is clearly seen in Fig. 7.2b & 7.2d.

Figure 7.3 shows the four frames of the simulation where the wave packet is travelling around the long arm of the TOF device. It is worth noting here that by frame 5, we have already used a gauge transformation four times and evolved the initialised wave packet over $N = 50,000$ times with a time step of $\mathit{\Delta} t = 1\,\mathrm{fs}$. The first wave packet at the bottom of Fig. 7.3a has spread to a length of 522.23 nm but has started to show sign of becoming more disordered. The Gaussian distribution of the wave packet has started to deteriorate, however, once it reaches the straighter edge it begins to become more organised and returns to its original length $\approx 240\,\mathrm{nm}$. As the wave packet approaches and travels around the curved potential in Fig. 7.3b & 7.3c respectively we can see the wave packet begin to bunch up. This is change in shape is prominent in Fig. 7.3d where the Gaussian distribu-

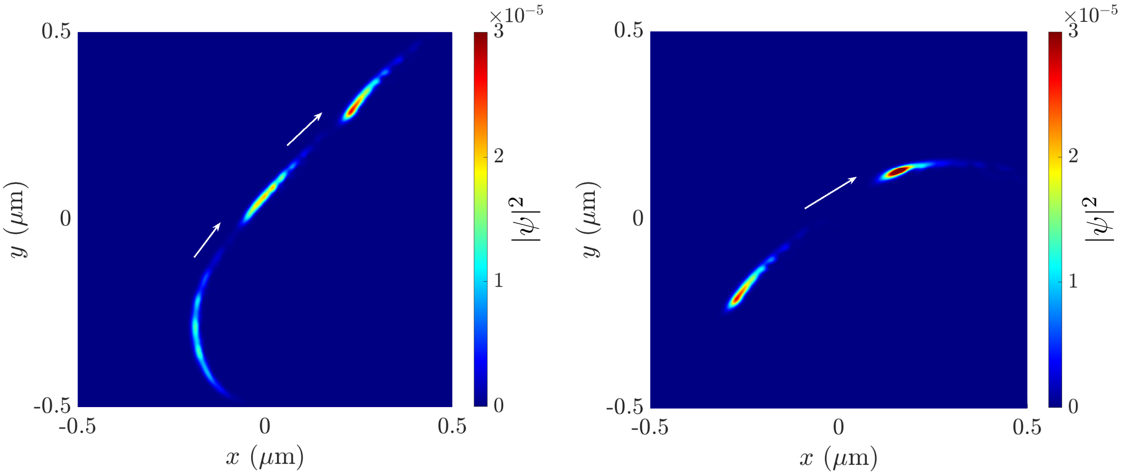

(a) Frame 5

(b) Frame 6

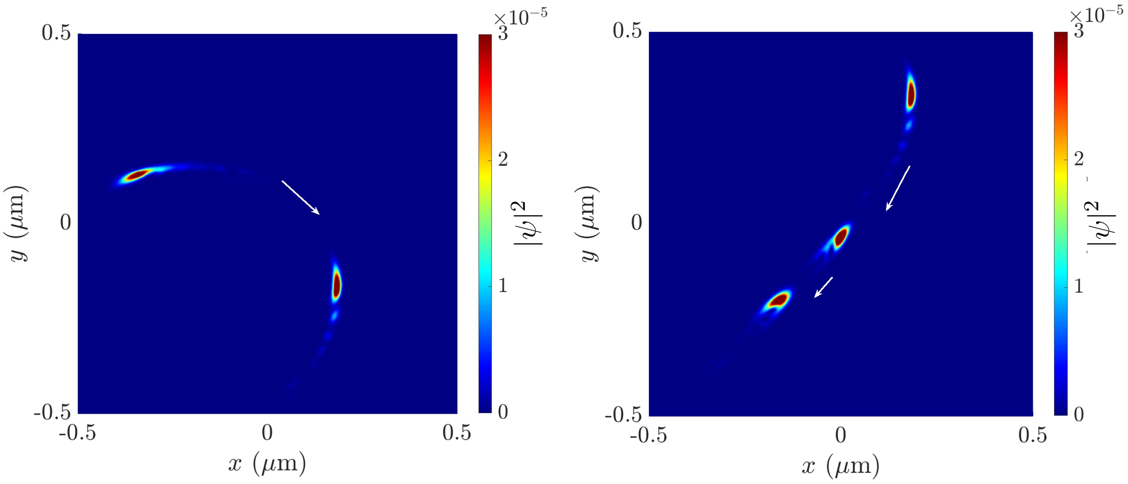

(c) Frame 7

(d) Frame 8

Figure 7.3: Four frames of Gaussian wave packets evolving in time around the long arm of the TOF device.

tion is no longer apparent and we notice a slow down in velocity between each of the first and second wave packet, and the second and third.

Figure 7.4 shows the re-approach of the wave packet towards the deflection gate. The final wave packet in Fig. 7.4a becomes more organised, resembling its original shape. As it travels back down parallel to the deflection gate in Fig. 7.4b, the shape becomes more circular. Note that in this figure, the wave packets represented are not spaced equally apart in time as the final two are closer together. Instead, the movement between top wave packet in the figure and the middle wave packet takes $t = 4\,\text{ps}$ while the middle and bottom wave packet takes $t = 2\,\text{ps}$. However, a calculation of the velocity $v = 7.28 \times 10^4$

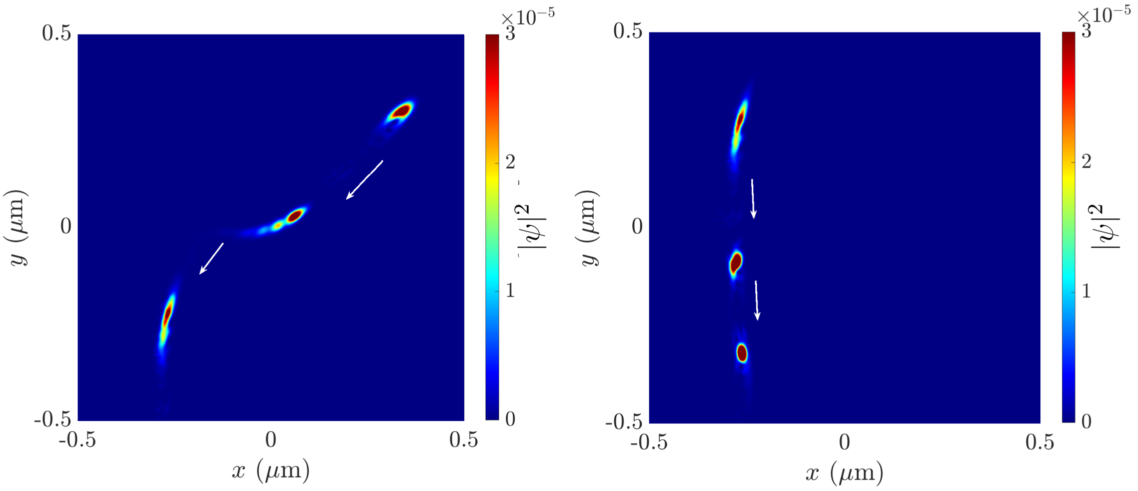

(a) Frame 9

(b) Frame 10

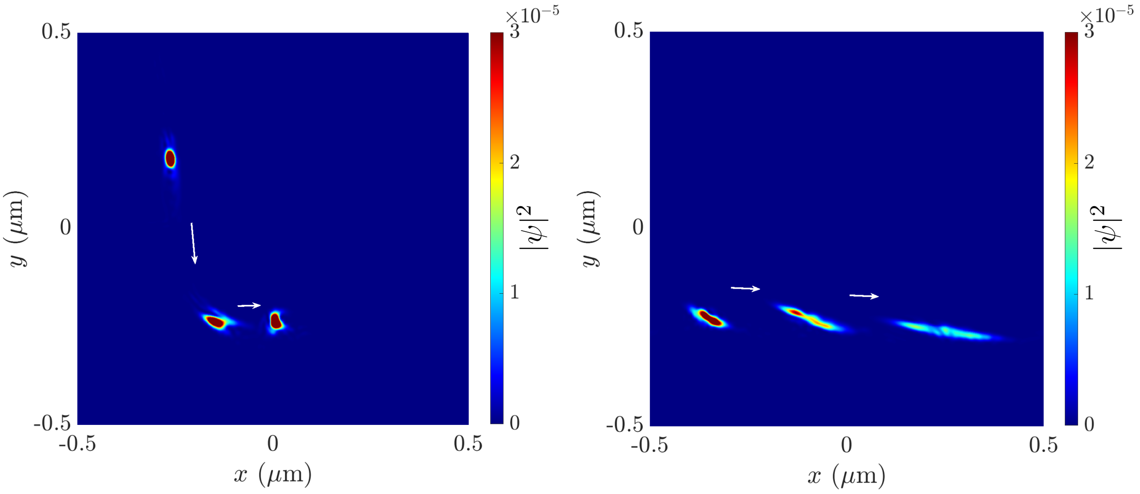

(c) Frame 11

(d) Frame 12

Figure 7.4: Four frames of the Gaussian wave packet evolving in time where it can be seen in (a) re-approaching the deflection gate, (b) & (C) travelling parallel to the deflection gate, and (d) travelling away along a straight edge of potential.

shows that it still similar to the opposite side of the deflection gate. The change in velocity is clearly seen in Fig 7.4c where the wave packets are now equally space in time.

7.2.2 Short path

We now continue to simulate the short path where the deflection gate voltage is $V_d = -0.30\,\mathrm{V}$. However, we note here that as there are significantly less frames, the following simulations have a time step of $\delta t = 0.5\,\mathrm{fs}$.

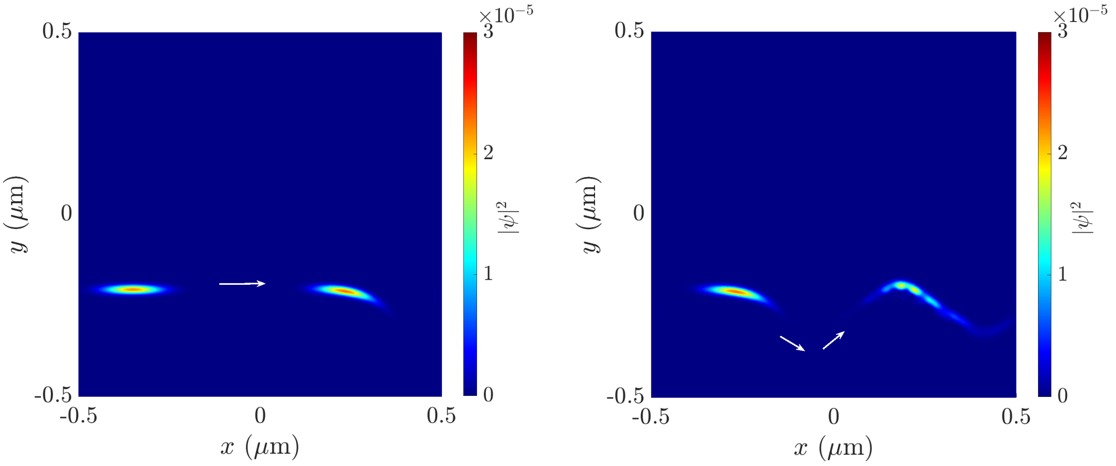

(a) Frame 1

(b) Frame 2

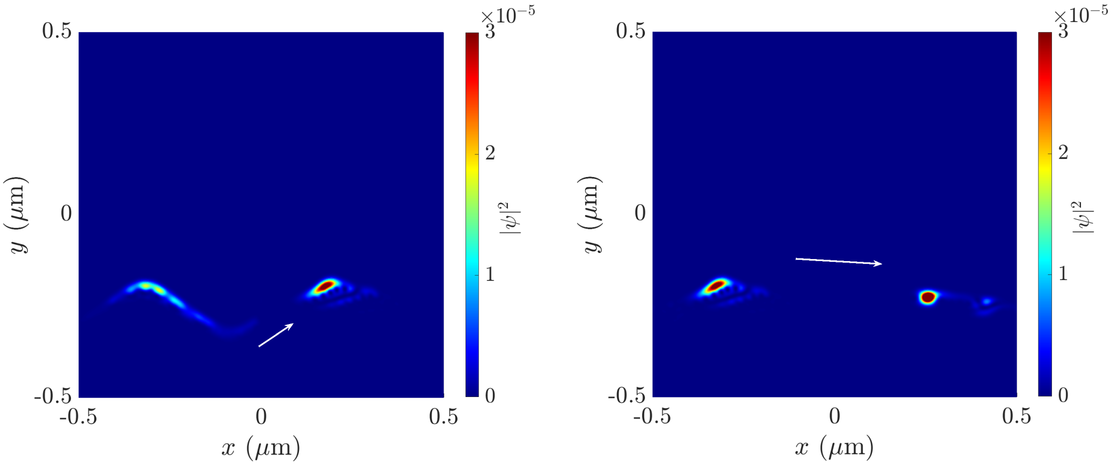

(c) Frame 3

(d) Frame 4

Figure 7.5: The short path of the TOF experiment where a voltage $V_d = -0.30\,\mathrm{V}$ is applied to the deflection gate.

Figure 7.5 shows the four frames used to simulate the wave packet along the short path of the TOF experiment. The initialised wave packet in Fig. 7.5a is the exact same as in the long path simulation. We see a similar motion of the wave packet as Fig. 7.2a, however the next frame in Fig. 7.5b continues to go through the region where the deflection gate occupies. Here, the path of the electron begins to bend down and back up. This is not represented in the figure as the wave packets would be too close together for a clear picture. But, the final wave packet in the frame has been stretched and the trail of its path can be seen behind it. This "zig-zag" path that the wave packet follows is also found in the next frame of Fig. 7.5c. Instead of the wave packet stretching due to this path, and as seen in the previous frames, it bunches up very quickly. In the final frame in Fig. 7.5d the final wave packet is now circular in shape. We saw similar behaviour in the same region of the long path (such as Fig. 7.4c), however the wave packet seemed to have restore itself but does not do so in this simulation.

In Fig. 7.5c we can see that the final wave packet of the frame shows a part of the wave packet has been "detached" from itself. What we are seeing here is the scattering of part of the wave packet into a higher Landau level. This scattering continues into Fig. 7.5d where the final wave packet has the separated portions reaching different points in the frame at the same time.

7.3 Discussion

We have shown in this chapter the use of a Gaussian wave packet evolving in time through an external potential which was calculated using the projected surface method for an altered TOF experiment. Prior to the simulations, we showed that the semi-classical analysis allowed us to calculate the instantaneous velocity of the electron at each point in its path and observe physical characteristics that were measured in the experiment. Here, we have taken this further by allowing us to analyse the experiment from a quantum point of view.

Firstly, with both the simulation of the long path and the short path, we an calculate the drift velocity of our Gaussian wave packet in the same time resolved method as the experiment. The long path travelled total distance of $8.8\,\mu$m for a total of 145 ps while the short path travelled $3.9\,\mu$m for a time of 75 ps. Independently we can calculate the drift velocity over each path as $v_d = 6.1 \times 10^4\,\mathrm{ms}^{-1}$ and $v_d = 5.2 \times 10^4\,\mathrm{ms}^{-1}$ for the long and short path respectively. The velocities are within the limit of the range of velocities calculated in our semi-classical analysis of the TOF model in the previous section. In those calculations, the average velocity for the short path was lower than in the long path. The difference in distance and time of flight between the two paths is $\Delta L = 4.9\,\mu$m an $\Delta\tau = 70\,$ps such that the drift velocity is $v_d = 7 \times 10^4$ ms^{-1}. This value of velocity is higher than the drift velocity calculated from the electrostatic potential calculated in the previous section. The calculation of the distance travelled by the wave packet in path relies on finding the position of its centre. This turned out to be a challenging task, as you can see in the figures of the simulation there were some distortions the shape of the wave packet. In addition to this, we only measured the position of the wave packet at intervals of 1 ps. Thus, for areas where there are large changes in the direction of the wave packets motion, like the zig-zag section of the short path, there are some discrepancies in the true distance travelled.

One of the first observations we can make with these experiments is the variations in the length (in the direction of travel) of the wave packet. We first observed a change in Fig. 7.2b where the wave packet is directed to travel parallel to the deflection gate. Initially, our wave packet begin with a length of 240 nm and as the direction of travel is changed by 90° it begins to spread to a length of 511.23 nm. After evolving further in time, we see that it reduces in length again, not to the initial length, but to 258.50 nm. This length is consistent in the continued frame in Fig. 7.2c and then the spreading occurs when in the frame of Fig. 7.2d. It seem that the dispersion of the wave packet correlates to the change in direction of motion.

Another characteristic that also changes with the change in motion is the instantaneous velocity which is in agreement with the semi-classical analysis of the trajectory as discussed in Chapter 5). Our first observation of this variation in velocity can be seen in Fig. 7.2b. The three wave packets are spaced evenly apart in time. The second (middle) wave packet moves a smaller distance than the difference in position between the second and third wave packet. However, this does depend on where you measure the distance as the second wave packet has dispersed to over double the original length. We continue to be consistent in our process by measuring the centre as the maximum point as we assume the Gaussian shape is kept. However, as the simulation progresses and the wave packet becomes more distorted (Fig. 7.4a for example), this measurement becomes increasingly more difficult and the accuracy of the measurement becomes weaker. In addition to this discrepancy in the measured centre, the size in computational memory needed for each frame visualising the probability distribution of the wave function is extremely large. This is due to the large discretised grid size required. As a result, we are unable to analyse the wave packet at every single point in its evolution and a more efficient solution is to analyse the wave packet at larger time intervals. However, we know the path of the wave packet is not a straight line and by having large time intervals are we are measuring the distance “as the crow flies” rather than the real distance along the path.

We know from the previous chapter that the trajectory of the electron in the short path is not a simple straight line which goes under the region occupied by the deflection gate. Instead, it is a zig-zag pattern which we can see in the simulations of Fig. 7.5 causes a breakdown in the wave packet. Initially, as the wave packet direction of motion is changed we see some lengthening. This is continued even after getting half way through the simulations. But, the final wave packet in Fig. 7.5c shows the wave packet bunching up. This same behaviour is also observed in Fig. 7.4c of the long path, however, instead of restoring back to a resemblance of its original shape it stays bunched up and circular in shape. The reason for this could be that the consistent change in the path of the wave packet has thrown it into a higher energy. As energy is conserved, we find that electrons in higher Landau levels have a smaller wave number and in edge channels there is a correspondence between the wave number and the displacement in real space. Therefore, when we see parts of the Gaussian wave packet break apart and travel at different positions relative to the edge, as shown in the Fig. 7.5d, the electron hase jumped Landau level. As the wave packet is spread over multiple energies, there are different parts of it now travelling at different velocities. This could explain the bunching, as the tail end of the wave packet now travels at a higher velocity to the front end, it seems to catch up on itself.

The simulation of this HEQO device has shown to be extremely computationally costly. Even with efforts to reduce the domain size of the full model it still required twelve frames to simulate the long path and the numerical calculations of performing a gauge transformation between each frame. The added complexity also brought by the requirement of a strong magnetic field meant that a large discretised grid of 4096 × 4096 points had to be used in a frame domain of 1 μm × 1 μm having a discretised spacing, δx and δy, in order for there not to be an overflow with the k-space vector in the Fourier transforms. The accumulation of these limits meant that, for time saving purposes, a time step of $\delta t = 1\,\text{fs}$ was used. The requirement for δt is stated in Eq. (6.18) where inputting the parameters of this simulation we have the restriction $\delta t \ll 7\,\text{fs}$. In such a case, an ideal time step may be $\delta t = 0.1\,\text{fs}$ but we would require much more real time to calculate. We performed the short path simulation with a time step of $\delta t = 0.5\,\text{fs}$ rather than the $\delta t = 1\,\text{fs}$ used in the long path. The reason for this was that the initial simulations did use $\delta t = 1\,\text{fs}$ but the breaking of the wave packet occurred, just as is seen in Fig. 7.5c. As there were fewer frames than the long path, a lower time step was used to investigate if this would make a difference. The results improved slightly but the same breaking of the wave packet can be seen as well as the scattering into higher Landau levels. Improvements can be made in this regard but reducing the time step would drastically increase the total run time of the simulation. Although the numerical calculation of these simulations did use parallel coding, there is a limit to the time saved as the time to manage and delegate parallelism increases and redundant computation becomes more prominent.

Chapter 8

Quantum point contacts

A quantum point contact is an essential component to electronic interferometry experiments, playing the role of an electronic beam splitter [77]. They help to exploit the wave-like nature of the electron and are prominent in electronic interferometers such as the Hanbury-Brown-Twiss [78], the Hong-Ou-Mandel [79, 80], and the Mach-Zehnder[7, 8, 12] interferometer. Like an optical beam splitter, a quantum point contact will split the path of an electron into two with a non-zero probability of finding the electron in each path.

Quantum point contacts were first realised in 1988 as split gate configurations [81]. It is generally regarded as a narrow constriction created between two electrically conducting regions. More specifically, the width of this restriction is comparable to physical electronic properties i.e. the de Broglie wavelength $\lambda_B = h/p$. This first realisation of a quantum point contact was to constrict two-dimensional electron systems into one-dimension. In this chapter we study quantum point contacts under a perpendicular magnetic field [82–84] by first observing a simple model with a saddle-point potential created by a split gate based on the design of Refs [85, 14] which would later be used to report the first quantum point contact. We then consider a design of our own which will incorporate the features of this simple design but with HEQO characteristics.

Our motivation for this chapter is to study a Gaussian wave packet modelling the hot-electron interacting with the quantum point contact, splitting between a transmitted path and a reflected path. In a perfect scenario, the hot-electron will be split evenly between both paths. Experimentally, however, this is challenging problem as the hot-electrons energy must match with the potential energy of the system to split evenly, giving a very small margin of error. Therefore, we aim to design a quantum point contact where the rate of change of the hot-electron travelling between the transmitted path and the reflected path with respect to the electron's energy is as flat as possible.

8.1 Two-gate quantum point contact

Experiments using quantum point contacts proved useful in exploring a quantum-size effect on the conductance which would identify the one-dimensional density of states of electrons confined to a narrow wire [86]. To describe a bottlenecking of the potential, which creates a region where the electrons will become constricted, a saddle point potential can be characterised by

$$V(\mathbf{r}) = by^2 - ax^2 \tag{8.1}$$

given that a and b are positive coefficents. A transmission coefficient for a potential described by Eq. 8.1 is well known (for 2DEGs described by Schrödinger's equation) and with high magentic fields the expression is

$$T_n(E) = \left[1 + \exp\left(-\pi \frac{E_{n+1/2}(\hbar\omega_c + \zeta)}{l_B^2\sqrt{ab}}\right)\right] \tag{8.2}$$

given for the nth Landau level. We have also introduced a parameter dependent on the magnetic length and coefficients of the of the saddle point potential $\zeta = l_B^2(b - a)$. As an electron's path coincides with the saddle potential, depending on the energy with respect to the zero point of the saddle, there arises a non-zero probability for the electron to be both transmitted and reflected [87].

We begin by looking at a simple quantum point contact which requires only two surface gates with a negative applied bias. The surface gates are patterned to create a "pinch point" which would manipulate the potential energy at the 2DEG to constrict the possible paths the electron could take. Figure 8.1a shows such a model with the surface gates (gold) laid on top of a AlGaAs/GaAs heterostructure. Unlike the HEQO devices we have studied this far, we will not be observing the motion of the injected electron underneath the surface gates but rather in the regions underneath the free surface (white).

The tips of the triangular points are centred at $y = 0$ on the figure and spaced a distance of 50 nm apart along the x-axis. This distance was chosen to be larger than the characteristic properties of the electron (magnetic length and Fermi wave length) such that we can have more control over the constriction using negative biases. We also chose the width of these tips at their widest to be 200 nm to reduce the likelihood of quantum tunnelling. In this model, the electron will be injected at the bottom left of the figure, underneath the free surface along the edge channels are formed close to the intersection with the surface gates.

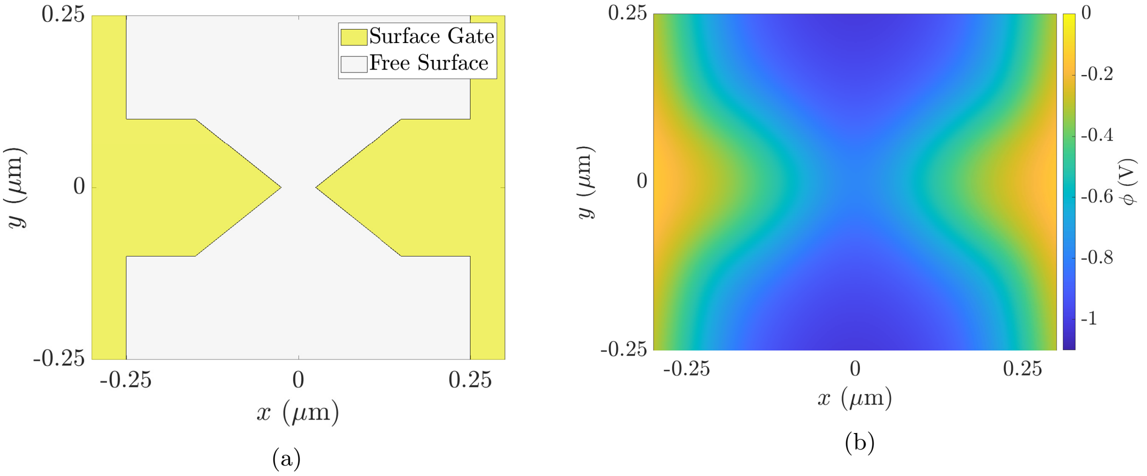

(a)

(b)

Figure 8.1: (a) A top view of a model of a quantum point contact comprising two surface gates (shown in gold) laid on top of a free surface (shown in white) of a AlGaAs/GaAs heterostructure. The gates are shaped as triangular points symmetrical about the origin and with a distance of 50 nm apart. (b) The electrostatic potential of the quantum point contact model with a voltage $V_g = -1.5\,\text{V}$ applied to both surface gates. The parameters shown in Table 3.1 are used for the heterostructure.

Although there is no etching in this model to worry about, we can still use the projected surface method to calculate the electrostatic potential as it is easier to apply the window functions to the geometry of the surface gates. The only difference here is that we project straight down through the heterostructure to the 2DEG. Figure 8.1b shows the resultant potential energy for our model with a voltage of $V_g = -1.5\,\text{V}$ applied to the gates. The large negative bias creates a pinch point in the potential, with a narrow bridge that runs across the origin of our model.

The resulting saddle potential created by these surface gates has a zero point exactly at the origin. We set as an arbitrary energy $\Delta E = 0$ for this zero point. Figure 8.2 shows the contour lines of electrons injected at the zero point of the saddle potential created with a surface gate voltage $V_g = -1.5\,\text{V}$. Labelled are the outermost paths injected at $\Delta E = -0.1\,\text{eV}$ and $\Delta E = 0.1\,\text{eV}$ for the transmitted and reflected paths respectively. The inner paths are injected at $\Delta E = -0.05\,\text{eV}$ and $\Delta E = 0.05\,\text{eV}$ respectively. We can already start to see from this figure, semi-classically, this non-zero probability of the transmission changing $E > 0$ and $E < 0$ that is shown by Eq. 8.2.

Figure 8.3 shows the probability distributions for a Gaussian wave packet at multiple times in the dynamic simulation. The wave packet is initialised at $t = 0\,\text{ps}$. For times $t = 0.5\,\text{ps}$ and $t = 1\,\text{ps}$ the wave packet follows the contours of the potential towards the quantum point contact. We can already see at $t = 1\,\text{ps}$ that the wave packet starts to

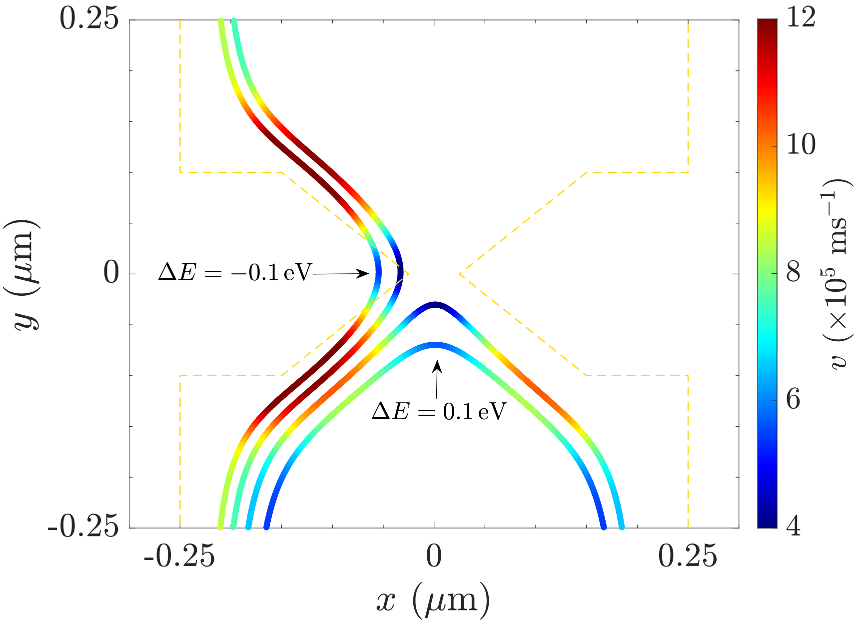

Figure 8.2: The paths followed by electrons injected at arbitrary energies defined about the zero point (i.e. $\Delta E = 0$) of the saddle created by the surface gates (dashed, gold lines). The paths for electrons with injected energy $\Delta E < 0$ are transmitted through the quantum point contact while those with $\Delta E > 0$ are reflected. The outer most transmitted and reflected paths are found at an injection energy $\Delta E = -0.1$ eV and $\Delta E = 0.1$ eV respectively (labelled). The inner paths are plotted for $\Delta = -0.05$ eV and $\Delta E = 0.05$ eV respectively. The instantaneous velocity is represented by the colour map within each path.

deform, with the front starting to bunch up and lose its symmetric Gaussian appearance. A snapshot of the wave packet splitting is shown at $t = 1.5$ ps where we can see the top and tail of already starting to spread into the transmitted path and the reflected path. The transmitted and reflected wave packets are labelled with the time stamps $t_T = 2$ ps and $t_R = 2$ ps respectively. In this model we have shown a 50/50 split between the two paths. Both of the split wave packets have spread out in length after travelling around the saddle potential produced by the quantum point contact. The initialised wave packet has a length of 200 nm but now it is measured to be over 300 nm. We can see a reason for this spreading is due to the variation in velocity around the centre of the saddle potential. The change in the distance the wave packet travels from $t = 0$ ps to $t = 1$ ps is generally the same. However, the distance travelled between $t = 1$ ps and $t = 1.5$ ps is relatively less indicating a reduction in velocity. This pinch point around the quantum point contact is reminiscent of the transition path in the TOF experiment where the reduction in velocity was shown to be large. Figure 8.2 shows for the multiple energy paths the instantaneous velocity within our model. As both wave packets exit the quantum point contact the respective tops travel along paths where there is an increase in the instantaneous velocity.

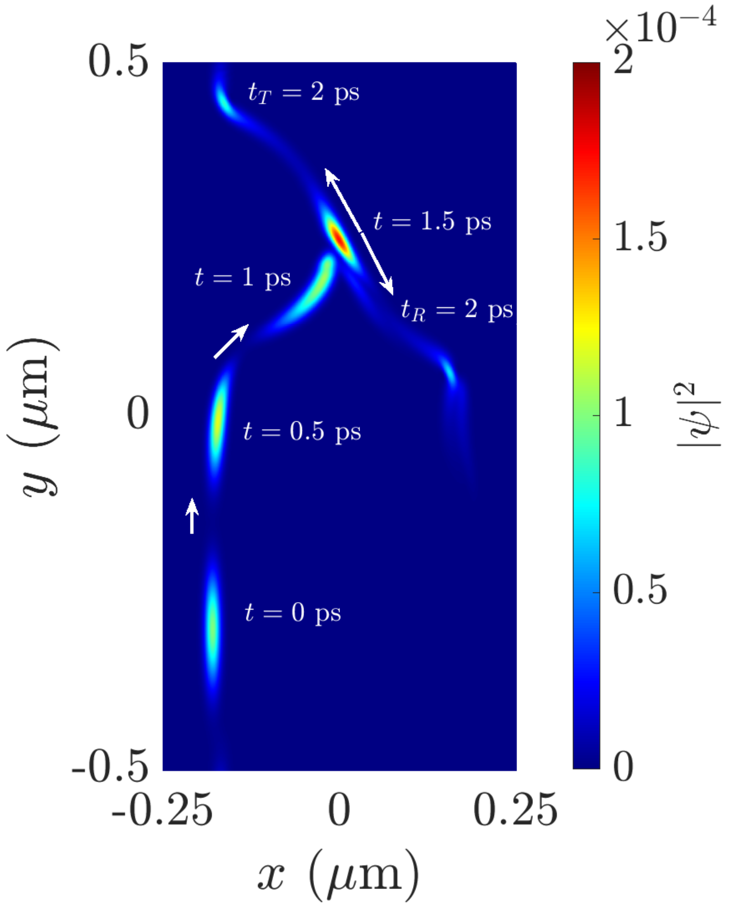

Figure 8.3: Dynamic simulation of a Gaussian wave packet initialised in the potential represented in Fig. 8.1b from $t = 0\,\mathrm{ps}$ to $t = 2\,\mathrm{ps}$. The Transmitted wave packet goes through the quantum point contact and labelled by the transmitted time $t_T = 2\,\mathrm{ps}$ and the reflected wave packet is deflected and labelled by the reflected time $t_R = 2\,\mathrm{ps}$.

Thus, there is a large spreading which includes a bulk probability distribution.

Figure 8.4 show the transmission for multiple wave packets with variations in the initialised energy for three voltages applied to the surface gates. As the energies are arbitrary, they have been reduce to zero such that the $\mathit{\Delta} E = 0$ is the zero point of each saddle potential produced by each voltage $V_g = -0.5$, -1.0, and $-1.5\,\mathrm{V}$, shown as the red, blue, and green line respectively. The transmission was measured by calculating the sum $|\mathit{\Psi}|^2$ for each half of the domain split by the centre of the quantum point contact. For lower absolute values of V_g, the width of the saddle potential is much wider. This increased width offers more regions of energy that split the wave packet to be transmitted and reflected. This is shown by a slower rate of change in the Transmission for injected energies. The trend follows for increases in absolute values of V_g creating a larger difference between transmission and reflection.

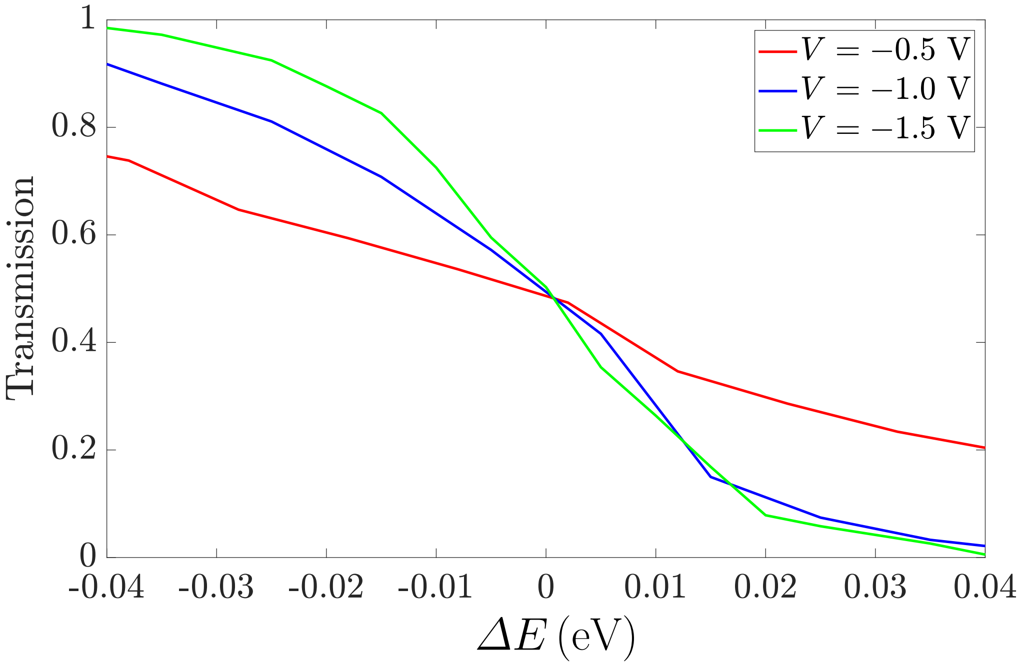

Figure 8.4: The transmission of an electron injected at an arbitrary energy $\mathit{\Delta E}$ where $\mathit{\Delta E} = 0$ is the zero point of the saddle potential. For $\mathit{\Delta E} < 0$ we observe a higher probability of the wave packet being transmitted through the quantum point contact, while for $\mathit{\Delta E} > 0$ we observe a higher probability of the wave packet being reflected.

The use of two depletion gates being used to constrict the potential is a simple and controllable way to create a quantum point contact. The variation in the voltage allows for a saddle potential which can be manipulated to allow either a wider or narrower constriction. By first identifying the zero point of the saddle potential within our electrostatic model, we were able to find contour lines where we would observe the paths of injected electrons. This semi-classical analysis showed that the transition between being transmitted and reflected is rather small in the energy range, within 0.1 eV around the $\mathit{\Delta E} = 0$ for a voltage of $V_g = 1.5\,\text{eV}$. This difference is studied in more detail by Fig. 8.4 where the Transmission showed a much quicker transition between being transmitted and reflected in a range of 0.08 eV. However, looking at the opposite end of the scale, for $V_g = -0.5\,\text{V}$ in the same figure, there is a much slower transition. The energy range we studied is not fully captured by the figure but is larger at a range of 0.12 eV, an increase of 50% for a decrease in voltage V_g of 66%.

The transmission represented for $V_g = 1.0\,\text{V}$ in Fig. 8.4 matches with the trend. However, there seems to be a discrepancy for values of $\mathit{\Delta E} > 0$. This region represents the reflected path of the wave packet. Looking at Fig. 8.3, although this is the dynamic simulations for $V_g = -1.5\,\text{eV}$, it still shows that the reflected wave packet has a large change in direction. This is also shown in Fig. 8.2 where the path at $\varDelta E = 0.05\,\text{eV}$ has a sharper change in direction at the quantum point contact, as opposed to the other paths. This large change in direction can be damaging to the simulation as it can throw the wave packet into higher energies. The simulations were performed with a time step of $\delta t = 0.5\,\text{fs}$ but by halving this, it may increase the accuracy of the simulations and therefore account for this discrepancy in the results.

Although this model does not show the distinct features of a HEQO device i.e. depletion gates and etching, it does offer valuable insight in important features of a quantum point contact. The width of constriction plays an important role such that a wider saddle potential can give a larger region for an injected electron to be split. We have also seen, as a secondary feature, how there is a reduction in velocity in the region encompassed by the saddle potential. In order to apply this to HEQO devices, we want to look to design a quantum point contact where an electron can travel in a region which is energetically and spatially separated from background electrons, rather than travelling near the 2DEG as in the case of this model.

8.2 Hot-electron quantum point contact

The model in the previous section utilised surface gates to squeeze the potential felt at the 2DEG and constrict the pathways of the electron such that there would be overlapping. However, that quantum point contact was not made for hot-electrons. Here, we introduce a design of a quantum point contact where which uses the fabrication techniques often used with HEQO devices: etching and surface gates.

The model will require a similar patterning of gates and etching in order to create a saddle potential. We showed in the Chapter 5 that, when compared to the TOF experiment, the hot-electron will travel close to the etched region, underneath the depletion gate. As such, we will use the etching technique in our mode to create the constriction. Figure. 8.5a shows our model, where there are essentially two islands of etched mesa connected by a small, constricted area centred about the origin. In this model, one of the points in the quantum point contact is placed at $(x, y) = (0, 0)$ while the other point is placed at $(x, y) = (-50, 50)\,\text{nm}$, for a total distance of $70.7\,\text{nm}$ apart. A depletion gate is overlaid, using the same width of $w_g = 500\,\text{nm}$ from the edge of the exposed, etched sidewall with an applied voltage $V_g = -0.25\,\text{V}$. Using the projected surface method we

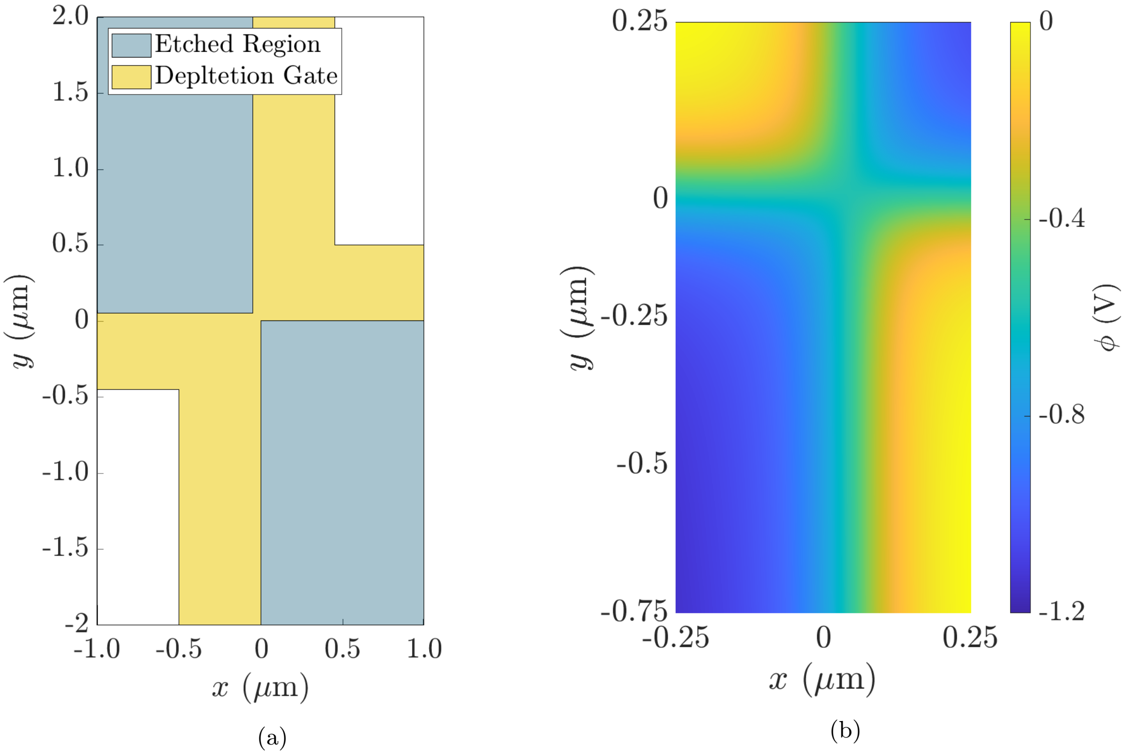

(a)

(b)

Figure 8.5: (a) A top-view of a model of a quantum point contact fabricated using etching and applied surface gates. The etched regions (shown in blue) leaves two islands of etched mesas (shown as the regions of white and where the depletion gates reside) connected by a small constricted part around the origin. In this particular model, the two vertices of the etched regions closest to each other about the origin are separated in the x direction by $\delta x = 50\,\mathrm{nm}$ and in the y direction by $\delta y = 50\,\mathrm{nm}$. (b) The electrostatic potential calculated using the projected surface method of the model (a) within the domain of $-0.25 < x < 0.25\,\mu\mathrm{m}$ and $-0.75 < y < 0.25\,\mu\mathrm{m}$.

can create window functions for the depletion gates, ethced mesa, and etched region to calculate the electrostatic potential shown in Fig. 8.5b. As with the previous quantum point contacts, the defining saddle potential has a zero point found directly in the centre of the two points. In this section we will take the electrostatic potential we calculated in the previous sections and apply our dynamic simulation calculations. We will initialise Gaussian wave-packets, used to model our hot-electrons, at multiple energies and observe the change in the transmission coefficient given in Eq. 8.2.

As we have observed in the previous chapter, the simulations require a region where the potential is translationally invariant in the direction of travel for the entire length of the wave-packet. Because of our choice of using the Landau gauge in the y-direction, we use a domain of $1\,\mu m \times 1\,\mu m$. Figure 8.5b shows this potential where you will observe that the centre of the saddle point sits in the region $y > 0$ and we have a long run in at the

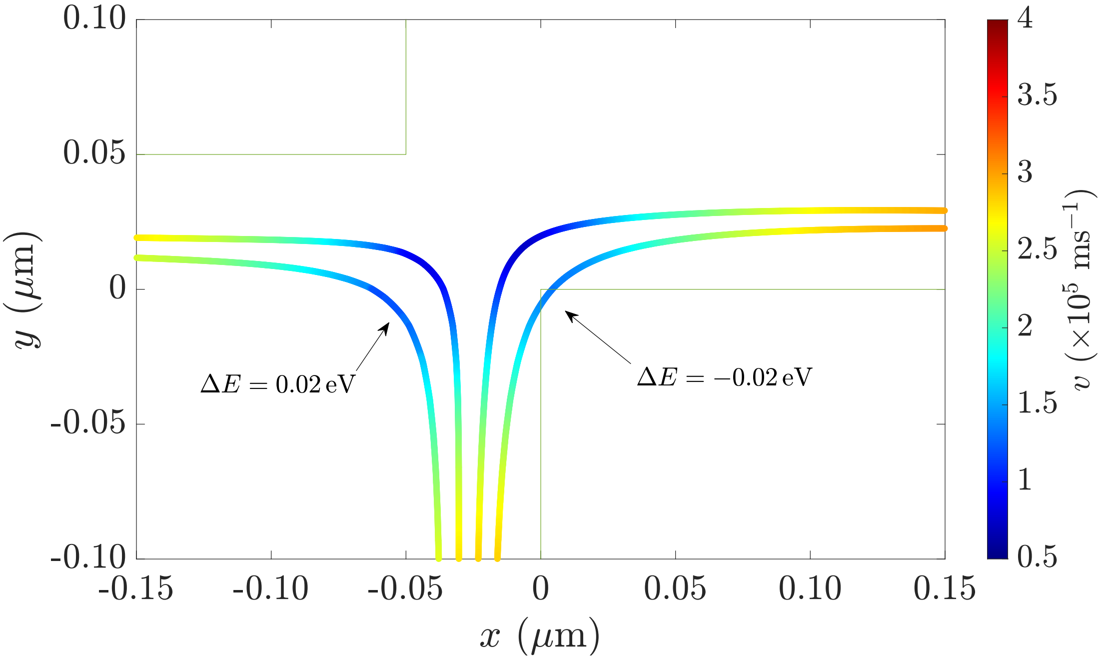

Figure 8.6: The calculated paths that would be taken by an injected hot-electron for an energy E around the quantum point contact. An energy range of $0.50 < E < 0.75\,$eV is shown and a transition point between the transmitted and reflected paths is found between $0.60 < E < 0.65\,$eV. The centre of the saddle point is found at $x = 0.025\,\mu$m and $y = 0.025\,\mu$m.

bottom where the potential is uniform i.e. for $y < 0$, the electrostatic potential looks like it is translationally invariant in the direction of motion y. Unlike with the TOF simulations, we are only interested in the small region around the QPC to show the transmission and reflection of the wave packet. As such, we can afford to be explore the simulation a bit more with a larger discretised grid and hence a full range of magnetic fields, unlike with our TOF experiment.

Figure 8.6 shows the trajectories of four paths the hot electron could take around the zero point of the saddle point potential. For the outermost paths the maximum injected energy is $\Delta E = \pm 0.02\,$eV and the inner paths represent energies at $\Delta E = \pm 0.01\,$eV respectively. In comparison to the two-gate quantum point contact shown in Fig. 8.2 of the previous section, the difference in the rate of change of direction between the transmitted path (travelling through the quantum point contact and going right) and for the reflected path (going left) is far greater. Here we can already see that a wave packet spread over equally in the two paths will have a well defined splitting in the wave packet. These trajectories also have a colour map representing their instantaneous velocities for a given position the path. Again, we observe that around the zero point there is a large slowing

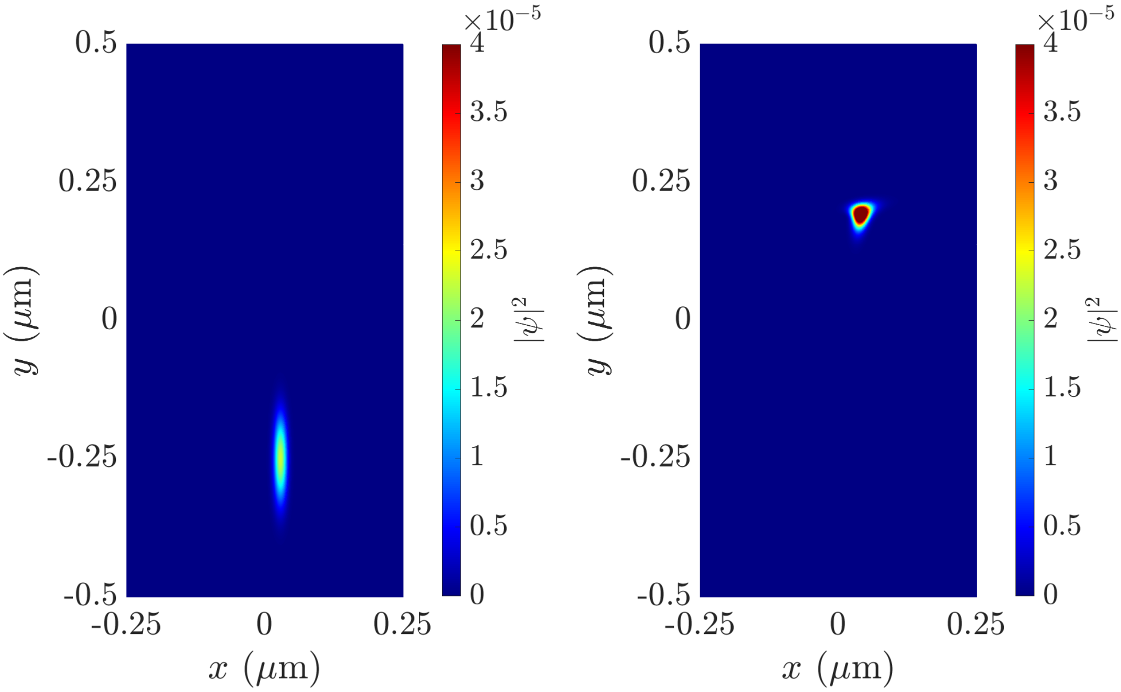

(a) $t = 0$ ps

(b) $t = 1.5$ ps

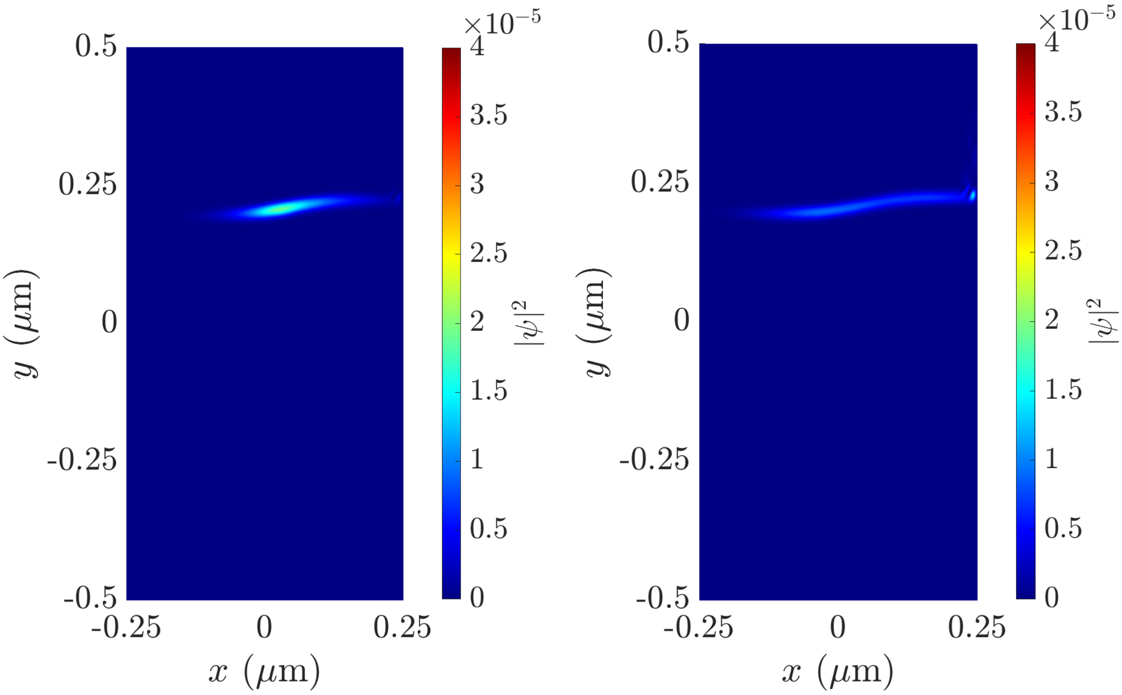

(c) $t = 2.25$ ps

(d) $t = 2.5$ ps

Figure 8.7: Dynamic simulations of a Gaussian wavepacket initialised at an energy $\varDelta E = 0$ and with a magentic field of $B = 5\,\text{T}$. A discretised grid of 2048×4096 was used with a difference of $\delta x = \delta y = 0.244\,\text{nm}$ between each point. (a) shows the initialised wavepacket at $t = 0$ progressing as labelled in figures (b), (c), and (d) to a final time $t = 2.5\,\text{ps}$.

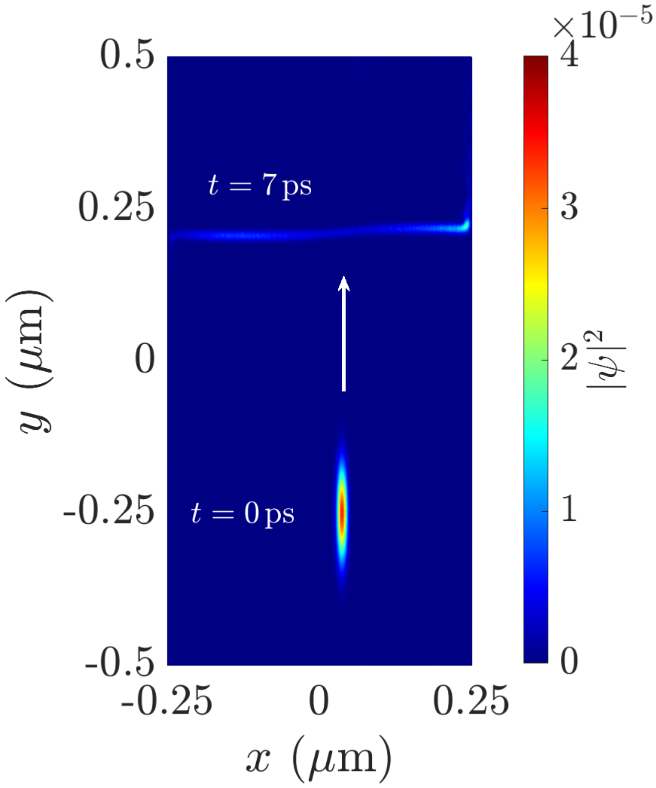

Figure 8.8: Dynamic simulations of a Gaussian wavepacket initialised at an energy $\Delta E = 0$. A magnetic field of $B = 11\,\mathrm{T}$ is applied perpendicular to the xy-plane. Compared with the initialised wave packet from Fig. 8.7a the width of this wave packet is much narrower but the splitting is more defined when compared to Fig. 8.7d. The time taken to the splitting of the wave packet is $t = 7\,\mathrm{ps}$ which is much slower than the $t = 2.5\,\mathrm{ps}$ of the $B = 5\,\mathrm{T}$ simulation.

down in the velocity and then accelerating again when passing the quantum point contact.

In Fig. 8.7 we show the probability distribution of the Gaussian wave packets in the electrostatic potential shown in Fig. 8.5b. We note here that electrostatic potential we implement into the dynamic simulations is identical to this figure but the domain in Fig. 8.7 has changed for ease of transformation from real space to Fourier space. Here we have initialised the centre of the wave packet in the position $x = 52\,\mathrm{nm}$ and $y = -250\,\mathrm{nm}$. For this figure we have used a magnetic field $B = 5\,\mathrm{T}$. The initialised point offers a uniform potential for all of the wave packet in the y direction. The wave packet travels initially unperturbed as it travels towards the quantum point contact. However, as it gets closer to the centre of the saddle point we observe a "bunching" of the wave packet. Each frame shown in the figure has equal spacing in time steps δt, showing that there is a slow down in the velocity of the wave packet. This will explain the bunching as the length of the wave packet experiences different instantaneous velocities at different points, we find the front will slow down while the velocity of the back is still high. As a comparison of simulations for magnetic fields, Fig. 8.8 shows the wave packet initialised at $\mathit{\Delta} E = 0$ but now with a magnetic field of $B = 11\,\mathrm{T}$. The initial wave packet, in comparison to the $B = 5\,\mathrm{T}$, has a much narrower width representing a stronger confinement of the wave packet in the potential. We can also see from the figure that the time taken for the wave packet to split is $t = 7\,\mathrm{ps}$ while for $B = 5\,\mathrm{T}$ it was $t = 2.5\,\mathrm{ps}$, showing the effect that the magnetic field has on the velocity.

As the wave packet is spread over multiple energies and we have initialised it close to the x value of the centre of the saddle point, we can see that parts of the wave packet will start to follow both paths that are either transmitted or reflected. In this exemplary figure, the splitting is 50/50 such that we have equal probability distributions travelling in either path. An interesting observation is the spreading of the wave packet after coinciding with the quantum point contact. As with the bunching at the centre of the quantum point contact we also see that parts of the wave packet have different instantaneous velocities as it leaves the quantum point contact as well causing this spreading. Immediately after the quantum point contact the velocity of the path will go back to the average velocity on straight edge-channels. Comparing with trajectories of the hot electron in Fig. 8.6 we can see how this bunching comes into effect. At the bottom of the figure the paths are all close to one another but as they reach the zero point the difference in position is much larger. This spreading in the distance of the energies mean that wave packets spread over multiple energy levels will start to spread with it. The increase in distance between each path also corresponds to a lower gradient in the electrostatic potential and hence a lower velocity, which explains the reduction velocity around the zero point.

For the previous simulation we use a magnetic field strength of $B = 5\,\mathrm{T}$, strong enough to put our system into the quantum Hall regime. However, HEQO devices can use stronger magnetic fields as high as $B = 14\,\mathrm{T}$ [45]. A higher field strength can contribute to a stronger confinement of the electron and suppress LO-phonon emission [48]. In Fig. 8.9 we show the transmission for the arbitrary energy $\mathit{\Delta} E$ for two magnetic field strengths, on either end of the spectrum for the strong field quantum Hall regime. For $B = 5\,\mathrm{T}$ (orange) we see there is a low, sloping gradient that that goes from $T = 0.95$ to $T = 0.08$ within a change of 40 meV. However, when we look at simulations where there is stronger magnetic field at $B = 11\,\mathrm{T}$ (blue) we see a sharper change in the transmission. In particular, we observe a quicker rate of change around the centre at $\mathit{\Delta} E = 0$ where $T = 0.50$. We can see why this is with the change in the width of the wave packets for both magnetic fields in our simulations. The spreading of the wave packet over less energy levels reduces the number of these semi-classical paths and hence the change between fully transmitted and fully reflected happens at a higher rate of change.

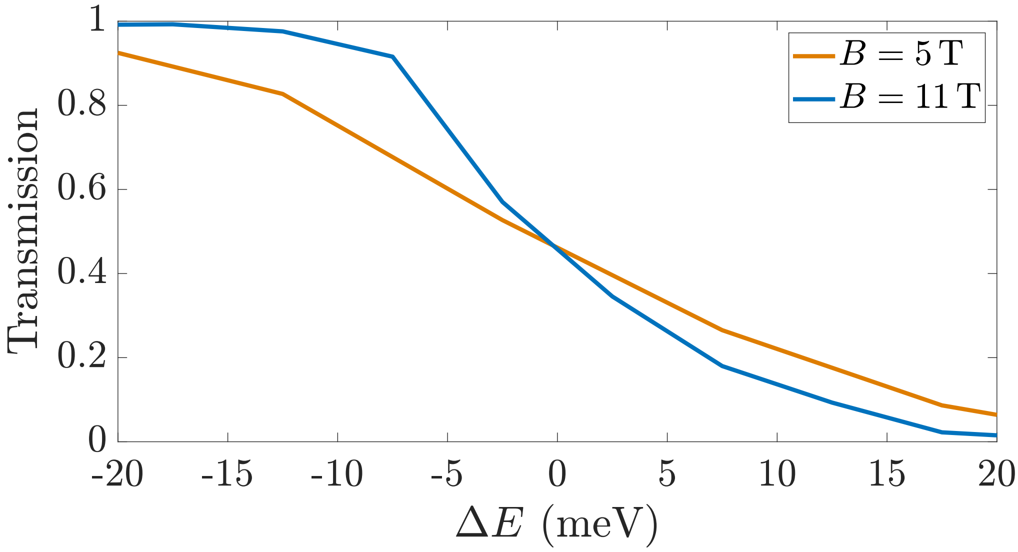

Figure 8.9: Plot of the transmission rate through the hot electron quantum point contact. The electrostatic potential for this simulation is shown in Fig. 8.5b. Two magnetic field strengths of $B = 5\,\mathrm{T}$ (orange) and $B = 11\,\mathrm{T}$ (blue) were used. The higher magnetic field showed a sharper constriction causing the transmission rate of change to increase.

8.3 Realistic quantum point contact

Our design of a quantum point contact for hot-electrons was fabricated using etching and a depletion gate. Although the depletion gate could be used to control the height of the saddle-point potential barrier, it was the etching which created the saddle shape required to split the path of the electron in two. We now look at another design, which also gives us the characteristics we require for hot-electrons, but now more controllable.

Figure 8.10 shows a top view of a model of a quantum point contact provided by Masaya Katoaka and Patrick See. This is part of an electronic Mach-Zehnder interferometer and more specifically it is the first quantum point contact. Our first observation is that the design is reminiscent of the deflection gate of the TOF experiment in Chapter 7. We have two deflection gates (in grey) alongside an etched region (green) which forms the edge channels in which our hot-electrons are found energetically and spatially separated from background electrons. However, instead of having a pinch point to constrict the potential and deform the electron path we have beamsplitter gate (red). Depending on the negative bias applied to the gate, the electron can either be transmitted through or reflected away. As with the deflection gate of the TOF experiment, the difference in

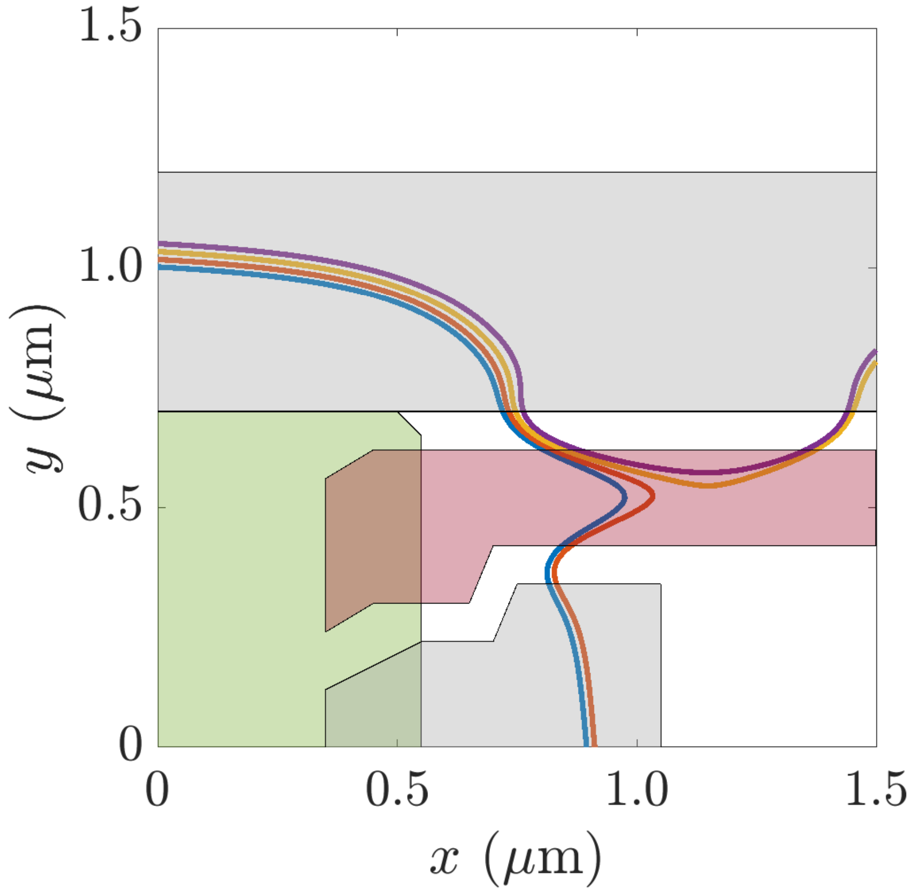

Figure 8.10: A design of a quantum point contact taken from a model of a Mach-Zehnder interferometer, provided by Masaya Kataoka and Patrick See.

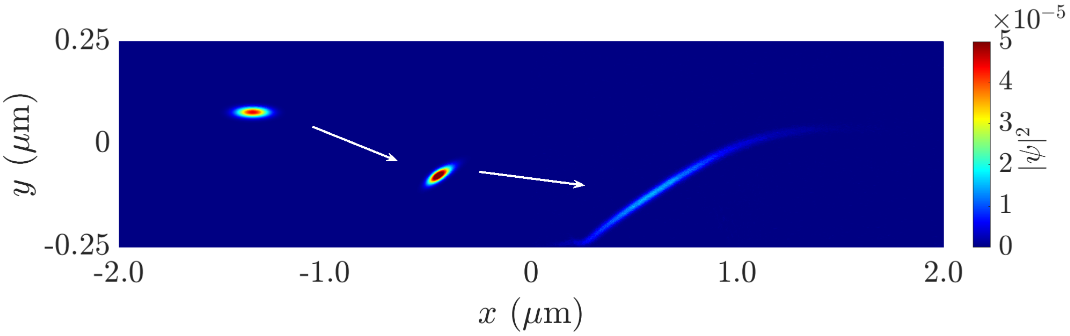

Figure 8.11: Probability distribution of simulated wave packets modelled on the design represented by Fig. 8.10. The simulation is initialised in the top left of the figure, underneath the depletion gate. As it travels towards the beamsplitter gate it spreads through both the reflected and transmitted paths.

the electrostatic potential around the gate creates much more subtle variations than the saddle point potential created by the previous models of quantum point contacts in this chapter. This can be seen by the contour lines in Fig. 8.10 where the path in which the electron will be transmitted (carry on travelling to the right of the figure underneath the depletion gate) and has a much smaller change in direction. It looks as if it is travelling in saddle point potential which has been stretched out in the x direction of the figure. In comparison the reflected path (which travels underneath beamsplitter gate in the y direction) has a sharper change in direction.

We have already seen in the previous simulations and semi-classical analysis that the velocity of the wave packet is very slow when travelling around the zero point of the saddle point potential. We also saw in the previous simulations that the slow down in the velocity created a large dispersion in the wave packet. Figure 8.11 shows the simulations of a wave packet initialised in the model of Fig. 8.10 where the wave packet begins on the furthest left of the figure and follows the arrows to the final wave packet on the furthest right. In this simulation we have overlapped two separate domains which required a Gauge transformation between the two. Each simulation was performed in a domain of $0.5\,\mu$m in the y direction and $2\,\mu$m in the x direction. In the figure, the wave packet begins like all previous simulations in a uniform and Gaussian shape. However, at the intermediate point of the simulation, during the approach to the splitting point in the electrons path, the wave packet rotates as if it is travelling sideways. This carries on further until the wave packet has dispersed down both the transmitted and reflected paths.

The shape of the saddle point that this model creates is clearly not as well defined as previous models. Because of this we see that the spreading of the wave packet takes place before the the zero point of the potential. Unlike previous simulations, the spreading is now occurring at a perpendicular direction to the direction of motion of the wave packet. Although we saw in the TOF simulation that the wave packet can be scattered to higher Landau levels, it does not show the characteristics of that here. Instead, we are seeing the bunching which took place in previous quantum point contacts where there was more area of the potential with the same energy but now it is occurring further out in the paths from the zero point. Because of this, the wave packet is splitting into two paths much earlier than expected. We can see this in the semi-classical picture of Fig. 8.10 where the paths are distributed evenly in the area where the wave packet is initialised but move closer together just before the zero point.

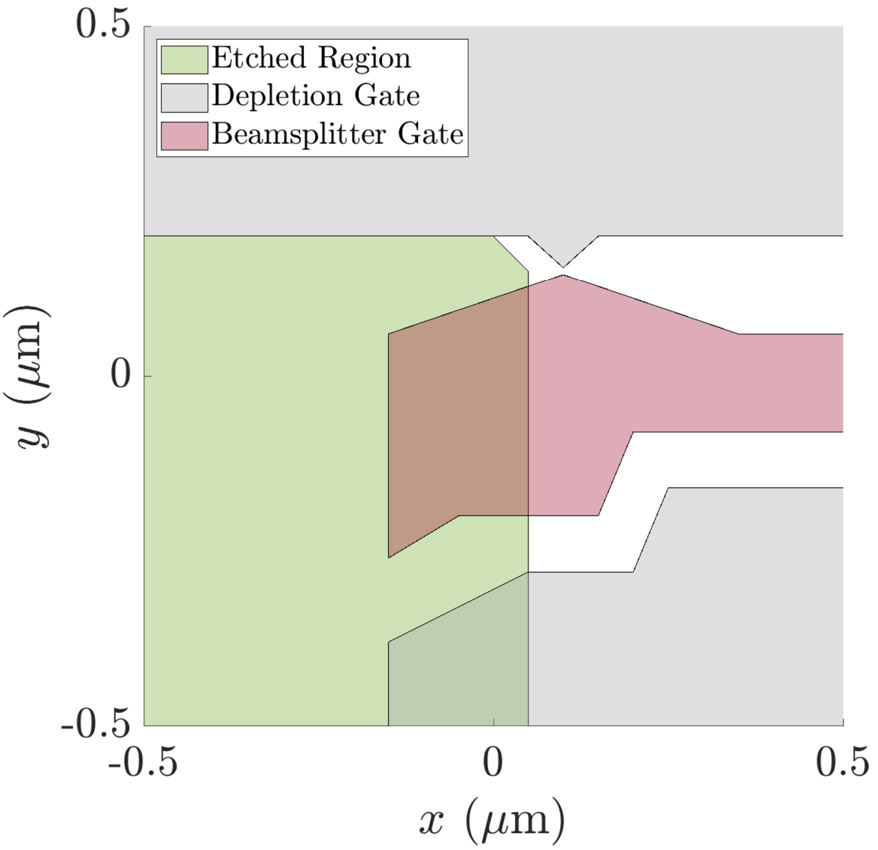

Figure 8.12: Redesign of the quantum point contact in Fig. 8.10 where two protrusions in the shape of triangular gates are added to the top depletion gate and the beamsplitter gate. We have used the same types of gates such as the depletion gate (grey) and the beamsplitter gate (red). The etched region (green) also remains unchanged. The distance between each triangular point is 25 nm.

8.3.1 Redesign

The slow velocity and the dispersion of the wave packet makes it much more difficult to measure the transmission rate for a quantum point contact of this design. This is because the simulation requires a lot more time to run in order for the wave packet to be completely split apart. However, we can expand on this realistic model to try and redesign this quantum point contact using the characteristics of previous models.We now take the opportunity to take what we have learned from sections 8.1 to attempt a redesign of a realistic quantum point contact.

From section 8.1 we found that when there was a larger voltage applied to the two depletion gates, there was a stronger constriction in the potential. This created a steeper rate of change in the transmission between fully transmitted and fully reflected. Although

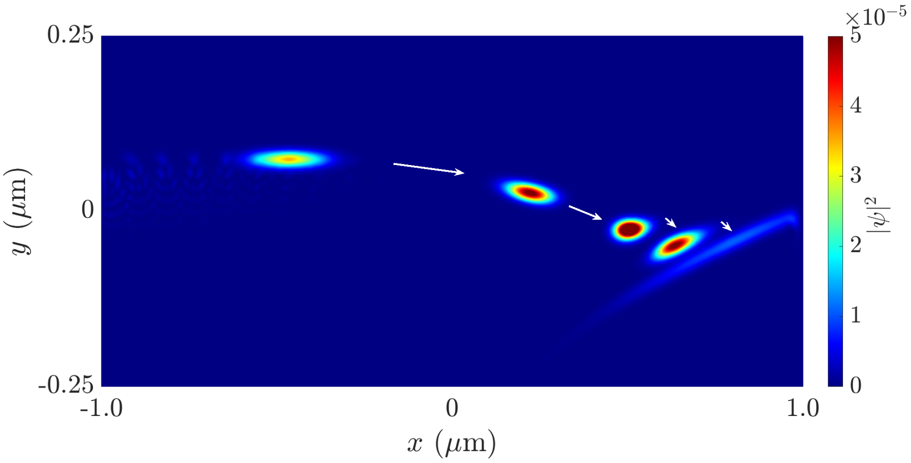

Figure 8.13: Simulation of the redesigned quantum point contact from the model in Fig. 8.12. Note that there is scattered wave packet around the initialised wave packet (furthest left) which originiates from the final wave packet (furthest right) reaching the edge of the periodic boundary conditions.

it meant a smaller region of energy would give a close to 50/50 split of the wave packet, it does mean that there would be two well defined wave packets after the splitting. Because of this, we have created a model for a quantum point contact where we have altered the top depletion gate and the beamsplitter gate such that there is a pinch off point to create a more constricted saddle point potential. This redesign can be seen in Fig. 8.12 where essentially two triangular points are modelled with the tips of each triangle at a very narrow distance of 25 nm apart. One of the observation we made in the previous quantum point contact was the distortion in the saddle point potential which, when looking at the paths the wave packet would travel, elongated the zero point. This distortion slowed down the wave packet and meant the spreading was slower. Due to this, the addition of the triangular point on the top depletion gate has been made to be sharper than the triangular point on the beamsplitter gate to reduce that distortion. the voltage applied to the depletion gate and the beamsplitter gate are the same as the original design where we have $v_g = v_{bs} = -0.65\,\mathrm{V}$. We also continue to use a magnetic field strength of $B = 5\,\mathrm{T}$.

Figure 8.13 shows the simulation of the wave packet in the redesigned model of the quantum point contact. The initialised wave packet is at the most left of the figure and progresses in equal time steps to the right, ending at the final wave packet on the most right of the figure. To help with the size of the domain of the simulation, the adapted triangular gates were placed such that the saddle point potential it creates is moved closer to the etched region in order to fit within a smaller domain. The motion of the wave packet is largely the same as the original model, however the distortion in the shape of the wave packet occurs much closer to the zero point of the potential where the splitting occurs. If the simulation in Fig.8.13 continued, we would see the eventual splitting of the wave packet. This simulation shows that the inclusion of the triangular shaped gates has manipulated the trajectory of the wave packet by keeping the distance between the path of different energy levels consistent for longer before splitting into different directions.

Part IV

Conclusion and outlook

Chapter 9

Conclusion

In this thesis, we have explored in detail the process of modelling HEQO devices and performed simulations of the motion of the electron in realistic experiments. The experiments in question do not know how an electron behaves before their detection, so the work shown here provides some theoretical insight into this world. Overall, the use of hot-electrons has raised some challenges in comparison to cold-electrons. However, we have shown that it is possible to overcome these challenges and have laid the ground work for future work to progress quickly.

9.1 Conclusion

In part II, we studied separately the fabrication techniques of etching and application of surface gates to show how changes to the surface of an AlGaAs/GaAs heterostructure would affect the electrostatic potential within. This concluded that in order to find how the electrons are confined we would need to solve the Laplace equation. Following the work of Davies in Ref. [47] & [32] we introduced a method which we call the projected surface gate method. This allowed us to model the electrostatic potential at the depth of the 2DEG in a closed form equation for any HEQO that uses both etching and applied surface gates. We envision this method to be very useful in the pre-fabrication stages of an experiment. This method only requires information on what the top surface of the device looks like i.e. the window functions of the etched region, etched mesa, and the surface gate. This takes away the need to create a full three-dimensional CAD model which would then be needed for other method such as the FEM to calculate the electrostatic potential. This method also prove particularly useful when there are variations to the applied voltage to surface gates. The projected surface method is an additive calculation, which is to say that if there is a change in the voltage of a surface gate, we can perform the method for a window function of just that surface gate and add it to the full calculation. For example, in the TOF experiment, for multiple voltages of the deflection gate, we can calculate the electrostatic potential for the whole system and then when we want a new result for a different value of V_d we can just perform the method on that gate only and add (or subtract) the resulting electrostatic potential from the previous result. This greatly speeds up the process over methods such as the FEM which would require a re-calculation of the entire model.

To test the accuracy of the projected surface method we compared the results to an exact solution of the FEM. When comparing to our two-dimensional and three-dimensional models we saw that there was a consistent area which led to differences. The regions in the 2DEG close to the exposed sidewall of the etched mesa showed differences between the two methods. A main contributor to this could be the size of meshing required by the FEM, which is mostly down to computational cost. The depth of etching is 60 nm, which extremely small when considering micron scale of the full device. As such, for accurate calculations which taken into account the full effect of the boundary conditions on the exposed etched sidewall, a very small meshing is required. The projected surface method, however, bypasses this boundary condition in order to get an approximation of the electrostatic potential at the depth of the 2DEG. When comparing with the FEM, in the TOF analysis, the region where we observe electrons with similar injected energies to our model is far away from the etched sidewall and closer to regions where the FEM and the projected surface method align better. This may become an issue if we were to find the hot electron has a higher energy in the experiment which correspond to a region closer to the etched sidewall. In such a case, it may be ideal to perform the projected surface method multiple times through the model. This would allow us to implement some boundary conditions imposed on the etched sidewall. However, we would need to consider the limitations in the depth of the projection in order to obtain accurate results. We only considered shallow etching in this thesis, but this method could be applied to deep etching (where the etching is performed past the 2DEG), and in such a case multiple projections would be needed.

One of the advantages we discuss of the projected surface method over the FEM is the computational cost. Obtaining similar results for the full TOF model by solving the full Poisson equation requires us to work in a 3D domain. With linear dimension L, a multi-grid method to a fixed error tolerance takes resources of $O(L^3)$ [88]. Turning to the projected surface method, we see from Eq. (4.6) that to evaluate the potential at a single point in the 2DEG involves two integrations over L^2. To obtain the results presented here we have used a direct summation to evaluate these integrals. This approach is rather inefficient and evaluating the integrals this way scales like $O(L^4)$. If instead we were to use e.g. Simpson's rule, the cost of evaluating these integrals reduces dramatically and the total cost of this method is $O(L^3)$, i.e. comparable with multi-grid. This can, however, be improved further. Firstly, the types of device in which we have studied in this thesis have a potential at $-h$ that consist of a few distinct regions, each with a fixed voltage. Provided these regions are polygonal, the projected potential at $z = 0$ from these sources can be calculated analytically as in [32], just as in the 1D case. Performing this first step analytical leaves just one numerical integral to be performed. Secondly, concerning the number of points that needs to be evaluated, it is clear that we don't need to evaluate Eq. (4.6) over the entire 2DEG as the valid electron trajectories are limited to the edge regions. Indeed considering geometries like the TOF experiment, the number of points that need to be evaluated will scale more like the length of the loop than its area. Taking these two factors into account, the scaling of the projected surface method can approach $O(L^{3/2})$. This represents a significant speed up over the full Poisson solver.

There is a second speed up, that comes when considering an ensemble of experiments performed at different gate voltages. From Eq. (4.6), we see that the potential at the 2DEG depends linearly on the surface potential which in turn depends linearly on the applied voltages. This means that contributions from etching and different gates can be worked out individually and then combined with appropriate voltage weights. This is seen explicitly in the 1D expression Eq. (5.1) but the same idea applies in 2D. This is advantageous because experiments typically sweep over gate voltages and, in the projected surface method approach, results at different voltages are simple to recalculate. This is in contrast with a full Poisson solver. Especially for devices which used both surface gate and etching, by changing the the voltage applied to a surface gate there will be a change in the boundary conditions on all the surfaces around it. As we have seen, usually the surface gates are laid close to an exposed etched sidewall, which already has complicated boundary conditions. Therefore the FEM would need to re-run the whole calculation afresh for each gate voltage. This feature of the PSM will be particularly valuable in complex structures where optimum voltages can readily be found by sweeping over a large set of gate parameters.

As a result of the electrostatic potential calculated from the projected surface method, we were able to perform semi-classical analysis on the trajectories of the hot electrons in the modelled experiments. This resulted in finding that the instantaneous velocity of the hot-electron varies dramatically throughout the TOF experiment. Although we are observing paths which have arbitrary energy when comparing to the experiment, the result for all energies are the same: there are large changes in velocity caused by the complex geometry of the energetic landscape. An interesting observation was the region around the deflection gate which showed that the transition point in the deflection gate voltage had two paths align very closely to one another. Experimentally, there is an issue of a broad barrier profile giving not such a sharp convolution with the wave packet in gate based detectors (like the one used on this device). This observation would help tackle the question of the noise from an electron pump, by considering the tunnelling trajectories over the exit barrier. In addition the use of the projected surface method and the subsequent analysis of the electron path could provide quick and easy alterations to the geometry of the deflection gate to understand the tunnelling trajectory [89].

This modelling and semi-classical analysis could play an important role in the design stages of HEQO devices. In particular, the Mach-Zehnder interferometer requires the use of two quantum point contacts as electronic analogues of beamsplitters. The first would split the path of the electron into two and the second would recombine the two paths together. However, as we have seen in our analysis of the TOF experiment, there is a lot of variation in the instantaneous velocity of the hot electron. As such, a Mach-Zehnder interferometer designed such that the chiral edge states follow the exact path of the photonic analogue may not provide identical variations of velocity in order for the hot-electron two paths to recombine at the same time. This is where the importance of the efficiency of the projected surface method allows for a quick calculation of the electrostatic potential of the system. Multiple designs could be made and analysis of the velocity easily calculated. The information of the model provides the distance and velocity of each path to calculate the time of arrival at the second quantum point contact.

In part III we follow the work of Andrea Bertoni to model an electron as a Gaussian wave packet and simulate how it will evolve in time around a potential landscape we calculate using the projected surface method. The numerical method was first demonstrated for a confining potential modelled as a Fermi distribution where we show the wave function can be converted into an edge state wave packet and how the spreading over multiple energies demonstrates its evolution. We have shown that the discretised grid has requirements in its size dependent on the magnetic length which gets smaller as we increase the magnetic field strength. Because of this to simulate hot-electrons it becomes very computationally costly as we require each domain to be limited to 4096 by 4096 points in a domain size of 1 micron by 1 micron. This proved tricky when simulating large devices such as the TOF experiment where the domain was 5 microns by 5 microns. As such we are able to take segments of the full potential and observe how the wave packets evolve in this small section. We then apply gauge transformations to move it to another segment, or frame, and carry on the simulation. Numerically calculating all this proved to be a time consuming task and we showed that for a TOF experiment with a reduce path length, it required at most twelve frames with eleven gauge transformations. As the wave packet evolved through the system it become apparent that the integrity of the wave packet became more disordered as time went on. When performing the gauge transformations we had to essentially cut and paste an area around the wave packet into the next frame of the simulation. For ease of calculation, this cut and paste was done in quartered segments of each frame. As such, the transfer of 100% of the wave packet was not possible. In the final frame of the long path we found $\sum |\psi|^2 = 0.976$, losing 2.4% of the total probability distribution. As a comparison, the short path only lost 0.4% of its total sum of the probability distribution. Although not detrimental to the accuracy of the simulation, it does mean that for future simulations in a larger modelled device it can become a problem.

In addition to the increase in computational cost due to increased grid size, the simulations have a restriction in the value of the time step between each evolution. For parameters of our models, this limit was given as $\delta t \ll 7\,\mathrm{fs}$. The simulations we have shown have used a value of $\delta t = 1\,\mathrm{fs}$ which, although smaller than the limit, is not order of magnitudes smaller. To see how this would affect the results in chapter 7, we used a time step of $\delta t = 0.5\,\mathrm{fs}$ for the simulations for the short path as there were over half as many frames needed than for the long path. However, even with this smaller time step the wave packet began to break up and become disordered even from the third frame. The same set of simulations were performed for the short path with $\delta t = 1\,\mathrm{fs}$ were performed but the same result occured. Although, we showed in chapter 5 that the paths around the deflection gate were extremely varied, the consecutive changes in direction could have thrown the wave packet off its initialised path. From our experience with the simulation, if a wave packet is left to run on a simple straight edge of a confining potential it will not distort as much as shown in the TOF simulation. The size of the devices also required a large amount of time steps to be calculated which, with the minute error for each step, accumulates to create large errors. This can be seen particularly in the long path of the TOF simulations for the final frames and even in the final frame of the short path. This is also exaggerated by the total number of gauge transformations required.

Overall, the simulations for the TOF experiment offered insight into the quantum transport properties of the hot electrons through the device. As the purpose of the TOF experiment is to measure the drift velocity of the hot electron, we pursued the same objective in the simulation. This provided us with good approximations to the experiment where we were able to get results for the drift velocity, calculated using the same method as the experiment, within the right magnitude. However, for this calculation we relied on calculating the distance the wave packet travelled. As the wave packet is Gaussian we assumed that the centre of the wave packet would be the maximum value of $|\psi|^2$ and we could track this value throughout the simulation. This proved challenging when we found that over time, the Gaussian like properties of the wave packet began to deteriorate. Although we were being consistent with our calculation of the centre of the wave packet, it may not be the most ideal method. In light of this, a different approach which may be better for future simulations is a method of finding the outer most points of the wave packet in the x and y direction and drawing a line between each point in its respective axis. The intersecting point of the two lines could then be used as the new centre. This method would be adjustable for wave packets that become extremely disorganised.

In addition to the discrepancy of calculations for the centre of the wave packet, the distance we calculate between each time in evolution may contribute to an error in the distance. Taking a snap shot of the wave packet in a grid size of 4096×4096 and finding the centre wave packet calculation is computationally costly. For this reason, the calculation is not done for every step in time δt but for every $1000 \times \delta t$. In regions where the wave packet is travelling in a translationally invariant system in the direction of motion, this is not a problem. But, for more complex systems it would mean we are calculating the distance more “as the crow flies” rather than following the exact path. Future simulations would need to consider this depending on the model in question and make adjustments. This could be done by reducing the total time between each point we observe in the wave packet evolution.

Finally, we exploited these simulations further to simulate the behaviour of a single electron around a quantum point contact. In the study of electron interferometry, quantum point contact are an essential component forming the electronic analogue of a beamsplitter. Our initial model of quantum point contact was one that would not be used in HEQO devices and was used more as a proof of concept. The two depletion gates would create a pinch point in the shape of a saddle-point potential, constricting the 2D domain into a 1D domain at the centre. This model provided us with the foundation of using these numerical calculations to simulate how a Gaussian wave packet would interact with a realistic quantum point contact. As it wasn’t based on a HEQO experiment, we used a lower magnetic field to lessen the computational cost. We then wanted to design a simple quantum point contact which used the characteristics of etching and depletion gates which are used in HEQO devices. Learning from the cold-electron quantum point contact, an etched constriction was modelled with a depletion gate covering it which allowed for some control over the value of the potential. This created a saddle point much like the prior model but now provides the characteristic spatial and energetic separation from background electrons. As HEQO devices also require strong magnetic field strengths we look at two sets of simulations for field strengths $B = 5$ T and $B = 11\,\mathrm{T}$. From the transmission equation, which has a dependence $\exp[-1/l_B]$, an increase in magnetic field means a decrease in the magnetic length and hence an increase in the rate of change of the transmission possibility from transmitted to reflected. Our simulation shows this result and the comparison with a lower, but still strong, field strength of $B = 5\,\mathrm{T}$.

From these two initial models of quantum point contacts we noticed that the probability distribution of the wave packet began to bunch up and change its shape as it approaches the zero point of the saddle point potential. For both models we performed semi-classical analysis on the trajectories for hot electrons with energies close to the zero point. This gave us a clearer picture of why the bunching of the wave packet occurred as we observed that in areas away from the saddle point, the paths were uniform and equally spaced in energy. However, the approach towards the zero point caused them to spread. The wave packet is initialised over multiple energy levels and as the trajectories for each energy spread, so will the probability distribution over a larger space. This analysis would prove useful in initial modelling of a quantum point contact. Depending on the characteristics one could exploit the manipulation of the electrostatic potential, and hence the potential energy, to get the desired characteristics from their design.

We then set out with our final model of a quantum point contact, the design of which was provided to us by Masaya Kataoka and Patrick See. From our analysis on the TOF experiment, this design looked reminiscent of the deflection gate used in that experiment. The use of a deflection gate was found to have an interesting deflection point which, from the semi-classical analysis, looks similar to the transitions in path around a quantum point contact. However, for this design in particular the depletion gate (labelled a beampsplitter gate) created a saddle-potential where the zero point looks to be elongated. This resulted in the wave packet in our simulations slowing down to very low velocities and spreading into both paths without a clear defining separation within the domain of the model. However, the simulations showed that the splitting of the wave packet was not well defined and that the shape of the saddle point potential due to this model was distorted. This led to a redesign of this quantum point contact, inspired by the previous models we have studied. It allowed us to make positive progress in identifying characteristics we wish to exploit in quantum point contacts. By integrating triangular geometries to the depletion and the beamsplitter gate, we were able to manipulate the trajectories of the wave packet to be more uniform and equally spaced closer to the zero point of the potential. However, we still had the same result of a less defined splitting in the wave packet. As such, it would be ideal to implement etching into this model, but a question would arise on whether such detailed fabrication can be performed at such a small scale. Our simulations restrict us greatly in the size of the domain we want to observe and so designing a quantum point contact which is part of a much larger model is challenging.

These simulations provide interesting insight into the characteristics of quantum point contacts and how they should be applied when fabricating interferometers. For example, the Mach-Zehnder interferometer requires two quantum point contacts, one to separate the paths of the electron and one to recombine them. Our simulations and analysis have shown that, for HEQO especially at high magnetic fields, the range of energy the hot-electron must be emitted at is very small to obtain a 50/50 split. This obviously provides draw backs as a higher magnetic field provides a stronger confinement and is thought to suppress LO-phonon emissions. The use of etching also creates difficulties in controlling the constriction and so the use of a depletion gate to control the path of the electron could be viable. In particular, the slow down in the velocity could prove useful for the second beamsplitter of the Mach-Zehnder interferometer, as it spread the probability distribution over a large area and create more of a chance for the split electron to recombine.

The biggest limitation to the simulations of the quantum point contacts were the domain sizes. For the first two models which created saddle point potentials using either two depletion gates or a depletion gate and etching, this was not a problem as we were able to control these sizes and where we can represent the potential in the simulation. However, for the realistic quantum point contact we are unable to change or adapt the model to fit in with our simulation size restrictions. Because of this we had to use a lower magnetic field in order to fit in as much of the region around the saddle point potential as possible. Even so, the simulations ended abruptly after the wave packet spread into both paths as it become difficult to perform a Gauge transformation for the required next frame. The simulated quantum point contact is part of a much larger model of the electronic Mach-Zehnder interferometer provided to us by Masaya Katoaka and Patrick See. This would require splitting the simulation into two simultaneous simulations each following separately the transmitted and reflected path. Initially, this would be an ideal way of following the wave packet after it has interacted with the first quantum point contact. This could continue observations of the spreading of the wave packet for a quantum point contact of this design. However, the problem of this full scale simulation lies in the exact recombination of the split wave packet at the second quantum point contact.

9.2 Outlook

While this thesis has made some important advances in the modelling and simulating of HEQO devices, it has opened the door to multiple avenues of exploration in the world of hot-electrons. The ease of producing electrostatic potentials and the interesting characteristics that can be obtained through semi-classical analysis an provide useful information in the pre-fabrication stages of an experiment. This method is also not limited to the exact structures described in this thesis. Different materials used in the heterostructure would only require a recalculation of the boundary conditions due to their characteristic properties. The process of the projected surface method can also be adjusted for other etched wires such as deep etching, where multiple projections could be done to incorporate the boundary conditions of the longer exposed etched sidewall.

The next important stage after the work in this thesis is the simulation of a full Mach-Zehnder interferometer which uses hot-electrons. This, however, would prove to be a difficult job given the challenges we have shown in simulating large devices. There is also the added complication of simulating the split path of the electron in separate frames and then making sure the simulations line up exactly with the recombination in the final beamsplitter. This would then allow us to compare with theoretical work done on seeing whether asymmetric arms maximise the visibility in hot-electron interferometers [90]. Another step would be to explore simulations which have two wave packet simulations. The numerical methods shown in this thesis have already been done for a Hong-Ou-Mandel interferometer [91] but would be interesting to continue for hot-electrons. The advantages of the projected surface method would allow for multiple variations in the modelling of such devices and the simulations would allow us to perform theoretical experiments at low cost, allowing for greater success when fabricating and performing the experiment.

A way to overcome some of the limitations in the dynamic simulations we have shown in this thesis would be an adaption of the numerical method. Instead of observing a wave packet moving through an external potential, one could attempt to change the point of view of the simulation to the wave packet itself. In this case, we would be observing a static wave packet in a moving external potential. This would overcome the challenges of performing multiple gauge transformations and time consuming tasks of moving frames. It wouldn't reduce the total number of time steps needed for large HEQO domains but it would be a great improvement to simulate such devices.

Elements of the electron quantum optic processes described in the previous sections can be used as the basis of quantum information processing. They form the architecture for the development of flying qubits. The implementation of a quantum computer must follow five requirements, known as Vincenzo's criteria [92]. Hot-electrons can offer solutions to these criteria. One way which they could be applied is by using two Landau levels to allow us to represent the hot electron in two different states of 50/50 probability. We have already observed in our simulations that the wave packet can scatter into higher Landau levels (see chapter 7) when the simulated hot electron travelled along a zig-zag path. This dramatic change in direction of the hot-electron path can be manipulated and different geometries can be tested in order to control a consistent scattering into a higher Landau level. However, hot-electrons in GaAs systems undergo the phenomena of energy relaxation through the emission of longitudinal optical mode phonons [36]. This would negatively impact the usability of hot-electrons as flying qubits, especially through encoding their quantum information in two Landau levels. Although, through studies of the mechanisms which cause this energy relaxation [48], we would be able to better understand how we can suppress them. Hopefully, the new way of modelling the complex geometries of HEQO devices and simulating the hot-electrons in these systems which we have studied in this thesis can help aid in the design of new experiments to provide a new outlook for studying these mechanisms.

Bibliography

[1] Louis de Broglie. *Quantum Theory Research.* Thesis, Migration - university being assigned, November 1924.

[2] C. J. Davisson and L. H. Germer. Reflection of Electrons by a Crystal of Nickel. *Proceedings of the National Academy of Science*, 14(4):317–322, April 1928.

[3] Claus Jönsson. Elektroneninterferenzen an mehreren künstlich hergestellten Feinspalten. *Zeitschrift fur Physik*, 161(4):454–474, August 1961.

[4] Thomas Young. I. the bakerian lecture. experiments and calculations relative to physical optics. *Philosophical Transactions of the Royal Society of London*, 94:1–16, 1804.

[5] W. D. Oliver, J. Kim, R. C. Liu, and Y. Yamamoto. Hanbury brown and twiss-type experiment with electrons. *Science*, 284(5412):299–301, 1999. doi: 10.1126/science.284.5412.299.

[6] E. Bocquillon, V. Freulon, F. D. Parmentier, J-M Berroir, B. Plaçais, C. Wahl, J. Rech, T. Jonckheere, T. Martin, C. Grenier, D. Ferraro, P. Degiovanni, and G. Fève. Electron quantum optics in ballistic chiral conductors. *Annalen der Physik*, 526(1-2): 1–30, 2014.

[7] Y. Ji, Y. Chung, D. Sprinzak, M. Heiblum, D. Mahalu, and H. Shtrikman. An electronic mach-–zehnder interferometer. *Nature*, 422:415–418, 2003.

[8] L. V. Litvin, H.-P. Tranitz, W. Wegscheider, and C. Strunk. Decoherence and single electron charging in an electronic mach-zehnder interferometer. *Phys. Rev. B*, 75: 033315, Jan 2007.

[9] Preden Roulleau, F. Portier, P. Roche, A. Cavanna, G. Faini, U. Gennser, and D. Mailly. Direct measurement of the coherence length of edge states in the integer quantum hall regime. *Phys. Rev. Lett.*, 100:126802, Mar 2008.

[10] P. Roulleau, F. Portier, P. Roche, A. Cavanna, G. Faini, U. Gennser, and D. Mailly. Noise dephasing in edge states of the integer quantum hall regime. *Phys. Rev. Lett.*, 101:186803, Oct 2008.

[11] P. Roulleau, F. Portier, P. Roche, A. Cavanna, G. Faini, U. Gennser, and D. Mailly. Tuning decoherence with a voltage probe. *Phys. Rev. Lett.*, 102:236802, Jun 2009.

[12] E. Bieri, M. Weiss, O. Göktas, M. Hauser, C. Schönenberger, and S. Oberholzer. Finite-bias visibility dependence in an electronic mach-zehnder interferometer. *Phys. Rev. B*, 79:245324, Jun 2009.

[13] D. T. McClure, Yiming Zhang, B. Rosenow, E. M. Levenson-Falk, C. M. Marcus, L. N. Pfeiffer, and K. W. West. Edge-state velocity and coherence in a quantum hall fabry-pérot interferometer. *Phys. Rev. Lett.*, 103(20):206806, 2009.

[14] Yiming Zhang, D. T. McClure, E. M. Levenson-Falk, C. M. Marcus, L. N. Pfeiffer, and K. W. West. Distinct signatures for coulomb blockade and aharonov-bohm interference in electronic fabry-perot interferometers. *Phys. Rev. B*, 79:241304, Jun 2009.

[15] G. Fève, A. Mahé, J.-M. Berroir, T. Kontos, B. Plaçais, D. C. Glattli, A. Cavanna, B. Etienne, and Y. Jin. An on-demand coherent single-electron source. *Science*, 316 (5828):1169–1172, 2007.

[16] S. Hermelin, S. Takada, M¿ Yamamoto, S. Tarucha, A. D. Wieck, L. Saminadayar, C. Bauerle, and T. Meunier. Electrons surfing on a sound wave as a platform for quantum optics with flying electrons. *Nature*, 47(435-438), 2011.

[17] R. P. G. McNeil, M. Kataoka, C. J. B. Ford, C. H. W. Barnes, D. Anderson, G. A. C. Jones, I. Farrer, and D. A. Ritchie. On-demand single-electron transfer between distant quantum dots. *Nature*, 477(439-442), 2011.

[18] S. P. Giblin, M. Kataoka, J. D. Fletcher, P. See, T. J. B. M. Janssen, J. P. Griffiths, G. A. C. Jones, I. Farrer, and D. A. Ritchie. Towards a quantum representation of the ampere using single electron pumps. *Nat. Commun.*, 3(930), 2012.

[19] Mark Oxborrow and Alastair G Sinclair. Single-photon sources. *Contemporary Physics*, 46(3):173–206, 2005.

[20] Brahim Lounis and Michel Orrit. Single-photon sources. *Reports on Progress in Physics*, 68(5):1129, apr 2005.

[21] *The Physics of Quantum Information: Quantum Cryptography, Quantum Teleportation, Quantum Computation.* Springer-Verlag, Berlin, Heidelberg, 2001. ISBN 3540667784.

[22] B. Kaestner, V. Kashcheyevs, S. Amakawa, M. D. Blumenthal, L. Li, T. J. B. M. Janssen, G. Hein, K. Pierz, T. Weimann, U. Siegner, and H. W. Schumacher. Single-parameter nonadiabatic quantized charge pumping. *Phys. Rev. B*, 77:153301, Apr 2008.

[23] K. Flensberg, A. A. Odintsov, F. Liefrink, and P. Teunissen. Towards single-electron metrology. *International Journal of Modern Physics B*, 13:2651–2687, 1999.

[24] J. Dubois, T. Jullien, F. Portier, P. Roche, A. Cavanna, Y. Jin, W. Wegscheider, P. Roulleau, and D. C. Glattli. Minimal-excitation states for electron quantum optics using levitons. *Nature*, 502(659–663), 2013.

[25] Jukka P. Pekola, Olli-Pentti Saira, Ville F. Maisi, Antti Kemppinen, Mikko Möttönen, Yuri A. Pashkin, and Dmitri V. Averin. Single-electron current sources: Toward a refined definition of the ampere. *Rev. Mod. Phys.*, 85:1421–1472, Oct 2013.

[26] R. Ionicioiu abd G. Amaratunga and F. Undrea. Quantum computation with ballistic electrons. *Int. J. Mod. Phys, B*, 15(125), 2001.

[27] S. P. Giblin, M. H. Bae, N. Kim, Y. H. Ahn, and M. Kataoka. Robust operation of a gaas tunable barrier electron pump. *Metrologia.*, 54:299–306, 2017.

[28] H. van Houten and C. W. J. Beenakker. Quantum point contacts. *Phys. Today.*, 7 (22), 1996.

[29] Neil M Zimmerman and Mark W Keller. Electrical metrology with single electrons. *Measurement Science and Technology*, 14(8):1237–1242, jul 2003.

[30] *The International System of Units (SI).* Bureau International des Poids et Mesures, 2019.

[31] C. W. J. Beenakker, C. Emary, M. Kindermann, and J. L. van Velsen. Proposal for production and detection of entangled electron-hole pairs in a degenerate electron gas. *Phys. Rev. Lett.*, 91:147901, Oct 2003.

[32] J.H. Davies and I. A. Larkin. Modeling the patterned two-dimensional electron gas: Electrostatics. *J. Appl. Phys.*, 77(9), 1995.

[33] J. D. Fletcher, P. See, H. Howe, M. Pepper, S. P. Giblin, J. P. Griffiths, G. A. C. Jones, I. Farrer, D. A. Ritchie, T. J. B. M. Janssen, and M. Kataoka. Clock-controlled

emission of single-electron wave packets in a solid-state circuit. *Phys. Rev. Lett.*, 111 (21):216807, 2013.

[34] Albert A. Michelson and Edward W. Morley. On the Relative Motion of the Earth and of the Luminiferous Ether. *Sidereal Messenger*, 6:306–310, November 1887.

[35] R. Loudon. *The Quantum Theory of Light.* OUP Oxford, 2000. ISBN 9780191589782. URL `https://books.google.co.uk/books?id=AEkfajgqldoC`.

[36] C. Emary, A. Dyson, S. Ryu, H.-S. Sim, and M. Kataoka. Phonon emission and arrival times of electrons from a single-electron source. *Phys. Rev. B*, 93:035436, Jan 2016.

[37] D. Ferraro, B. Roussel, C. Cabart, E. Thibierge, G. Fève, Ch. Grenier, and P. Degiovanni. Real-time decoherence of landau and levitov quasiparticles in quantum hall edge channels. *Phys. Rev. Lett.*, 113(16):166403, 2014.

[38] P. Degiovanni, Ch. Grenier, and G. Fève. Decoherence and relaxation of single-electron excitations in quantum hall edge channels. *Phys. Rev. B*, 80(24):241307, 2009.

[39] Mihajlo Vanević, Yuli V. Nazarov, and Wolfgang Belzig. Electron and electron–hole excitations in a driven fermi sea. *physica status solidi (b)*, 254(3):1600551, 2017.

[40] V. I. Talyanskii, J. M. Shilton, M. Pepper, C. G. Smith, C. J. B. Ford, E. H. Linfield, D. A. Ritchie, and G. A. C. Jones. Single-electron transport in a one-dimensional channel by high-frequency surface acoustic waves. *Phys. Rev. B*, 56:15180–15184, 1997.

[41] Hermann Edlbauer, Junliang Wang, Thierry Crozes, Pierre Perrier, Seddik Ouacel, Clément Geffroy, Giorgos Georgiou, Eleni Chatzikyriakou, Antonio Lacerda-Santos, Xavier Waintal, D. Glattli, Preden Roulleau, Jayshankar Nath, Masaya Kataoka, Janine Splettstoesser, Matteo Acciai, Maria da Silva Figueira, Kemal Öztas, Alex Trellakis, and C. Bäuerle. Semiconductor-based electron flying qubits: review on recent progress accelerated by numerical modelling. *EPJ Quantum Technology*, 9, 2022.

[42] M. D. Blumenthal, B. Kaestner, L. Li, S. Giblin, T.J.B.M. Janssen, M. Pepper, D. Anderson, G. Jones, and D.A. Ritchie. Electron pumping through quantum dots defined in parallel etched quantum wires. *Microelectronics Journal*, 39(3):365 – 368, 2008. ISSN 0026-2692.

[43] B. Kaestner and V. Kashcheyevs. Non-adiabatic quantized charge pumping with tunable-barrier quantum dots: a review of current progress. *Rep. Prog. Phys.*, 78 (103901), 2015.

[44] Y. H. Ahn and Y. Chung. Numerical simulation of quantized current generated by a quantum dot pump. *J. Appl. Phys.*, 122(054303), 2017.

[45] M. Kataoka, N. Johnson, C. Emary, P. See, J. P. Griffiths, G. A. C. Jones, I. Farrer, D. A. Ritchie, M. Pepper, and T. J. B. M. Janssen. Time-of-flight measurements of single-electron wave packets in quantum hall edge states. *Phys. Rev. Lett.*, 116: 126803, 2016.

[46] J. Waldie, P. See, V. Kashcheyevs, J. P. Griffiths, I. Farrer, G. A. C. Jones, D. A. Ritchie, T. J. B. M. Janssen, and M. Kataoka. Measurement and control of electron wave packets from a single-electron source. *Phys. Rev. B*, 92(12):125305, Sep 2015.

[47] J. H. Davies. Electronic states in narrow semiconducting wires near threshold. *Semicond. Sci. Technol.*, 3(995), 1988.

[48] N. Johnson, C. Emary, S. Ryu, H.-S. Sim, P. See, J. D. Fletcher, J. P. Griffiths, G. A. C. Jones, I. Farrer, D. A. Ritchie, M. Pepper, T. J. B. M. Janssen, and M. Kataoka. Lo-phonon emission rate of hot electrons from an on-demand single-electron source in a gaas/algaas heterostructure. *Phys. Rev. Lett.*, 121(137703), 2018.

[49] S. Datta. *Electronic Transport in Mesoscopic Systems.* Cambridge University Press., 1997.

[50] Lewis A Clark, Masaya Kataoka, and Clive Emary. Mitigating decoherence in hot electron interferometry. *New Journal of Physics*, 22(10):103031, oct 2020.

[51] C. Emary, L. A. Clark, M. Kataoka, and N. Johnson. Energy relaxation in hot electron quantum optics via acoustic and optical phonon emission. *Phys. Rev. B*, 99:045306, Jan 2019.

[52] T. Mimura. The early history of the high electron mobility transistor (hemt). *IEEE Transactions on Microwave Theory and Techniques*, 50(3):780–782, 2002. doi: 10.1109/22.989961.

[53] Klaus von Klitzing. The quantized hall effect. *Rev. Mod. Phys.*, 58:519–531, Jul 1986.

[54] D. C. Tsui, H. L. Stormer, and A. C. Gossard. Two-dimensional magnetotransport in the extreme quantum limit. *Phys. Rev. Lett.*, 48:1559–1562, May 1982.

[55] B Jeckelmann and B Jeanneret. The quantum hall effect as an electrical resistance standard. *Reports on Progress in Physics*, 64(12):1603, nov 2001.

[56] J. Frenkel. On the electrical resistance of contacts between solid conductors. *Phys. Rev.*, 36:1604–1618, Dec 1930.

[57] Yuli V. Nazarov and Yaroslav M. Blanter. *Quantum Transport: Introduction to Nanoscience*. Cambridge University Press, 2009. doi: 10.1017/CBO9780511626906.

[58] M. Chen, W. Porod, and D. J. Kirkner. Coupled finite element/boundary element method for semiconductor quantum devices with exposed surfaces. *Journal of Applied Physics*, 75(5):2545–2554, 1994.

[59] G. L. Snider, I.-H. Tan, and E. L. Hu. Electron states in mesa-etched one-dimensional quantum well wires. *Journal of Applied Physics*, 68(6):2849–2853, 1990.

[60] H-. Z. Guo, J. Gao, and C. Lu. Three dimensional potential distribution and quantized acoustoelectric current for a al0.3ga0.7as/gaas two-dimensional electron gas heterostructure. *Journal of Applied Physics*, 105(12):124302, 2009.

[61] MATLAB. *Partial Differential Equation Toolbox: User's Guide (R2019a).* The MathsWorks, Inc., 2019.

[62] R. D. Cook, D. S. Malkus, M. E. Plesha, and R. J. Witt. *Concepts and Applications of Finite Element Analysis.* New York, N. Y. : Wiley, 2007.

[63] G. Strang and G. Fix. *An Analysis of the Finite Elements Method.* Wellesley, MA: Wellesley-Cambridge Press, 2n edition edition, 2008.

[64] C G Smith, M Pepper, R Newbury, H Ahmed, D G Hasko, D C Peacock, J E F Frost, D A Ritchie, G A C Jones, and G Hill. One-dimensional quantised ballistic resistors in parallel configuration. *Journal of Physics: Condensed Matter*, 1(37):6763–6770, 1989.

[65] D.T. Park, S. Lee, U. Kim, H. Choi, and H. K. Choi. Robust quantum point contact via trench gate modulation. *Sci Rep*, 10(19746), 2020.

[66] A. M. Chang, H. U. Baranger, L. N. Pfeiffer, K. W. West, and T. Y. Chang. Non-gaussian distribution of coulomb blockade peak heights in quantum dots. *Phys. Rev. Lett.*, 76:1695–1698, Mar 1996.

[67] C. R. Anderson, M. F. Gyure, S. Quinn, A. Pan, R. S. Ross, and A. A. Kiselev. High-precision real-space simulation of electrostatically confined few-electron states. *AIP Advances*, 12(6):065123, 2022.

[68] J.S. Lee, Y.K.and Smith and J.H. Cole. Influence of device geometry and imperfections on the interpretation of transverse magnetic focusing experiments. *Nanoscale Res Lett*, 17(31), 2022.

[69] S. E. Laux, D. J. Frank, and F. Stern. Quasi-one-dimensional electron states in a split-gate gaas/algaas heterostructure. *Surface Science*, 196(1):101–106, 1988. ISSN 0039-6028.

[70] Andreas Marquardt. Self-consistent calculation of the electron distribution near a quantum point contact in the integer quantum hall effect. *Physical Review B*, 75: 045325, 2006.

[71] MathWorks. Partial differential equation toolbox, R2022a.

[72] Andrea Beggi, Paolo Bordone, Fabrizio Buscemi, and Andrea Bertoni. Time-dependent simulation and analytical modelling of electronic mach–zehnder interferometry with edge-states wave packets. *Journal of Physics: Condensed Matter*, 27 (47):475301, 2015.

[73] A. Beggi. *Quantum Entanglement and Electron Interference in Nanostructures: Analytical and Numerical Study of Quantum Correlations and Transport in Edge Channels and Quantum Walks.* Thesis, Universita Degli Stud Di Modena E Reggio Emilia, March 2017.

[74] J. Fletcher, N. Johnson, E. Locane, Penelope See, J. Griffiths, I. Farrer, D. Ritchie, P. Brouwer, Vyacheslavs Kashcheyevs, and Misao Kataoka. Continuous-variable tomography of solitary electrons. *Nature Communications*, 10, 11 2019.

[75] J. Fletcher, W. Park, Sungguen Ryu, Penelope See, J. Griffiths, G. Jones, I. Farrer, D. Ritchie, H-S Sim, and Misao Kataoka. Time-resolved coulomb collision of single electrons. *Nature Nanotechnology*, pages 1–6, 05 2023.

[76] S. Ryu, M. Kataoka, and H.-S. Sim. Ultrafast emission and detection of a single-electron gaussian wave packet: A theoretical study. *Phys. Rev. Lett.*, 117(146802), 2016.

[77] I. Neder, N. Ofek, Y. Chung, M. Heiblum, D. Mahalu, and V. Umansky. Interference between two indistinguishable electrons from independent sources. *Nature*, 448:333 – 337, 2007.

[78] E. Bocquillon, F. D. Parmentier, C. Grenier, J.-M. Berroir, P. Degiovanni, D. C. Glattli, B. Plaçais, A. Cavanna, Y. Jin, and G. Fève. Electron quantum optics: Partitioning electrons one by one. *Phys. Rev. Lett.*, 108:196803, May 2012.

[79] E. Bocquillon, V. Freulon, J.-M Berroir, P. Degiovanni, B. Plaçais, A. Cavanna, Y. Jin, and G. Fève. Coherence and indistinguishability of single electrons emitted by independent sources. *Science*, 339(6123):1054–1057, 2013. doi: 10.1126/science.1232572.

[80] V Freulon, A Marguerite, J-M Berroir, B Plaçais, A Cavanna, Y Jin, and Gwendal Fève. Hong-ou-mandel experiment for temporal investigation of single-electron fractionalization. *Nature communications*, 6(1):1–6, 2015.

[81] B. J. van Wees, H. van Houten, C. W. J. Beenakker, J. G. Williamson, L. P. Kouwenhoven, D. van der Marel, and C. T. Foxon. Quantized conductance of point contacts in a two-dimensional electron gas. *Phys. Rev. Lett.*, 60:848–850, Feb 1988.

[82] B. J. van Wees, L. P. Kouwenhoven, E. M. M. Willems, C. J. P. M. Harmans, J. E. Mooij, H. van Houten, C. W. J. Beenakker, J. G. Williamson, and C. T. Foxon. Quantum ballistic and adiabatic electron transport studied with quantum point contacts. *Phys. Rev. B*, 43(15):12431–12453, May 1991.

[83] N. K. Patel, J. T. Nicholls, L. Martn-Moreno, M. Pepper, J. E. F. Frost, D. A. Ritchie, and G. A. C. Jones. Evolution of half plateaus as a function of electric field in a ballistic quasi-one-dimensional constriction. *Phys. Rev. B*, 44:13549–13555, Dec 1991.

[84] N.K. Patel, L. Martín-Moreno, J.T. Nicholls, M. Pepper, J.E.F. Frost, D.A. Ritchie, and G.A.C. Jones. Quantisation of the conductance in units of e2/2h in a ballistic quasi-one-dimensional channel, produced by strong electric and magnetic fields. *Superlattices and Microstructures*, 11(2):233–235, 1992. ISSN 0749-6036.

[85] T. J. Thornton, M. Pepper, H. Ahmed, D. Andrews, and G. J. Davies. One-dimensional conduction in the 2d electron gas of a gaas-a1gaas heterojunction. *Phys.Rev. Lett.*, 56(1198), 1986.

[86] B. I. Halperin. Quantized hall conductance, current-carrying edge states, and the existence of extended states in a two-dimensional disordered potential. *Phys. Rev. B*, 25(4):2185–2190, Feb 1982.

[87] Martina Flöser, Serge Florens, and Thierry Champel. Transmission coefficient through a saddle-point electrostatic potential for graphene in the quantum hall regime. *Physical Review B*, 82(16):161408, 2010.

[88] P. Wesseling and C.W. Oosterlee. Geometric multigrid with applications to computational fluid dynamics. *Journal of Computational and Applied Mathematics*, 128(1):

311–334, 2001. ISSN 0377-0427. Numerical Analysis 2000. Vol. VII: Partial Differential Equations.

[89] Nathan Johnson. personal communication.

[90] Clarissa J. Barratt, Sungguen Ryu, Lewis A. Clark, H.-S. Sim, Masaya Kataoka, and Clive Emary. Asymmetric arms maximize visibility in hot-electron interferometers. *Phys. Rev. B*, 104:035436, Jul 2021.

[91] L. Bellentani, P. Bordone, X. Oriols, and A. Bertoni. Coulomb and exchange interaction effects on the exact two-electron dynamics in the hong-ou-mandel interferometer based on hall edge states. *Phys. Rev. B*, 99:245415, Jun 2019.

[92] David P. DiVincenzo. The physical implementation of quantum computation. *Fortschritte der Physik*, 48, 2000.